Z-boson and double charm production with ALICE at the LHC

Sizar Aziz

université
PARIS-SACLAY

Production des bosons Z et du double charme avec ALICE auprès du LHC

Z-boson and double charm production with ALICE at the LHC

Thèse de doctorat de l'Université Paris-Saclay

École doctorale n° 576, Particules, Hadrons, Énergie et Noyau : Instrumentation, Image, Cosmos et Simulation (PHENIICS)

Spécialité de doctorat: Physique hadronique

Unité de recherche: Université Paris-Saclay, CNRS, IJCLab, 91405, Orsay, France

Référent: Faculté des sciences d'Orsay

Thèse présentée et soutenue à Orsay, le 30 septembre 2021 par

Sizar AZIZ

Composition du jury

Marie-Hélène SCHUNE	Présidente
Directrice de recherche, CNRS, Université Paris-Saclay (IJCLab)	
Philippe ROSNET	Rapporteur & Examinateur
Professeur, Université Blaise Pascal (LPC)	
Marco VAN LEEUWEN	Rapporteur & Examinateur
Directeur de recherche, Nikhef (Pays-Bas)	
Ingo SCHIENBEIN	Examinateur
Maître de conférences, Université Joseph Fourier (LPSC)	
Diego STOCCO	Examinateur
Chargé de recherche, Université de Nantes (Subatech)	

Direction de la thèse

Bruno ESPAGNON	Directeur de thèse
Professeur, Université Paris-Saclay (IJCLab)	
Zaida CONESA DEL VALLE	Co-encadrante
Chargée de recherche, CNRS, Université Paris-Saclay (IJCLab)	
Christophe SUIRE	Co-encadrant
Chargé de recherche, CNRS, Université Paris-Saclay (IJCLab)	

Thèse de doctorat

NNT: 2021UPASP092

Acknowledgements

First of all, I would like to express a special thanks to my thesis director Bruno Espagnon. I highly value the discussions we had on physics and your willingness to answer any questions I asked. For the day-to-day supervision, I would like to express a special thanks to my supervisor Zaida. Your exemplify for me a keen mind and attention to detail. And there is of course your golden rule that I mostly adhered to: never ask more than 1 question in an email, if you want to have them answered! Another person to whom I feel deep gratitude is Christophe, who was particularly present during the second half of my thesis. I enjoyed working under your supervision on the DualSampa's. Moreover, I obtained some silent insights from watching you lead the team, that might come in handy one day.

I cannot forget of course the other members of the team at Orsay. Special thanks is given first and foremost to Cynthia and Chun-Lu for being one of my valued cookie testers (together with Ho-San Ko and Mylène). Chun-Lu, we spent a lot of time together discovering Paris and trying to understand the french way of thinking. Laure, you were always willing to answer any technical questions I had, for which I'm grateful. Jana, whom I only got to know for a brief period, but you were able to impart some wisdom into me regardless. Your books about dealing with the french were very much appreciated! Thera, Afnan and Charlotte, we spent limited time together due to circumstances beyond our control but I have good memories of our interactions.

Furthermore, I would like to take a moment to thank Ingo Schienbein, Marie Hélène-Schune, Diego Stocco and Bruno Espagnon for agreeing to be in the Jury and Marco van Leeuwen and Philippe Rosnet for accepting the role of rapporteur on top of that.

Going back in time a bit, I would also like to thank the team at the University of Utrecht and Nikhef, where I did my master thesis with the ALICE group. It was here that I got my first real taste of the life of a scientist, and through my development here I was able to continue on with the team in Orsay. So I would like to express a warm thanks to Panos and Rihan for their supervision, and Davide for helping me apply for the PhD position that I ended up filling.

Physics aside, a PhD is also a great time to make new friends with other students. Melih, I enjoyed the regular visits to musea and restaurants together with Chun-Lu. Then there are the students from across the hallway: Pierre, Sheng-Ying, Ho-San Ko and Mylène. We always had a great time, whether visiting bars or the mountains in Lyon. A special mention goes out to Guillaume, Nicolò and Ophélie, who were my partners in crime for the paper writing process. I'm happy we were able to share the occasional late-night stress together.

Lastly but certainly not leastly, I would like to appreciate my family and friends back home. In particular, my parents, my brothers, and my aunt and uncle. On top of that, my friends who found the time to visit Paris, spending some days together always felt like mini vacations.

Synthèse en français

Chapitre 1: Introduction

Le modèle standard (SM) classifie toutes les particules et leurs interactions. Dans le SM, la chromodynamique quantique (QCD) décrit l'interaction forte et possède deux propriétés importantes. La première est celle de confinement, qui impose que les charges de couleur ne peuvent pas être observés isolées. Il est seulement possible de mesurer des particules composites, qui sont incolores. La deuxième propriété de QCD est la liberté asymptotique, qui impose qu'à courtes distances (ou à hautes énergies), l'interaction forte s'affaiblit. Dans des conditions extrêmes de très haute densité de particules et/ou de très haute température, la liberté asymptotique amène à un nouvel état de la matière, appelé le Plasma de Quarks et Gluons (QGP). En réalisant des collisions d'ions lourds, il est possible d'atteindre ces conditions extrêmes, et d'étudier le QGP. Cela est important afin de comprendre l'univers quelques microsecondes après le Big Bang, qui était supposément composé d'un QGP.

La QCD permet de calculer des sections efficaces des processus partoniques. Par contre, à cause du confinement, les partons libres n'existent pas dans la nature. Des modèles ont été conçus afin de décrire la production des particules dans des collisions proton-proton. L'un de ces modèles est la factorisation colinéaire inclusive. En convoluant les sections efficaces partoniques avec les probabilités de trouver des partons, des sections efficaces hadroniques peuvent être calculées. Cela est fait en particulier pour les particules lourdes ou très énergétiques (appelées les sondes dures) pour lesquelles il est possible de calculer les sections efficaces partoniques avec la QCD perturbative. La probabilité de trouver un parton donné est encodé dans les fonctions de distributions des partons (PDFs). Ce sont des objets non-perturbatifs, ce qui veut dire qu'ils ne peuvent pas être dérivés de QCD. Ils sont obtenus par des ajustements basés sur des mesures expérimentales. Des mesures ont montré que ces distributions de partons sont différentes entre les protons et les ions lourds. Les distributions des partons dans les ions lourds ne sont pas de simples superpositions de celles des protons et des neutrons. En conséquent, pour comprendre la production des particules lourdes dans des collisions d'ions lourds, il est très important de connaître les distributions de partons nucléaires (nPDFs). Il est en effet crucial de bien séparer ces effets, venant de la matière froide, de ceux de la matière chaude (c'est à dire le QGP). Comme les PDFs, les nPDFs sont obtenus par des ajustements basés sur des mesures expérimentales. Les bosons électrofaibles sont des outils particulièrement utiles pour étudier et contraindre les nPDFs. Ne possédant pas de charge de couleur, ils n'interagissent pas avec

le QGP qui se forme dans les collisions d'ions lourds.

Récemment, des corrélations angulaires et des augmentations du taux de production d'étrangeté ont été observées dans des collisions pp et p–A à haute multiplicité. Les observations étaient surprenantes car ces phénomènes sont typiquement associés au QGP. Beaucoup d'efforts théoriques prennent place pour mieux comprendre ce comportement. Une origine suggérée est celle des interaction multiples de partons (MPI). Cette modélisation est basée sur le fait qu'à hautes énergies, les densités de parton s'accroissent fortement. Cela augmente la probabilité que plusieurs partons se heurtent pendant une seule collision pp (ou p–A). Ces MPI peuvent, entre outre, se manifester dans la production de plusieurs particules lourdes comme le J/ψ. La production des paires de J/ψ est sensible aux contributions d'un seule diffusion (SPS) ou de double diffusion (DPS) de partons.

Chapitre 2: Le détecteur ALICE

ALICE est un détecteur dédié aux ions lourds. Il a pour dimensions $16 \times 16 \times 16\ \mathrm{m}^3$ et pèse 10000 tonnes. Le détecteur est capable de mesurer une grande variété de particules, comme les hadrons, les électrons, les muons et les photons. Le système de déclenchement d'acquisition des événements utilise principalement le détecteur V0. Le V0 se compose d'une paire de détecteurs de scintillement qui sont placés de chaque côté du point d'interaction (IP). Le Silicon Pixel Detector, qui entoure l'IP, est utilisé pour obtenir le vertex primaire d'une collision. Les analyses décrites dans cette thèse utilisent des données récoltées par le spectromètre à muons d'ALICE.

Le spectromètre à muons couvre la pseudo-rapidité $2.5 < |\eta| < 4$ et consiste en

- 5 stations de trajectographie, chacune équipée de deux chambres de trajectographie
- des absorbeurs qui réduisent le bruit de fond venant des décroissances des pions et kaons
- un aimant dipolaire pour courber les trajectoires des muons afin de permettre la mesure de leur impulsion
- 2 stations de déclenchement, chacune équipée de deux chambres de déclenchement. Cela permet de sélectionner des événements qui contiennent une paire de muons de charges opposées

Chapitre 3: Boson Z: méthode d'analyse

Les objectifs de l'analyse de la production du boson Z sont de quantifier la production invariante dans des collisions Pb–Pb et de la comparer avec la production dans des collisions pp. La production invariante en collisions Pb–Pb sera normalisée par la fonction de recouvrement nucléaire afin de la réduire à l'équivalent d'une collision nucléon-nucléon.

L'analyse est conduite sur les données de collisions Pb–Pb à une énergie dans le centre de masse par paire de nucléons de $\sqrt{s_{\mathrm{NN}}} = 5.02\,\mathrm{TeV}$. Les données ont été récoltées par le spectromètre à muons en 2015 et 2018. Le déclenchement des événements est appelé CMUL7. Les événements CMUL7 sont définis par le déclenchement de bias minimum, définie par la coïncidence d'un signal dans les détecteurs V0A et V0C, auquel se rajoute le déclenchement lié au signal d'une paire de muons de charges opposées. Certains critères sont requis pour les

traces de muons analysées. Parmi d'autres, la pseudo-rapidité des traces doit satisfaire la condition $-4 < \eta_\mu < -2.5$ et l'impulsion transverse doit être suffisamment grande, $p_{\mathrm{T}\mu} > 20$ GeV/c.

Pour extraire le signal des bosons Z, toutes les paires possibles de muons (dimuons) de charges opposées sont associées événement par événement pour construire le spectre de masse invariante. Une sélection sur la rapidité des dimuons est faite ($2.5 < y_{\mu\mu} < 4.0$). Le nombre de bosons Z est déterminé avec le spectre de masse invariante en comptant le nombre de dimuons qui ont une masse $60 < m_{\mu\mu} < 120$ GeV/c^2. Dans l'ensemble des données, 208 candidats bosons Z ont été trouvés. Le nombre de candidats Z produits est ensuite corrigé par l'acceptance cinématique et l'efficacité du détecteur. Le facteur de correction acceptance$\times$efficacité est déterminé avec des simulations PYTHIA 6 et POWHEG. Finalement, le taux de production est normalisé par le nombre équivalent d'événements de biais minimum utilisé dans l'analyses afin d'obtenir la production invariante. Le calcul du nombre d'événements de biais minimum passe par le calcul d'un facteur reliant ces derniers au CMUL7, plus sélectif, défini précédemment.

Chapitre 4: Boson Z: résultats

Dans cette section, la production invariante du boson Z est détaillée. Elle est présentée en fonction de la centralité et de la rapidité et intégrée sur ces variables. Les résultats sont comparés à plusieurs prédictions théoriques. Certains modèles théoriques comprennent des modifications nucléaires aux distributions de partons, c'est-à-dire des nPDFs. Ces modèles s'appellent EPS09s, EPPS16, et NCTEQ. Un seul modèle, CT14NLO, ne comprend pas de telles modifications et considère les noyaux comme des superpositions simples des protons et neutrons.

La production invariante dans la classe de centralité de 0-90% et dans l'intervalle de rapidité $2.5 < y_{\mu\mu} < 4.0$ est en accord avec les trois modèles de nPDF. Par contre, une différence de $3.4\ \sigma$ est trouvée entre la valeur mesurée et celle prédite par CT14NLO. Cette différence est plus grande que la différence de $2.3\ \sigma$ obtenue dans une mesure précédente d'ALICE (qui utilisait une statistique moindre, i.e. un sous-ensemble des données utilisées dans cette thèse). Les trois modèles de nPDF prédisent une valeur plus basse que celle du CT14NLO. Cette diminution est attribuée à deux effets nucléaires: l'ombrage, ou shadowing, à bas Bjorken-x (fraction d'impulsion emportée par un parton) et l'effet EMC à Bjorken-x intermédiaire, qui tous deux causent une déplétion des fonctions de distribution des partons nucléaires comparées à celles de protons et de neutrons. Dans un schéma de production de type $2 \to 1$, un Z produit dans l'acceptance du spectromètre à muons provient principalement de partons possédant des Bjorken-x dans les régions du *shadowing* et de l'EMC.

En fonction de la rapidité, la production invariante de Z est en accord avec EPPS16, mais en désaccord avec CT14NLO. Le désaccord avec CT14NLO augmente pour les plus grandes valeurs de rapidité. Cela s'explique par le fait qu'à grande rapidité les valeurs de Bjorken-x sondées diminuent et l'effet d'ombrage est donc plus prononcé.

La production invariante de Z en fonction de la centralité est compatible avec une valeur constante. Cela est attendu pour les sondes dures incolores insensible aux effets de QGP. C'est un test important pour le modèle de Glauber à partir duquel de nombreuses quantités géométriques utilisées dans les collisions d'ions lourds sont

calculées.

Chapitre 5: Boson Z: projections pour LHC Run 3

Les nPDFs sont obtenues par des ajustements basés sur des mesures expérimentales. La plupart des données à hautes énergies proviennent du LHC et concernent donc des ions de plomb. Par conséquent, la dépendance en masse atomique A n'est pas bien connue. Des mesures faites sur des collisions d'ions plus légers seront utiles pour contraindre cette dépendance. Dans le LHC Run 3, des collisions d'oxygène sont prévues. Plus spécifiquement, ce sont des collisions p–O à une énergie dans le centre de masse par paire de nucléons de $\sqrt{s_{\rm NN}} = 9\,\rm TeV$ et O–O à $\sqrt{s_{\rm NN}} = 6.37\,\rm TeV$. Les luminosités intégrées attendues dans les deux systèmes de collisions sont $5\ \rm nb^{-1}$ et $1\ \rm nb^{-1}$, respectivement. Dans cette thèse, des projections de la production du boson Z ont été faites pour déterminer si une mesure serait faisable.

Les projections sont obtenues par extrapolation des mesures actuelles de la section efficace du boson Z publiées par les collaborations ALICE et LHCb. Cependant, les mesures de section efficace existantes sont faites à une énergie différente de celles des collisions oxygène. De plus, la distributions en rapidité des bosons Z produits change aussi en fonction de l'énergie et du système de collision. Par conséquent, des corrections ont dû être appliquées sur les mesures actuelles. Ces corrections sont obtenues par des simulations PYTHIA 6. Pour valider la stratégie, des sections efficaces déjà mesurées ont été recalculées et un bon accord a été trouvé entre les deux valeurs.

Finalement, il apparaît qu'avec les luminosités prévues, la production de Z dans le spectromètre à muons d'ALICE serait de 3 bosons Z dans les collisions p–O à $\sqrt{s_{\rm NN}} = 9\,\rm TeV$ et elle serait de 4 bosons Z dans les collisions O–O à $\sqrt{s_{\rm NN}} = 6.37\,\rm TeV$. La mesure n'est donc possible dans aucun des systèmes de collision. Si le temps de prise des données alloué était augmenté, des mesures pourraient être possible.

Chapitre 6: Production de paires de J/ψ: méthode d'analyse et résultats

Ce chapitre présente la mesure de la section efficace des paires de J/ψ. Les J/ψ sont mesurés via leur décroissance en une paire de muons de charge opposée et dans l'intervalle de rapidité $2.5 < y_{\mu\mu} < 4$. L'analyse a été faite sur l'ensemble des données du Run 2, qui comprend des collisions de protons à une énergie dans le centre de masse de $\sqrt{s} = 13\,\rm TeV$, récoltées par le spectromètre à muons entre 2016 et 2018.

En combinant toutes les paires possibles de double dimuons ou di-dimuons par événement, un spectre de masse invariante à deux dimensions de masse a été construit. Le nombre de paires de J/ψ est extrait de ce spectre par un ajustement à deux dimensions. Pour ce faire, les paramètres des fonctions ont préalablement été déterminés par des ajustements aux distributions de masse invariante à une dimension. Un total de 12 configurations différentes a été utilisé en prenant différentes combinaisons des fonctions d'ajustement pour le signal, le bruit de fond et l'intervalle d'ajustement. Sur la base des résultats des ajustements 1-D, les paramètres de la fonction du signal ont été fixés, et une nouvelle fonction en 2D a été construite. Cette dernière étape consiste à prendre le carré des fonctions en 1D, en introduisant une nouvelle variable de masse. L'acceptance et l'efficacité du détecteur pour les

paires de J/ψ est factorisée comme le produit de l'acceptance et de l'efficacité déterminée pour un J/ψ en faisant donc l'hypothèse que la paire est non-corrélée. La luminosité est calculée à partir d'un nombre d'événements analysés de type CMUL7 renormalisé au nombre d'événements de biais minimum. Pour l'ensemble des données analysées, une valeur de $\mathcal{L} = 24.38 \pm 0.01\ (\mathrm{stat}) \pm 0.87\ (\mathrm{syst}) \mathrm{pb}^{-1}$ a été trouvée pour la luminosité intégrée.

La mesure concerne les paires de J/ψ inclusive. Cela veut dire qu'aucune distinction n'a été faite entre les contributions promptes et non-promptes. La contribution non-prompte a pour origine des paires de $b\bar{b}$ qui s'hadronisent en deux hadrons beaux, qui ensuite décroissent chacun en un J/ψ. Des simulations avec PYTHIA 6 ont permis d'estimer cette contribution.

La section efficace inclusive des paires de J/ψ a été évaluée à $10.2 \pm 2.3\ (\mathrm{stat}) \pm 1.1\ (\mathrm{syst})\ \mathrm{nb}$. Après soustraction des contributions non-promptes, la section efficace différentielle est $\frac{\mathrm{d}\sigma}{\mathrm{d}y} = 5.5 \pm 1.5\ (\mathrm{stat}) \pm 0.8\ (\mathrm{syst})\ \mathrm{nb}$. Cela est en bon accord avec la valeur $\frac{\mathrm{d}\sigma}{\mathrm{d}y} = 6.1 \pm 0.4\ (\mathrm{stat}) \pm 0.4\ (\mathrm{syst})$ publiée par LHCb. Lors des prochaines prises de données du LHC (runs 3 et 4), la luminosité intégrée devrait augmenter d'un facteur 8. Grâce à cette statistique plus importante, la précision expérimentale s'améliorera fortement. De plus, l'installation du nouveau détecteur à l'avant, Muon Forward Tracker, nous donnera la capacité de déterminer très précisément les vertex primaires et secondaires dans les collisions. Cela permettra de rejeter les contributions non-promptes directement en sélectionnant les vertex déplacés.

Chapitre 7: Conclusions

La physique de QGP est un domaine propice pour étudier la QCD sous des conditions extrêmes. Pour comprendre le QGP, il est très important de pouvoir séparer des effets de matière chaude (le QGP) de ceux induits par la matière nucléaire froide. En particulier, les distributions de partons dans les noyaux sont différentes de celles des protons et neutrons. Les distributions de partons nucléaires forment la base des calculs des sections efficaces des particules lourdes et/ou très énergétiques. Ce sont des objets non-perturbatifs, et ils sont obtenus par ajustements basés sur des mesures expérimentales. Les données utilisées dans ces ajustements proviennent d'une multitude de sources. Parmi ces sources, nous trouvons les mesures des bosons électrofaibles. Comme ils n'ont pas de charge de couleur, ils n'interagissent pas avec la matière chaude et dense formée dans des collisions d'ions lourds. En conséquent, la production des bosons électrofaibles peut être utilisée pour contraindre les nPDFs. Dans cette thèse, la production du boson Z dans des collisions Pb–Pb à $\sqrt{s_{\mathrm{NN}}} = 5.02\,\mathrm{TeV}$ est rapportée. Les bosons Z sont reconstruits via leur décroissance en une paire de muons de charges opposées, avec une impulsion transverse des muons de $p_{\mathrm{T}\,\mu} > 20$ GeV/c, une pseudo-rapidité des muons de $-4 < \eta_\mu < -2.5$, une masse invariante des dimuons de $60 < m_{\mu\mu} < 120$ GeV/c^2 et une rapidité des dimuons de $2.5 < y_{\mu\mu} < 4.0$. La production a été mesurée en fonction de la centralité et de la rapidité. Les résultats ont été comparés à des modèles théoriques incluant ou pas les nPDFs. Les résultats montrent une forte préférence pour les modèles qui incluent des nPDFs. Une déviation de 3.4 σ est observée entre nos résultats et les prédictions du modèle qui ne tient pas compte pas des effets nucléaires dans les distributions de partons. En fonction de la rapidité, la préférence pour les modèles nucléaires

augmente pour les grandes valeurs de rapidité. Cela est attribué à l'effet d'ombrage qui est principalement sondé à bas Bjorken-x, correspondant à des grandes valeurs de rapidité. Dans les runs 3 et 4 du LHC, les prises de données en collisions Pb–Pb continueront avec un taux d'acquisition considérablement plus grand dans ALICE. La luminosité intégrée devrait croître d'un facteur 10. Cette meilleure statistique permettra d'améliorer la précision de nos mesures expérimentales, ce qui fournira des contraintes plus fortes dans les ajustements des nPDFs.

En plus de la prise de données de Pb–Pb, de collisions avec des noyaux d'oxygène sont aussi prévues au LHC. Dans cette thèse, des projections ont été faites pour la faisabilité des mesures de boson Z dans des collisions p–O à $\sqrt{s_{\mathrm{NN}}} = 9\,\mathrm{TeV}$ et O–O à $\sqrt{s_{\mathrm{NN}}} = 6.37\,\mathrm{TeV}$. Les projections ont été obtenues par des extrapolations des mesures existantes des collaborations ALICE et LHCb. Avec les luminosités intégrées prévues les mesures ne seront pas possibles.

Des phénomènes typiquement associés au QGP ont récemment été observés dans des collisions pp et p–A à haute multiplicité. Jusqu'à présent, l'origine de ces phénomènes n'est pas bien comprise. Certaines théories suggèrent que des gouttelettes de QGP pourraient se former. Une autre explication est celle des interactions multiples de partons (MPI). Le cadre des MPI est basé sur le fait qu'à haute énergie, les densités des partons augmentent rapidement. Avec les hautes densités, il devient possible que plusieurs interactions de partons se produisent pendant une seule collision pp (ou p–A). Les MPI peuvent être indirectement observées dans la production de paires de J/ψ, qui reçoit des contributions des interactions simples (SPS) ainsi que des interactions doubles (DPS), cas le plus simple des MPI.

Dans cette thèse, la production inclusive des paires de J/ψ dans des collisions proton-proton à $\sqrt{s} = 13\,\mathrm{TeV}$ a été déterminée. Les J/ψ ont été mesurés via leur décroissance en paire de muons de charges opposées dans l'intervalle en rapidité $2.5 < y_{\mu\mu} < 4.0$. L'analyse porte sur une luminosité intégrée de $\mathcal{L} = 24.38 \pm 0.01\ (\mathrm{stat}) \pm 0.87\ (\mathrm{syst})\mathrm{pb}^{-1}$. La contribution des décroissances des hadrons B, autrement dit les contributions non-promptes, a été estimée. Après la soustraction de ces contributions non-promptes, la section efficace différentielle $\frac{\mathrm{d}\sigma}{\mathrm{d}y}$ vaut $5.5 \pm 1.5\ (\mathrm{stat}) \pm 0.8\ (\mathrm{syst})\ \mathrm{nb}$. Cela est en accord avec la valeur de $\frac{\mathrm{d}\sigma}{\mathrm{d}y} = 6.1 \pm 0.4\ (\mathrm{stat}) \pm 0.4\ (\mathrm{syst})$ publiée par la collaboration LHCb. Il faudra attendre les prochains runs du LHC et l'augmentation luminosité intégrée pour affiner nos résultats. D'une part, nous pourrons réduire les incertitudes et exclure directement la composantes non-prompte. D'autre part, nous voudrions mesurer la section efficace en fonction de la différence en rapidité des deux J/ψ Δy. Cette mesure permet notamment de séparer les contributions SPS et DPS, cette dernière étant supposée dominer la section efficace à grand Δy.

Contents

Chapter 1

Introduction

1.1 Quantum Chromodynamics and the Quark-Gluon plasma

1.1.1 The Standard Model and Quantum Chromodynamics

The main goal of modern particle physics is to classify all elementary particles and to describe the interactions between them. This information is encapsulated in the Standard Model (SM) of particle physics, which was developed in the latter half of the 20th century. The Standard Model classifies two kinds of elementary particles: fermions with half-integer spin, and bosons with integer spin. Fermions are considered the building blocks of all matter, while interactions between them are mediated by the elementary bosons. The fermions can be subdivided into quarks that participate in strong interactions and leptons that only participate in electroweak interactions. Both quarks and leptons can be arranged into a family structure, where each subsequent generation has the same quantum numbers as the previous, with the exception of mass. Lastly, for each particle, there is a corresponding antiparticle, with opposite charge and magnetic moment. An overview of the SM is shown in Fig. 1.1. With the discovery of the Higgs boson in 2012, all particles of the Standard Model have been experimentally observed.

The SM not only classifies which particles exist, but also how the various particles can interact with each other. Three of the four fundamental forces are described within the Standard Model: the strong force, the electromagnetic force and the weak force. They are mediated by respectively gluons, photons, and the W and Z bosons. It has been shown that the electromagnetic force and weak force can be unified into a single electroweak (EW) theory. This insight has led to the question of whether the EW force and strong force can also be unified into a singular force, in a Grand Unified Theory. Another open question of the Standard Model is how the last fundamental force, gravity, can be included.

The strong force is described by a part of the SM called Quantum Chromodynamics (QCD). In QCD, interactions occur through exchanges of color charge, mediated by gluons. A unique feature of QCD is that gluons themselves

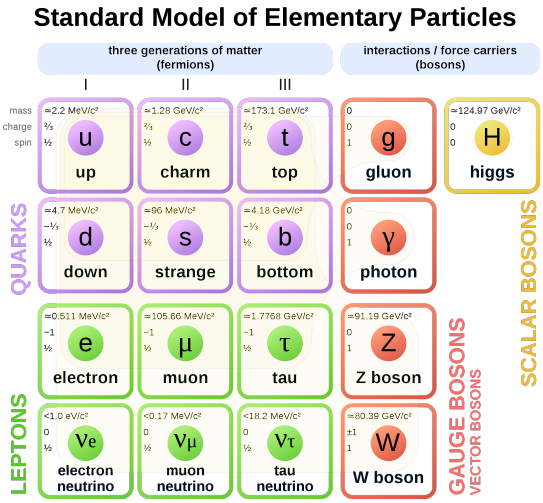

Figure 1.1: The Standard Model of particle physics. The family structure of quarks and leptons (together known as fermions) is shown, as well as the fundamental bosons that describe their interactions. Figure taken from [1].

carry color charge. In contrast, in electromagnetic interactions described by Quantum Electrodynamics (QED), photons are the mediators of interactions while they themselves carry no electric charge. Highly non-trivial dynamics arise from the fact that gluons carry color charge, and can therefore interact with other gluons. When gauge theories such as QCD are renormalized (a procedure necessary to obtain meaningful results at higher orders in perturbation theory), the coupling constant is no longer constant. Instead, it is said to run, and becomes dependent on the energy scale of interactions. The presence of the aforementioned self-interactions drastically influences the behavior of the running of the coupling α_s, shown in Figure 1.2.

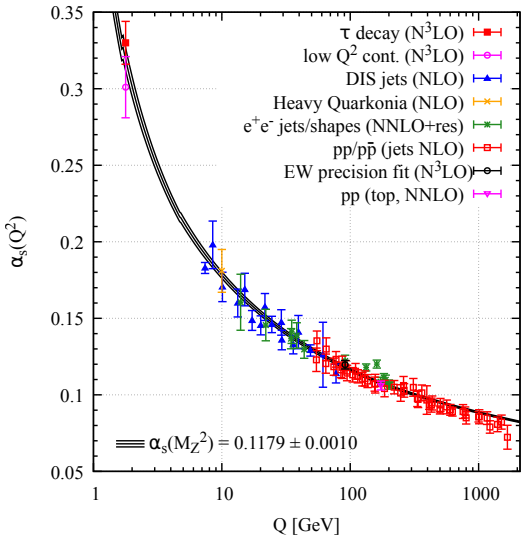

Figure 1.2: Running of the coupling α_s as a function of the energy scale Q. At large Q, the coupling becomes weak. Oppositely, at low Q, α_s becomes so large that perturbative QCD is no longer applicable. Figure taken from [2].

The running of the QCD coupling has two main features. First, as the energy scale Q grows (or equivalently

at smaller distances), α_s becomes weaker. This feature of QCD is called asymptotic freedom. For energy scales $0.1 - 1$ TeV, $\alpha_s \sim 0.1$, which means that perturbative QCD (pQCD) can be applied to compute physical quantities such as production cross sections. On the other hand, at low energy scale (equivalently, at large distances), the coupling diverges. Lattice QCD calculations show that due to the large value of α_s at large distances, the potential energy between two color charges increases linearly. When separating two color charges (i.e. quarks or gluons), it becomes energetically more favorable at some point to create a new quark-antiquark pair, so that in the end free color charges are never observed in Nature. Instead, only colorless bound states consisting of two or more quarks have been observed. This phenomenon is called (color) confinement. Confinement is related to the divergence of α_s at low energy scales, but because confinement is a non-perturbative process, no proof from first principles exists[1]. The composite particles that can be observed are called hadrons. A subdivision is made between bound states of even numbers of quarks called mesons and of odd numbers of quarks called baryons.

1.1.2 The Quark-Gluon Plasma and heavy-ion collisions

Shortly after the introduction of asymptotic freedom in QCD, two separate groups realised its consequences. Because the strong coupling weakens at smaller distances, at sufficiently high density and temperature, hadrons should dissolve into a deconfined state of quarks and gluons. This state of matter was named the Quark-Gluon Plasma (QGP). The QGP is closely related to cosmology, as it is expected to be the state of the universe very shortly after the Big Bang. This means that beside the interest of studying matter under extreme conditions, understanding the QGP can give insights into the earliest stages of the Universe. In order to recreate and study the QGP, large temperatures and densities are needed. Both conditions can be achieved by colliding ultrarelativistic heavy ions.

1.1.2.1 Heavy-ion variables

Before discussing the physics of heavy-ion collisions, it is useful to introduce quantities that are commonly used in heavy-ion physics.

(pseudo)rapidity

In high-energy collider experiments, beams are directed along a beam axis which is typically defined as the z-axis. Collisions then occur between one beam with its momentum along the $+z$ direction, and another beam with its momentum along the $-z$ direction. Colliding partons will generally not have equal momenta however, so that the center-of-mass frame of the collision will be boosted along the z-axis. The rapidity of a particle is defined as

$$y = \frac{1}{2} \ln \left(\frac{E + p_z}{E - p_z} \right), \tag{1.1}$$

[1] As a matter of fact, a one million dollar reward is promised by the Clay Mathematics Institute for a formal proof of confinement.

where E is the energy of the particle and p_z its momentum along the z-axis. The rapidity can be considered as a relativistic measure of velocity. It is defined such that a rapidity of 0 means that the particle is traveling transverse to the z-axis, and tends to $\infty(-\infty)$ when it travels along the positive (negative) z axis. Rapidity is not a lorentz invariant quantity, although it has very useful properties. Namely, it changes by a constant under a longitudinal (i.e. along the z-axis) Lorentz boost. This means that rapidity differences are a lorentz invariant quantity.

Because a measurement of both the energy and the total momentum is necessary for the determination of rapidity, it can be difficult to measure for highly relativistic particles. This is especially the case at large rapidity for particles that travel close to the beam axis, and therefore to the beam pipe (where no detection elements are present). A related quantity that is experimentally much more accessible was therefore defined. This quantity is called the pseudorapidity and is defined as

$$\eta = -\ln\left[\tan\left(\frac{\theta}{2}\right)\right], \tag{1.2}$$

where θ is the angle between the particle and the z-axis. It can be shown that for ultrarelativistic particles (i.e. with mass negligible compared to momentum), $y \approx -\ln\left[\tan\left(\frac{\theta}{2}\right)\right]$, so that $y \approx \eta$. Only the angle relative to the beam axis has to be measured for the pseudorapidity, which is much simpler than measuring both the energy and momentum.

Centrality, $\langle N_{\mathrm{part}}\rangle$ and $\langle N_{\mathrm{coll}}\rangle$

Collisions between heavy ions can occur with different geometries, depending on the impact parameter b, which is defined as the transverse distance between the center of the two nuclei. Based on the impact parameter, centrality percentiles can be assigned as a percentage of the total nuclear interaction cross section.

Related to the notion of centrality, a distinction is made between two types of nucleons: spectator nucleons which do not encounter other nucleons and participant nucleons (also called wounded nucleons) which undergo at least one scattering. The relation with the total number of nucleons is straightforward: $\langle N_{\mathrm{spec}}\rangle + \langle N_{\mathrm{part}}\rangle = N_A + N_B$, where N_A and N_B represent the total number of nucleons in nuclei A and B. Because it is possible for a nucleon to collide more than once, it proves useful to also define the number of binary collisions $\langle N_{\mathrm{coll}}\rangle$ in an event. It has been experimentally established that soft production scales with $\langle N_{\mathrm{part}}\rangle$, while hard probes scale with $\langle N_{\mathrm{coll}}\rangle$ [3].

The quantities $\langle N_{\mathrm{part}}\rangle$, $\langle N_{\mathrm{coll}}\rangle$, and $\langle N_{\mathrm{spec}}\rangle$ are closely related to the centrality percentile (impact parameter) of an event, although they cannot be directly measured in experiments. However, given certain event properties they can be estimated. The estimation of centrality, $\langle N_{\mathrm{part}}\rangle$ and $\langle N_{\mathrm{coll}}\rangle$ is based on Glauber Monte Carlo (MC) models [4]. The Glauber MC translates the centrality of an event to a mean charged particle multiplicity. In data, the latter can be measured and therefore converted back to a centrality (or impact parameter) using the Glauber MC. This conversion is shown in Figure 1.3.

A fundamental assumption of the Glauber MC is that the charged particle multiplicity depends monotonically on the impact parameter b. At low b, the nuclei collide head-on, and the resulting charged particle multiplicity is large.

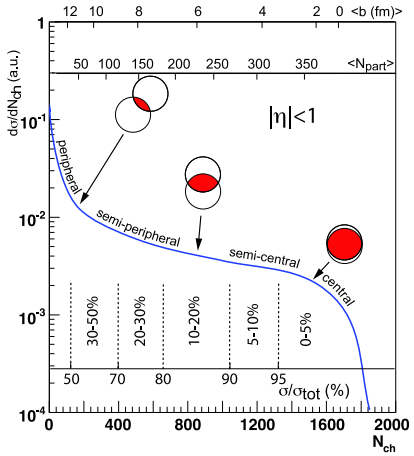

Figure 1.3: An example of the Glauber MC modeling of the number of charged particles based on centrality class (impact parameter) and $\langle N_{\mathrm{part}} \rangle$. The plotted distribution is illustrative and does not pertain to any specific measurement. Figure taken from [4].

The corresponding centrality class has a low value, for example $0-5\%$. This kind of head-on event is called a central event. Inversely, in the $80-90\%$ centrality class, corresponding to large values of b, multiplicities are (relatively) low. These events are called peripheral events.

As a closing remark, any impact parameter dependence or centrality dependence in this thesis relates strictly to quantities measured in collisions between heavy nuclei. In specialized analyses on proton–proton collisions, such as Semi-Inclusive Deep Inelastic Scattering, an impact parameter dependence on the scale of the proton can be taken into account. However, such a dependence lies outside the scope of this thesis.

1.1.2.2 Evolution of heavy-ion collisions

As mentioned before, the QGP can be created by colliding ultrarelativistic heavy ions. The time evolution of such collisions, from the moment the ions collide up to the detection of particles in experiments will now be detailed. Several phases occur following the collisions [5, 6], shown in Figure 1.4.

Due to Lorentz contraction, the heavy ions are essentially flat discs. For large nuclei such as gold (Au) used at RHIC and lead (Pb) used at the LHC, the diameter is 14 fm. The thickness of the discs is $14/\gamma$ fm, where γ is the Lorentz factor, equivalent to 100 and 2500 at the highest RHIC, respectively LHC energies. As the heavy ions collide, many interactions occur at soft scales (i.e. at low momentum transfer), while some occur at hard scales. The hard interactions are responsible for the production of particles with large transverse momentum, which are called hard particles or hard probes.

1 fm/c after the collision, after the hard particles have been produced, the energy density rises to about 12

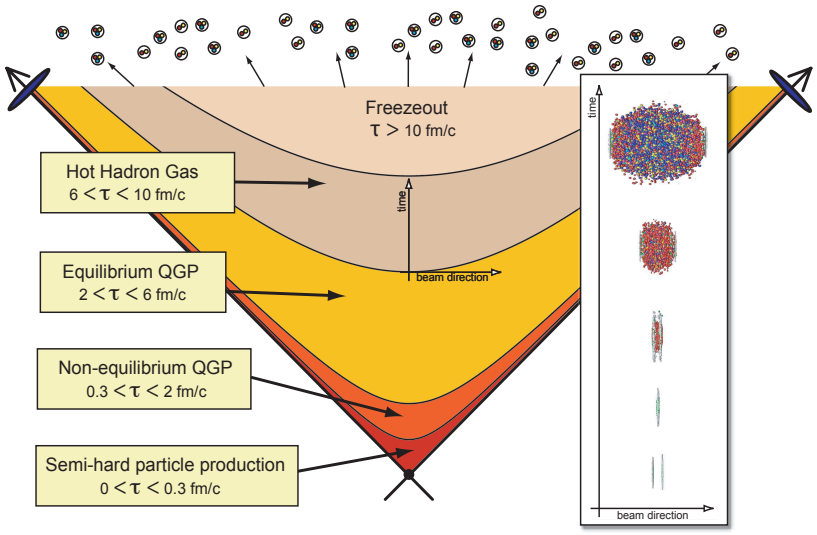

Figure 1.4: Time evolution of a heavy-ion collision, where the indicated timescales are rough guidelines. Figure taken from [6].

GeV/fm^3. This is more than twenty times the average energy density inside a hadron. The corresponding high temperature and parton density lead to the formation of a QGP that is out of equilibrium. Although hydrodynamical models can be used at this stage, their applicability and reliability is not well established.

The next stage is that of a hydrodynamic QGP. Even though quarks and gluons are deconfined in the QGP, they are not independent. One surprise was the discovery that quarks and gluons in the QGP behave like a strongly coupled fluid, instead of like a gas-like fireball. The hydrodynamic phase is described by linearised viscous hydrodynamics in which the QGP expands due to its high initial pressure after which it cools down.

The hydrodynamic expansion phase lasts until the temperature becomes so low that quarks and gluons again become confined within hadrons, which signals the formation of a hot hadron gas. The hadron gas further cools down, while interactions between particles are still taking place. At some point, inelastic collisions no longer occur so that the chemical composition of outgoing particles is fixed. This is called the chemical freeze-out. The hadrons can still interact elastically, which can modify for example their p_{T} spectra. Lastly, the kinetic freeze-out indicates that even elastic collisions no longer take place. After the kinetic freeze-out, particles free stream to detectors where they can be measured.

1.1.2.3 Probes of the QGP

Because the lifetime of the QGP is extremely short ($\sim$10 fm/c at the LHC, $\sim$6 fm/c at RHIC [7]), it cannot be directly observed. However, its presence and properties can be inferred from a multitude of measurements. In this subsection, a small selection of such measurements is discussed. It is by no means a complete summary of QGP probes and is only intended to briefly sketch the variety of measurements. An interested reader is invited to read Refs. [3, 5, 8] and references therein for more detailed information. The characterization of the QGP can be

divided in roughly two categories of probes: hard and soft probes. The separation between the two is based on the momentum transfer scales involved in the partonic scatterings. Hard probes involve momentum transfer scales much larger than any energy scales present in the QGP medium and strictly originate from the initial nucleon–nucleon collisions. Because they are formed earliest, they can traverse the QGP and interact with it. Moreover, due to the large energy scales involved, their production can be computed within the pQCD framework which allows for first-principle computations. On the other hand, soft probes elucidate bulk and dynamic properties of the QGP and generally involve non-perturbative QCD.

Hard probes

High-p_{T} photons and EW bosons have been extensively studied in a multitude of collision configurations. In pp collisons, their production cross section agrees well with pQCD calculations. In nucleus–nucleus (AA) collisions, their production matches with expectations from the yield in pp collisions scaled by the number of binary collisions $\langle N_{\mathrm{coll}} \rangle$ (also taking into account nuclear modifications of parton densities). Because both photons and the Z boson lack color charge, this shows an understanding of the production mechanisms in pp and also provides credence for the determination of $\langle N_{\mathrm{coll}} \rangle$ using the Glauber MC. The production of Z bosons and nuclear modifications of parton densities are an integral part of this thesis and will be outlined in more detail later.

The comparison with colored probes such as jets, high-p_{T} hadrons and heavy quarks then can provide information about how the strongly interacting QGP affects colored probes that traverse it. When comparing yields of these colored hard probes in AA collisions to those in pp (scaled by $\langle N_{\mathrm{coll}} \rangle$), it has been found that they are suppressed in AA collisions. This phenomenon is called jet quenching, and arises from energy loss due to interactions with the QGP.

Soft probes

Particle correlations have been measured in AA and pp collisions. It has been observed that correlations are stronger in AA collisions than what can be expected from a superposition of proton–proton collisions. The strength of these correlations provide evidence for collective behavior in AA collisions due to the QGP. Azimuthal correlations have been studied as a function of centrality, particle type, collision energy, rapidity and transverse momentum. The observations can be described by relativistic hydrodynamics if the presence of a relativistic liquid is assumed. From the measurement of azimuthal anisotropies, it has been established that the QGP does indeed behave like a liquid. Moreover, it has an extremely low viscosity. The low viscosity allows for initial spatial anisotropies (due to local fluctuations in nucleon density in the heavy ions) to persist to final state momentum anisotropies through pressure-driven expansion of the liquid.

1.1.2.4 Recent developments in small systems

It is not sufficient to only study collisions between heavy nuclei to understand the QGP. Production mechanisms can change due to nuclear environments, such that the description of proton–nucleus (pA) collisions already deviates

from that in pp collisions. Therefore, measurements of the same probe are generally done in three collision systems: proton–proton, proton–nucleus and nucleus–nucleus. The measurement in pp is considered as the baseline reference, the measurement in pA as the baseline for cold nuclear matter effects (i.e. not due to the hot and dense QGP) and AA signals the onset of QGP phenomena. In small systems (pp and pA), no QGP was originally expected to form.

However, in 2010 measurements showed that when selecting pp collisions with very high multiplicity, angular correlations typically attributed to QGP could be observed [9]. The same behavior has since then also been observed in high-multiplicity pA collisions (see [10] for an overview). Additionally, in 2016 it was observed that an enhancement of strange hadrons, also typically associated with the presence of the QGP, could be found in high-multiplicity pp and pA collisions [11]. The observation of such phenomena in small systems challenges the notion that in these collision systems no QGP should be formed. It should be noted that these high-multiplicity events constitute a small fraction of the total number of pp events ($\mathcal{O}(1\%)$) [12], so pp collisions can still safely be regarded as a baseline without collective phenomena. The observations have encouraged new investigations to the minimum size necessary for QGP formation, as well as how large energy densities could be created in pp collisions. A framework that could potentially explain the phenomena is that of multi-parton interactions (MPI) [13]. The MPI framework is based on the observation that at large energies, parton densities grow very rapidly. As a result, the probability for several parton scatterings to occur during a single pp or pA collision increases. The scatterings can occur either at soft or hard scales. Although the MPI framework predates the observations of the aforementioned azimuthal correlations and strangeness enhancement, it has been suggested that it could be used to explain them. Much experimental and theoretical effort is being put forward into understanding the appearance of collective phenomena in these small systems [3, 14].

1.2 Particle production in proton–proton collisions

In the previous section, the running of the QCD coupling α_s was discussed. At large momentum transfer, the value of α_s is small which allows for the computation of partonic cross sections using perturbative expansions. However, free quarks and gluons do not exist in nature. Due to long-range interactions that occur at large values of α_s, partons are confined within hadrons. Perturbative QCD does not work for these large values of α_s as higher order diagrams are no longer negligible, leading to divergence of perturbative series. This poses an interesting challenge in the computation of cross sections in QCD processes in hadron collisions, such as at the LHC.

One of the frameworks thas has been established to nevertheless compute hadronic cross sections is the collinear factorisation framework. In the collinear factorisation framework, hadronic cross sections are calculated as the convolution of partonic cross sections with non-perturbative objects called parton distribution functions $f_i\left(x, Q^2\right)$. Here, x is momentum fraction of the parton (also known as bjorken-x), Q^2 is the square of the mo-

mentum transfer, which indicates the energy scale of the interaction, and i indicates the parton flavor, which can be either a quark or a gluon. The PDFs describe the number density (or more roughly speaking, the probability) of a parton i at an energy scale Q^2. The PDFs describe the long-distance proton structure and are inherently non-perturbative objects, so they cannot be computed from first principles. Instead, they are obtained through global fits to various data from a multitude of experiments, including Deep Inelastic Scattering (DIS), Drell-Yan production of electroweak bosons, jets and top quark pair production. Hadronic cross sections can then be obtained by [15]

$$\sigma = \sum_{a,b} \int dx_a \int dx_b f_a\left(x_a, \mu_F^2\right) f_b\left(x_b, \mu_F^2\right) \hat{\sigma}_{a,b,x_a,x_b,\mu_F^2} + \mathcal{O}\left(M/Q\right) \tag{1.3}$$

where σ is the hadronic cross section, a and b are partons, f are PDFs which give the parton densities of momentum fractions x_a and x_b evaluated at a factorisation scale of μ_F^2, $\hat{\sigma}$ is the partonic cross section for a given combination of mentioned variables and M represents the confinement scale, $M \sim 0.3$ GeV. The factorisation scale μ_F^2 indicates the scale at which the PDFs are evaluated, and is typically set equal to the momentum transfer scale Q^2. The term factorisation is used frequently in physics, where it indicates that a quantity can be computed as the convolution of several factors. To be precise, Eq. 1.3 refers specifically to inclusive collinear factorisation [15]. The term *inclusive* pertains to a technical detail relating to the cancellation of infrared infinities due to the emission of soft partons. An intuitive interpretation of Eq. 1.3 is that the hadronic cross section is given by partonic cross sections $\hat{\sigma}$ for partons a and b, multiplied by the probabilities to find said partons (given by the PDFs), integrated over all values of momentum fraction x.

Before showing recent results from PDF fits, some technical aspects of factorisation are discussed. Firstly, it should be noted that factorisation applies specifically to hard probes, where the partonic cross section can indeed be computed using perturbative QCD. Secondly, factorisation relies on the principle that there is a separation between the timescales in a hadron collision. An intuitive 'proof' for factorisation is that the correlations of the momentum distributions occur on long timescales, so that during the short timescale of the collision, the distributions can be considered frozen [15]. However, formal proofs are mathematically very demanding and only exist in a limited number of cases [16]. In general, factorisation is assumed and justified in retrospect if the theory describes the data well. Thirdly, an important aspect of factorisation is that PDFs are assumed universal because they describe the proton structure. They should therefore not depend on any specific hard process, and the same PDFs determined from electron-proton DIS at HERA should be applicable in hadron collisions at the LHC. Lastly, the PDFs depend on the momentum transfer scale Q^2. Normally this would mean that one would have to obtain each PDF at various Q^2 to obtain the full dependence. Fortunately, a set of equations called the Dokshitzer–Gribov–Lipatov–Altarelli–Parisi (DGLAP) equations, can be used to obtain the Q^2 evolution of the PDFs given a starting scale Q_0^2 [17–20].

Figure 1.5 shows the most recent proton PDFs obtained by the CTEQ-TEA collaboration, evaluated at NNLO [21]. The PDFs are shown at two different energy/factorisation scales, which show qualitative similarities. At both energy

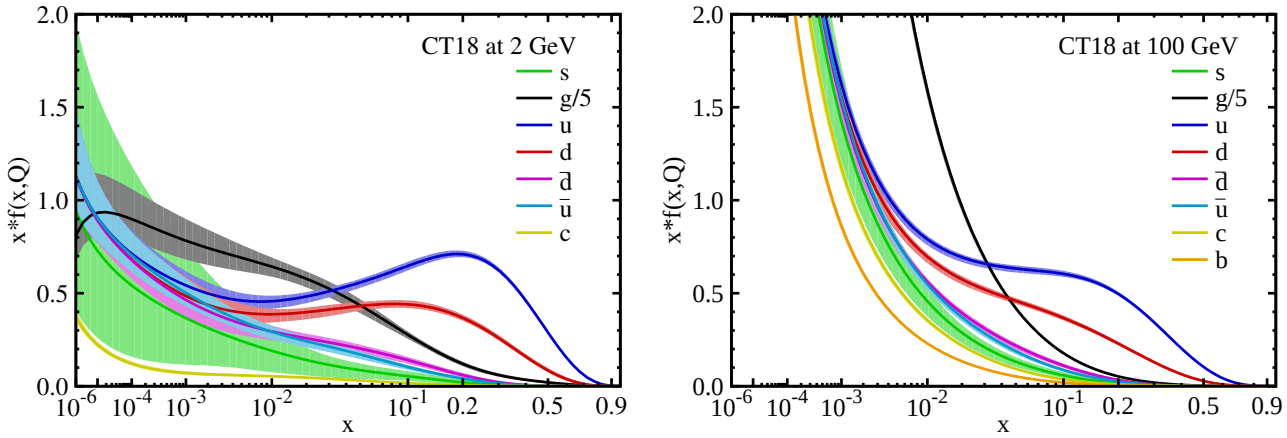

Figure 1.5: CT18NNLO proton PDFs as a function of Bjorken-x at $Q = 2$ GeV (left) and $Q = 100$ GeV (right). Figure taken from [21].

scales, there are two bumps visible at $x \approx 1/3$ for the up and down quark distributions which correspond to the valence quarks. Moving to lower x values, the density of all partons increases. In particular, the gluon PDFs grow rapidly. Even though the gluon PDFs are divided by 5 for visibility, they dominate the other partons, especially at large momentum transfer, as seen on the right plot.

The increase of the PDFs at low x can be understood intuitively as follows. The value of Bjorken-x can be shown to be approximately equal to Q^2/s where s is the center-of-mass energy of the colliding partons [22]. For a fixed Q^2, low x therefore corresponds to a large center-of-mass energy. For ultrarelativistic particles, the center-of-mass energy is proportional to the Lorentz boost γ. Because internal timescales are dilated by the γ factor, a larger γ factor increases the lifetime of the QCD fluctuations (i.e. the gluons and sea quarks). As the lifetime of the fluctuations grows, the probability for an interaction between a fluctuation and a probe increases. The end result is that the proton is a denser object at higher energies and by correspondence lower bjorken-x.

A separate factorization framework called the k_T-factorisation exists, specifically for the computation of low-x physics. Instead of an evolution in Q^2, the PDFs are evolved in x, given by the the Balitsky-Fadin-Kuraev-Lipatov (BFKL) equation, which is a linear equation [23]. Some theories predict that the rise of the gluon PDFs at lower x does not continue indefinitely. Instead, at some point the gluon fusion cross section should become equal to gluon splitting cross section. This leads to a saturation of the gluon density, and the domain of physics is therefore called saturation physics. One framework designed to understand and describe saturation physics is the Color-Glass Condensate (CGC) model, which introduces non-linear effects to the BFKL equation at large gluon densities [24]. In this thesis however, the focus lies on the inclusive collinear factorization.

Inclusive collinear factorisation in hadron collisions (as given by Eq. 1.3) is the starting point for the computation of cross sections of hard probes. In the following, the production and decay of the Z boson and the J/ψ meson will be discussed separately in more detail.

1.2.1 Z bosons

1.2.1.1 History and significance

The following is a condensed timeline of the theoretical conception and experimental discovery of the Z boson. The information is principally taken from Refs [25] and [26]. An interested reader is invited to read them and references therein for more detailed information.

Already in 1934, long before the advent of the Standard Model, E. Fermi put forward an effective theory of the weak force to describe β decays. In his effective theory, only charged weak interactions were considered. Some 30 years later in 1958, S. Bluman attempted to create a gauge theory describing weak interactions. The gauge theory naturally led to the prediction of weak neutral currents. Shortly after in 1961, S. Glashow proposed an electroweak theory to unify QED (electromagnetic) and weak interactions. As for Bluman's theory, this required the presence of a massive neutral boson, although at the time no mechanism was known to give rise to vector boson masses without breaking certain symmetries in the theory. In 1964, R. Brout, F. Englert and P. Higgs presented the mechanism of spontaneous symmetry breaking. Through this mechanism, bosons could gain mass without breaking the gauge theory. The mechanism was used simultaneously in 1967 by S. Weinberg and A. Salam in what can be considered a precursor to the Standard Model, the Glashow-Salam-Weinberg model. The theory necessitated both a neutral boson, which had still not yet been experimentally observed, as well as a boson related to the symmetry breaking. The first experimental discovery of weak neutral currents was finally made in 1973 in the Gargamelle bubble chamber experiment at CERN. Using a neutrino beam and a bubble chamber, neutrino–electron and neutrino–hadron elastic collisions were observed. Ten years later in 1983, the first experimental discovery of the W and Z bosons was made by the UA1 and UA2 collaborations at the Sp$\bar{\text{p}}$S collider at CERN. The discovery of the three electroweak bosons was a crucial milestone that cemented the Standard Model as the correct description of electroweak interactions. Lastly, the discovery of the Higgs boson in 2012 served as yet another confirmation of the correctness of the Standard Model.

After their discovery, the EW bosons were used to do precision measurements of SM predictions at the LEP and SLAC colliders in the 1990s. For example, in the SM, EW couplings to electrons, muons and tauons are exactly identical. This assumption is called lepton flavor universality, and was found to hold [27] (although later measurements found a $2.6\ \sigma$ discrepancy [28]). Another example is the invisible width of the Z boson, where SM calculations showed good agreement with measured values. The invisible width of the Z boson is an interesting quantity because it can be used to extrapolate the number of neutrino families. The theory predicts, and measurements show that this number should be 3, which is also the number of families that have been observed so far.

1.2.1.2 Properties

Z bosons are the force carriers of the electroweak force, together with the W bosons and photons. They carry the same quantum numbers of spin (+1) and electric charge (0) as the photon and carry no color charge. In contrast to the massless photons, Z bosons have a mass of 91.1876 ± 0.0021 GeV/c^2 [2].

An aspect of Z bosons that makes them useful in experiments is their experimental signature. They can decay into a pair of high-p_{T} leptons with opposite sign with a branching ratio of $3.3662 \pm 0.0066\%$ [2]. Furthermore, the decay products of Z bosons are in a kinematic regime where there is little background. In addition to that, their cross sections at LHC energies are large, so that Z bosons can be measured experimentally with high precision. Because the cross sections can be measured with high precision and theoretical predictions from QCD (discussed in the next subsection) can be done with high accuracy, Z boson production can be used to calibrate detectors. As such, the Z bosons (and also W bosons) have been nicknamed the 'standard candles' of the LHC [21, 29]. An LHCb measurement of Z bosons at forward rapidity and an ATLAS measurement of Z and W bosons at central rapidity, both for pp collisions at $\sqrt{s} = 13\,\mathrm{TeV}$ are shown in Fig. 1.6 [30, 31]. Within uncertainties, the data are well described by pQCD calculations at next-to-next-to-leading order (NNLO) in QCD and next-to-leading order (NLO) in QED.

1.2.1.3 Production mechanism

Z bosons are mainly produced through quark–antiquark annihilation, at the LHC. A special name is given to the process where the Z boson subsequently decays to a lepton pair, namely the Drell-Yan process [32]. The Drell-Yan process, shown in Figure 1.7 is a purely EW process at LO. Because the Z boson and photon have identical quantum numbers, the Drell-Yan process can also occur through an intermediary virtual photon instead of a Z boson.

The large mass of the Z boson has two consequences. First, even at the large LHC energies, Z bosons are exclusively produced in the initial hard scatterings (in contrast to low-mass particles that can be produced thermally or from initial/final state radiation). Secondly, the large mass of the Z boson requires a large momentum transfer. Because α_s is small at the Z boson mass ($\alpha_s = 0.1179 \pm 0.0010$ [2]), a perturbative expansion in α_s can be done. This is necessary for the computation of QCD corrections to the production cross section, which are generally larger than QED corrections. For comparison, the value of the QED coupling constant α at the Z-boson mass is $\alpha = \frac{1}{127.952 \pm 0.009} \approx 0.0078$ [2]. QCD corrections have been calculated up to NNLO, including a fully differential description of the decay leptons [34]. NLO EW corrections have also been computed, which are comparable in size to the NNLO QCD corrections (a rule of thumb is that $\alpha_s^2 \approx \alpha$). Partial results of N3LO QCD corrections, as well as mixed QCD-EW $\mathcal{O}(\alpha_s \alpha)$ have already been obtained and full corrections are ongoing [35].

As was mentioned before, the intermediary boson in the Drell-Yan process can be either a Z boson or a virtual photon. Because the two processes $q\bar{q} \to \mathrm{Z} \to \mu\mu$ and $q\bar{q} \to \gamma^* \to \mu\mu$ are physically indistinguishable, they must both be included in production cross sections. In the theoretical computation of the cross section, their scattering

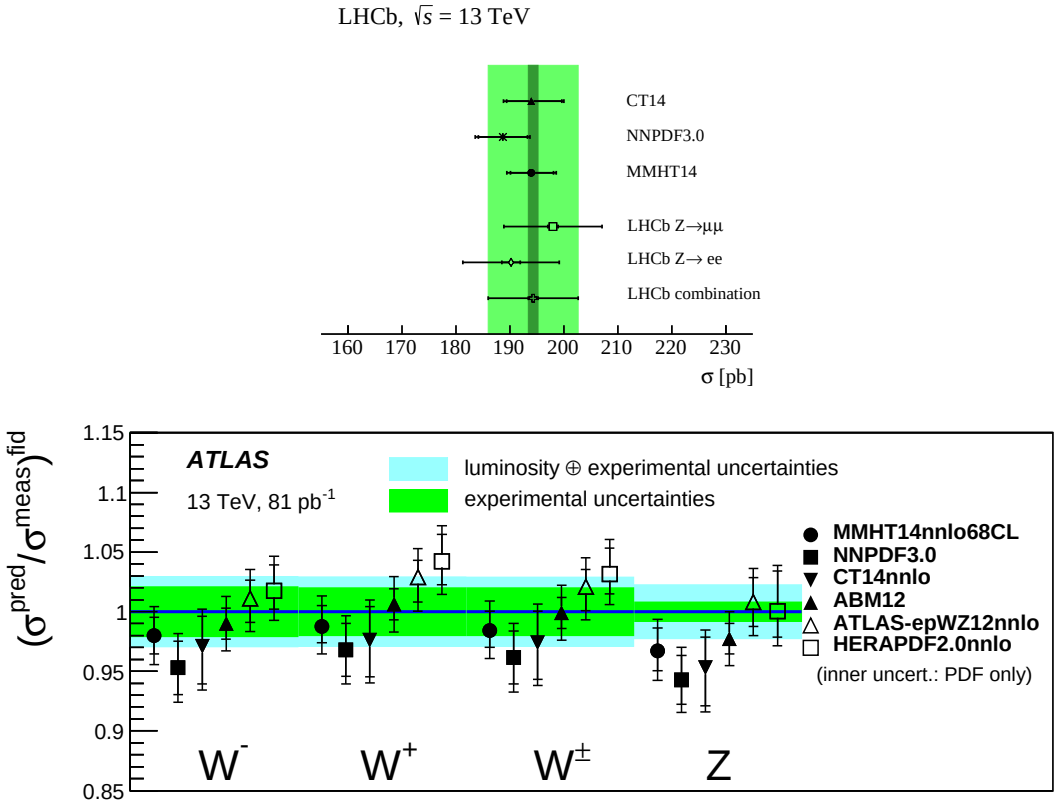

Figure 1.6: Cross section measurement in pp collisions at $\sqrt{s} = 13\,\mathrm{TeV}$. The upper plot shows the fiducial Z boson cross section measured by LHCb, while the lower plot shows the fiducial Z and W cross sections measured by ATLAS. Figures taken from [30] and [31].

matrix elements will interfere and this influences the Drell-Yan production cross section. This means that strictly speaking, although the term Z boson production is used in this thesis, the actual measured production is that of Z bosons and virtual photons (in other words, the Drell-Yan production). The invariant mass spectra of the two processes differ, because the Z-boson process produces a resonance peak while the γ^* produces a continuous spectrum that decreases towards higher masses. Figure 1.8 shows both the continuum and resonance contributions of the Drell-Yan process, measured by CMS in pp collisions at $\sqrt{s} = 13\,\mathrm{TeV}$. The data are compared to NNLO QCD + NLO EW computations, which show remarkable agreement over a wide range of invariant mass [36].

1.2.2 J/ψ

1.2.2.1 History and significance

The following is a condensed timeline of the theoretical conception and experimental discovery of the J/ψ. The information is principally taken from Refs [37–39]. An interested reader is invited to read them and references therein for more detailed information.

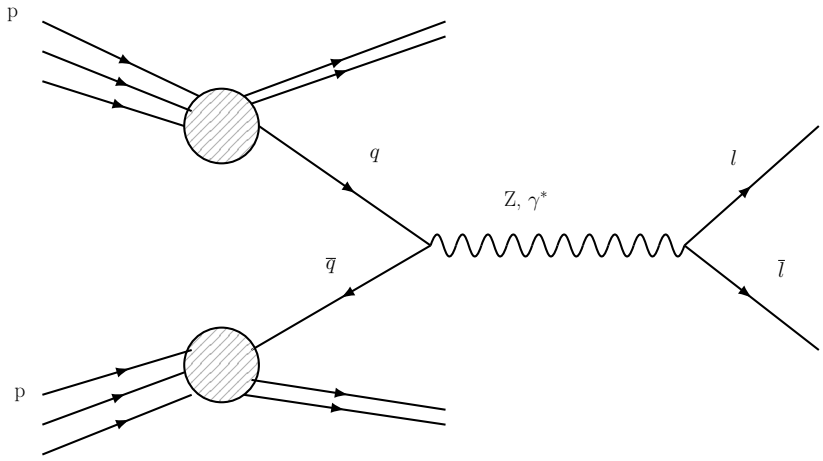

Figure 1.7: Drell-Yan process, in which a quark-antiquark pair from two hadrons annihilates into a virtual photon or Z boson that decays into a lepton pair. Figure made using [33].

During the 1950s and 1960s, large numbers of new particles were being detected. Suspecting that these particles were not elementary but rather composite, M. Gell-Man and G. Zweig introduced the quark model of hadrons in 1964. In the model, three quarks (up, down and strange) were considered as the building blocks of all observed hadrons. The quark model was able to explain measured meson and baryon spectra at the time. However, isolated quarks had never been experimentally observed (which is now understood to be impossible due to confinement). It was therefore not clear whether these quarks were mathematical book keeping tools or represented physical particles. In addition to the quarks, the existence of four leptons (electrons, muons and their neutrino's) had been established.

The quark model was able to explain many weak amplitudes, but there was a notable exception. It predicted strangeness changing neutral currents, but experimentally these were not observed. In 1970, S. Glashow, J. Iliopoulos and L. Maiani proposed the GIM mechanism that could explain the reason for this suppression[2]. In order to do so however, they required the existence of a fourth quark with charge $2/3e$. Four years later in 1974, the J/ψ meson was experimentally observed for the first time. The observation was done simultaneously by two separate research groups at Brookhaven National Laboratory and Stanford Linear Accelerator. In their publications, the particle was named J and ψ respectively. Ultimately, both names were kept, leading to the name J/ψ.

One surprising aspect of the J/ψ was its extremely narrow decay width and therefore long lifetime. For comparison, other mesons which were known at the time, such as the ρ, ω and ϕ have masses around 1 GeV/c^2, close to the J/ψ mass. Their lifetimes on the other hand, are three orders of magnitude smaller than that of the J/ψ. This triggered lot of theoretical speculation and experimental activity. In the following year, more than 700 papers were written related to the discovery of the J/ψ. This is now known as the November Revolution of 1974. In the end, the discovery of the J/ψ played a fundamental role in the acceptance of quarks beyond mere bookkeeping tools and consequently in the understanding of the fundamental structure of Nature.

[2]The GIM mechanism also predicted the presence of neutral currents, mediated by a neutral weak boson.

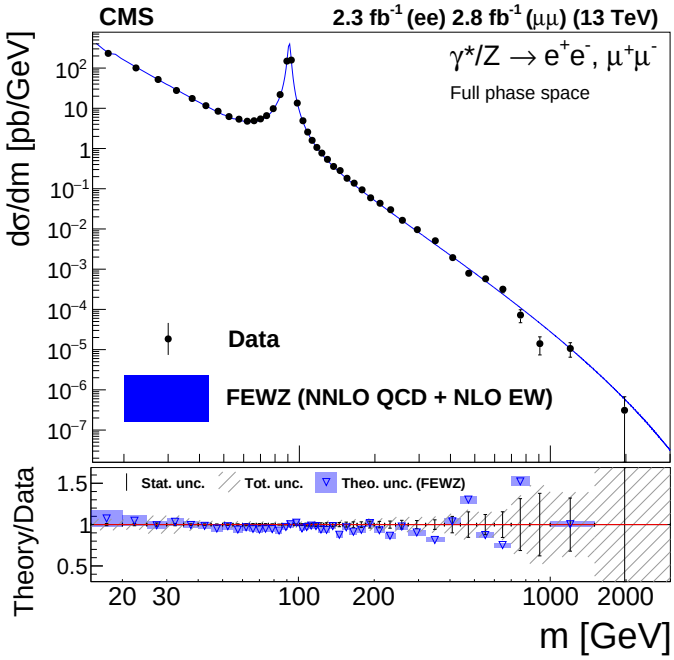

Figure 1.8: Drell-Yan production cross section as a function of invariant mass in pp collisions at $\sqrt{s} = 13\,\mathrm{TeV}$ for the leptonic decay channels. Both the virtual photon continuum contribution as well as the Z-boson resonance peak are visible. A comparison is made with theoretical calculations, showing good agreement with the Standard Model predictions. Figure taken from Ref. [36].

1.2.2.2 Properties

Bound states of heavy quark and antiquark pairs are generally labeled quarkonium (plural: quarkonia). More specific names corresponding to the quark flavors are commonly used, such as charmonia for charm-anticharm bound states and bottomonia for bottom-antibottom bound states. Due to the large masses of c and b quarks, dynamical properties of charmonia and bottomonia can be described by a non-relativistic potential model, called the Cornell potential [40]. The Cornell potential is given by

$$V_{\mathbf{Cornell}}(r) = \sigma r - \frac{\kappa}{r} \tag{1.4}$$

where σ and κ are constants of the potential and r is the radial separation of the quarks. At short distances, interactions are dominated by high-energy gluon exchanges so that the dynamics are perturbative. This leads to a Coulomb-like $\frac{\kappa}{r}$ term in the potential. At long distances however, non-perturbative effects such as confinement are modelled by a linear term in the potential. Similarly to the non-relativistic hydrogen atom, or positronium (which are also two-particle bound states), many different states exist, giving rise to an emission spectrum. Using the Cornell potential, a similar spectrum of charmonium can be computed, shown in Figure 1.9.

The various charmonia are described by several distinct quantum numbers. States are described in spectroscopic notation as $(n+1)^{2S+1}L_J$, where n indicates the principal quantum number, S the spin of the quarkonium,

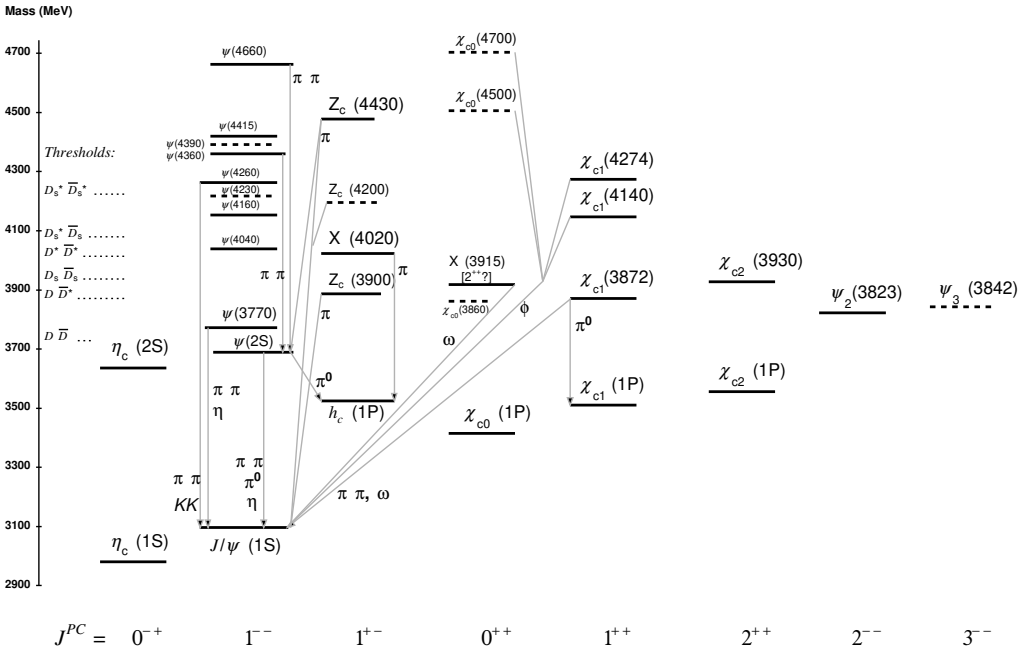

Figure 1.9: Spectroscopy of the charmonium family. Certain single photon transitions have been left out for clarity. Figure taken from [2].

L the orbital angular momentum and J the total angular momentum $L + S$. Quarkonia consist of a pair of quarks, so that they can be either in a spin singlet ($S = 0$) or spin triplet ($S = 1$) state. The allowed values of the angular momentum L are $0, 1, 2..$, but they are generally denoted by the letters $S, P, D...$ In the spectroscopic notation, the J/ψ is denoted as 1^3S_1. Alternatively, quarkonia can be classified by their parity P and charge conjugation C quantum numbers, written as J^{PC}. These are related to the values of angular momentum and spin by $P = (-1)^{L+1}$ and $C = (-1)^{L+S}$. Quarkonia with the same J^{PC} can have different values of n, which indicate excitations. This is the case for the $\Psi(2S)$ state, which is an excited state of the J/ψ (the J/ψ is also named the $\Psi(1S)$ state).

Although the J/ψ is a hadron, and can therefore decay strongly, it has a relatively long lifetime. There are several reasons for this. First, the mass of the J/ψ is lower than that of any open charm mesons, which forbids decays to other charmed mesons. Secondly, the J/ψ cannot decay into a single gluon, as the J/ψ is in a color singlet state, while gluons are color octet states. Lastly, the strong interaction preserves charge parity C. Both the J/ψ and the gluon have $C = -1$. C-parity is multiplicative, so a pair of gluons has $C = +1$, prohibiting the decay. The LO gluon decay is therefore a decay into three gluons. The matrix element computed in Feynman diagrams is therefore proportional to α_s^3, suppressing the decays. As a result, EM decays become competitive with strong decays, leading to a large branching ratio to muons of 5.961 ± 0.033 % [2].

Another property of the J/ψ that can be measured and predicted is its polarisation. The J/ψ is a massive particle with $J = 1$. If hypothetically the angular momentum were to be measured along a chosen quantisation axis z, the projected angular momentum J_z could take on the values $-1, 0, +1$. If specific values of J_z are preferred over others,

the J/ψ is said to be polarized. If the preferred values are $J_z = \pm 1$, the J/ψ is said to be transversely polarized, while a preference for $J_z = 0$ is denoted as longitudinal polarization. If there is no preference, the J/ψ is said to be unpolarized [41]. Because J/ψ's are extremely shortlived, no such measurement can be done. However, the polarization of J/ψ's affects the angular distribution of their decay leptons. Because different production mechanisms (discussed in the following subsection) predict different values of polarisation, measurements can be used to differentiate between production models. Polarization is generally described by three parameters, $\lambda_\theta, \lambda_\phi, \lambda_{\theta\phi}$, where θ is the polar angle between the positive lepton and the chosen quantisation axis and ϕ azimuthal with respect to the hadron–collision plane. The interpretation of these parameters depends on the quantization axis (or reference frame) chosen. In the helicity frame, where the angular momentum is measured with respect to the momentum direction, transversely polarised states are represented by $\lambda_\theta = 1, \lambda_\phi = \lambda_{\theta\phi} = 0$, while $\lambda_\theta = -1, \lambda_\phi = \lambda_{\theta\phi} = 0$ represents longitudinally polarised states and $\lambda_\theta = \lambda_\phi = \lambda_{\theta\phi} = 0$ represents unpolarised states. They affect the angular distribution of the leptons through [42]

$$\frac{d^2N}{d\cos\theta d\phi} \propto 1 + \lambda_\theta \cos^2\theta + \lambda_\phi \sin^2\theta \cos 2\phi + \lambda_{\theta\phi} \sin 2\theta \cos\phi \,. \tag{1.5}$$

1.2.2.3 Production mechanisms

There are multiple ways through which J/ψ's can be produced in pp collisions, and in the literature, several disctinctions are made. J/ψ's that are created in the initial pp collisions are called direct prompt J/ψ's. J/ψ's are also produced in decays of other quarkonia, such as the $\Psi(2S)$ and χ_c mesons. These are referred to as indirect prompt J/ψ's, providing feed-down contributions. Both direct and indirect prompt J/ψ's, are produced through the production mechanisms detailed in this subsubsection. It is also possible for B hadrons to weakly decay into J/ψ's, which is called non-prompt production. Non-prompt production does not occur through charmonium production, and is therefore sensitive to different physical processes. Because they decay weakly, B hadrons have relatively long lifetimes, which causes the decay vertex to be displaced by hundreds of microns [43]. Non-prompt production can therefore experimentally be separated, given a detector with good vertex resolution. Lastly, the term inclusive J/ψ production indicates that no separation between direct/indirect or prompt/non-prompt is made. The fraction of non-prompt over inclusive J/ψ has been measured as a function of p_{T} at different energies and rapidity windows. At $p_{\mathrm{T}}{\sim}1$ GeV/c, the fraction is roughly 10% and steadily grows to 25% at $p_{\mathrm{T}}{\sim}10$ GeV/c. From there, the increase becomes stronger and at $p_{\mathrm{T}}{\sim}40$ GeV/c, the non-prompt fraction is about 60% [44, 45].

At the LHC, prompt J/ψ's are mainly produced through gluon fusion [46] and their production can be described by factorisation formulas such as Eq.1.3, similar to the production of Z bosons. One crucial difference however, is that J/ψ's are hadrons. This complicates the calculation of production cross sections, because after the formation of a $c\bar{c}$ pair, the pair needs to hadronise (i.e. form a bound state). Hadronisation occurs at low energy scales and is therefore a non-perturbative process. This makes J/ψ (and quarkonia in general) production an ideal laboratory

to test the interplay between perturbative and non-perturbative QCD [47]. Several models have been created to describe J/ψ production in hadronic collisions. In the following, the three main production models of quarkonium are discussed. The three different models differ mainly in the way they treat hadronisation. They are the Color Singlet Model (CSM), Color Evaporation Model (CEM) and effective field theory of non-relativistic QCD (NRQCD).

Color Singlet Model (CSM)

Proposed already one year after the official discovery of the J/ψ in 1975, the color singlet model provided the first evaluations of quarkonium production. In the CSM, it is assumed that the quantum numbers for colour and spin of the quarkonium pair do not change during hadronisation. In other words, the heavy quark pairs are by assumption produced in the color singlet state (i.e. colourless, as must be the case for physical hadrons), hence the name of the model. The additional assumption is made that in the inertial frame of the quarkonium, both quarkonia are at rest. Hadronisation is then described by a quarkonium wave function that is process and flavor independent. The hadronic production cross section can then be calculated as [42]

$$\sigma\left[\mathcal{Q}+X\right]=\sum_{a,b}\int dx_a\int dx_b f_{a/A}\left(x_a,\mu_F^2\right)f_{b/B}\left(x_b,\mu_F^2\right)\hat{\sigma}_{a,b,x_a,x_b,\mu_F^2}|R(0)|^2 \tag{1.6}$$

where $\mathcal{Q}$ represents a quarkonium, R is the universal wave function, and all other indices are identical to those in Eq. 1.3. The two formulae are in principle identical, beside the addition of the wave function.

An attractive feature of the CSM is that the aforementioned wave function is universal. It does not change between processes or kinematic regimes, so that the same wave function can be used to describe the production of J/ψ, $\Psi(2S)$, $\Upsilon(1S)$, $\Upsilon(2S)$ and $\Upsilon(3S)$ which are the $^3S_1$ states as well as η_c and η_b which are singlet states. The wave function is non-perturbative, but because it appears in decay processes, it can be extracted from decay-width measurements. Once the wave function is obtained, the CSM becomes highly predictive.

Color Evaporation Model Model (CEM)

The CEM was first introduced only 3 years after the discovery of the J/ψ, in 1977. The CEM assumes that all heavy quark pairs hadronise into quarkonia if they have an invariant mass less than the threshold of producing a pair of open heavy flavor mesons. A fundamental difference with the CSM is that the quark pair $Q\bar{Q}$ is not required to be produced with the quantum numbers of the final hadron. Instead, the quark pair can be produced in a color octet state and by emitting soft gluons (therefore non-perturbatively) lose its color. Through this process, the quark pair ends up in the color singlet state, having 'evaporated' away its color. In the CEM, the quantum numbers of the heavy quark pair and quarkonia are therefore decorrelated, and the probability for a heavy quark pair to end up in a specific state is given by $P_{\mathcal{Q}}$. This probability is assumed to be universal for each state. The production cross section in the CEM is then given by

$$\sigma\left[\mathcal{Q}+X\right]=\sum_{a,b}\int dx_a\int dx_b f_{a/A}\left(x_a,\mu_F^2\right)f_{b/B}\left(x_b,\mu_F^2\right)\hat{\sigma}_{a,b,x_a,x_b,\mu_F^2}P_{\mathcal{Q}}\int_{2m_Q}^{2m_H}\frac{d\sigma\left[Q\bar{Q}+X\right]}{dm_{Q\bar{Q}}}dm_{Q\bar{Q}}. \tag{1.7}$$

Historically, a drawback of the CEM is that it did not describe polarisation, which is an important requirement for a production model. However, recent developments have started to incorporate mechanisms through which the CEM model can yield polarised quarkonia [42].

Non-relativistic QCD (NRQCD)

In 1995, a new framework was proposed in which aspects of both CSM and CEM were included [48]. Making use of the fact that quarkonia are bound states of heavy quarks, a non-relativistic framework built on QCD was established. In NRQCD, a similar factorisation is assumed as for CSM, but instead of a universal wave function, hadronisation is described using universal long-distance matrix elements (LDME's). Hadronic production cross sections are computed as

$$\sigma\left[\mathcal{Q}+X\right]=\sum_{a,b,n}\int dx_a\int dx_b f_{a/A}\left(x_a,\mu_F^2\right)f_{b/B}\left(x_b,\mu_F^2\right)\hat{\sigma}_{a,b,x_a,x_b,\mu_F^2,\mu_\Lambda}\langle\mathcal{O}_{\mathcal{Q}}^n\rangle. \tag{1.8}$$

where the partonic cross section obtains an extra dependency on an unphysical scale μ_Λ, and $\langle\mathcal{O}_{\mathcal{Q}}^n\rangle$ represents the LDMEs.

As in the CEM, transitions from color octet states to the final physical meson are allowed. The addition of these color octet states allows for the cancellation of divergences present in the CSM. The sum in Eq. 1.8 therefore is also over the quantum numbers for spin, color and angular momentum which are all denoted by n. Obtaining the LDMEs is a more challenging task than obtaining the CSM wave functions, because LDMEs cannot be extracted from decay-width measurements or from lattice QCD calculations. Only relations from Heavy-Quark Spin Symmetry allow for the extraction of the LDMEs.

In principle, a sum over an infinite number of LDMEs must be done in order to obtain cross sections. However, the sum over n is typically organised in powers of the relative quark velocity v (in addition to the well-known expansion in α_s). NRQCD therefore uses a double expansion in v and α_s, truncating computations at a given order for either variable. If only the leading order in v is considered, and only those quantum numbers where the heavy quark pair is the same as the quarkonium, NRQCD yields the CSM predictions. The non-relativistic approach is justified through estimates of the relative quark velocities, which are $v^2\approx 0.3$ for charmonia and $v^2\approx 0.1$ for bottomonia [47]. For single inclusive J/ψ hadroproduction, relativistic corrections to the p_{T} distribution of cross sections for CS modes are negligible [49].

Current standings on production models

The LO CSM was initially successfully applied at lower energies at $\sqrt{s}=27\,\mathrm{GeV}$ and $\sqrt{s}=63\,\mathrm{GeV}$, for which

data was available up to a transverse momentum of 6 GeV/c [46, 47]. Later on however, direct J/ψ and $\psi(2S)$ measurements done by the CDF collaboration in 1992 at $\sqrt{s} = 1.08\,\mathrm{TeV}$ showed that the cross section from the CSM underestimated the data by a factor 30. This failure of the CSM to predict the p_{T} distribution of quarkonium production in turn inspired the popularity of the NRQCD model which included the COM and was better able to describe the data. In subsequent years, higher order NLO and NNLO* (i.e. partial NNLO) corrections to the CSM were computed. A striking finding is that these higher order corrections do not influence the total cross section much, although their impact on the p_{T} distributions is very significant [47]. In case the full NNLO CSM corrections are close to the partial NNLO* corrections, the CSM alone is enough to explain the p_{T} distribution at low and mid p_{T}. The significant NLO and NNLO corrections do raise doubts for the convergence of the perturbative series in α_s. Large uncertainties, both in the CSM and in the COM of NRQCD, ultimately do not allow for any strong conclusions on the dominant production mechanism. The dominance of either is important to establish what the polarisation of the J/ψ should be. Measurements indicate that J/ψ are produced unpolarised (some indicate a light longitudinal polarisation), while the CSM predicts longitudinally polarised J/ψ and the COM in NRQCD predicts transverse polarisation at high p_{T} (all in the helicity frame).

1.2.2.4 Associated production

As experimental and theoretical studies have progressed, increasingly more precise measurements and predictions have been made. However, a number of challenges still remain in the understanding of quarkonium production. New observables have been suggested, going beyond cross section measurements of single quarkonium. Instead, measurements of a quarkonium in combination with other particles (called associated production) are considered promising to a better understanding of quarkonium production mechanisms. For example, J/ψ + J/ψ production is expected to be dominated by CSM contributions while J/ψ + Υ is dominated by COM contributions [50]. Such measurements therefore provide separation power between the various single production modes. Furthermore, new constraints on NRQCD LDMEs can be obtained from associated production, as the LDMEs appear in different combinations than in single production [42]. The focus in this thesis will lie mainly on J/ψ + J/ψ pair (also called di-J/ψ) production. The production cross section for di-J/ψ production is three orders of magnitude smaller than that of single J/ψ production. A kinematical reason for this is that a larger mass needs to be produced in the collision, which thereby reduces the possible phase space. Another reason is that in perturbative computations, di-J/ψ production generally starts at a higher order in α_s, compared to single J/ψ production [51].

The production mechanisms for single J/ψ's (and quarkonia in general) have been outlined already. In all three mechanisms, J/ψ production occurs through the interaction of two initial partons. From such a single scattering, Feynman diagrams that include the production of two J/ψ's can be made. An example is shown in Fig. 1.10-left. This process is called Single Parton Scattering (SPS). At LHC energies, gluon densities of the proton are very large (as shown in Fig. 1.5) and it becomes possible for several separate parton scatterings to occur during one single

proton–proton collision. In general, this is referred to as Multi-Parton Interactions (MPI). In this thesis, the focus lies on MPI involving two separate scatterings, which is referred to as Double Parton Scattering (DPS), shown in Fig.1.10-right. In both SPS and DPS, gluon fusion is considered to be the dominant mode of production of di-J/ψ's at LHC energies [51]. Di-J/ψ production can help understand dynamics at which multiple parton scattering becomes important at LHC energies [52]. It can also be used as a tool to probe polarised gluon momentum distribution through azimuthal asymmetries, even in unpolarised protons [53].

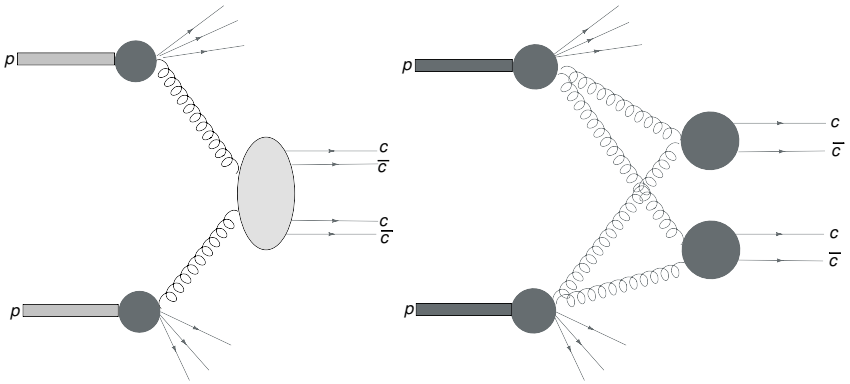

Figure 1.10: Production of two charmonium pairs, through single parton scattering (left) and double parton scattering (right). Figure taken from [54].

Although both SPS and DPS are considered to contribute to di-J/ψ production, they do so in different kinematic regimes. In the following, the SPS and DPS mechanisms will be discussed separately.

Single Parton Scattering

As for the single J/ψ production, CS and CO contributions can be computed for the di-J/ψ production cross section. However, CO contributions are generally considered negligible in SPS calculations, at least for $p_{\mathrm{T}}^{\mathrm{J}/\psi} < 50$ GeV/c [42]. Even including QCD corrections at NLO, CEM contributions remain dominated by CSM contributions. No full NLO NRQCD COM computations have been done yet, but strong similarities to the CEM computations are expected [55]. On the other hand, partial NLO evaluations, referred to as NLO* have been done for CS channels, where they were found to significantly enhance LO differential cross sections [52]. In summary, the CS contribution is expected to dominate the SPS channels of di-J/ψ production. This means that di-J/ψ production could be used to separate CS and CO production channels [56].

As mentioned before, di-J/ψ production generally occurs at higher orders of α_s. For example, the LO CSM contribution to single J/ψ production is α_s^3, while the LO contribution for di-J/ψ production in CSM instead occurs at α_s^4, as shown in Fig. 1.11.

Beside offering separation power between CS and CO contributions, di-J/ψ production can also help to constrain feeddown contributions. The initial gluons are in the color singlet state and have even C-parity. This allows for the production of J/ψ, η_c or χ_c pairs, while prohibiting the production of quarkonium pairs of different C-parity such as J/ψ + η_c or J/ψ + χ_c. This consequently affects the feeddown from J/ψ + η_c states, while η_c + η_c feeddown is

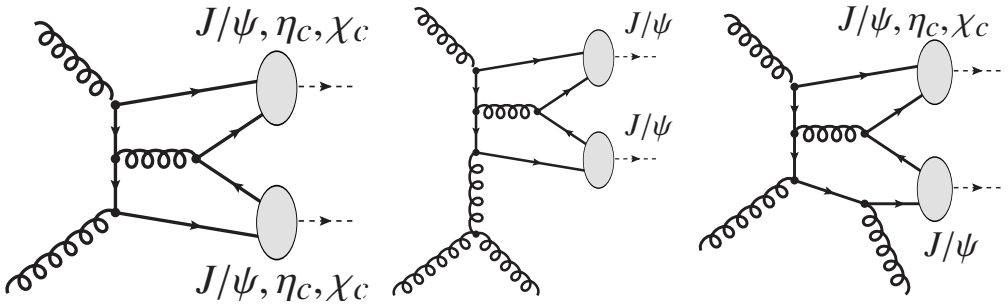

Figure 1.11: Color singlet production channels in single parton scattering. The LO contribution at $\mathcal{O}\left(\alpha_s^4\right)$ is shown on the left, while the middle and right plots show NLO contributions at $\mathcal{O}\left(\alpha_s^5\right)$. Figure taken from [42].

allowed [51]. However, it should be noted that these restrictions apply at LO only, and that at higher orders (seen on the right plot in Fig. 1.11) such mixed C-parity combinations can be produced.

Double Parton Scattering (DPS)

Typically in the framework of inclusive collinear factorisation, it is assumed that one hard scattering occurs during a hadron-hadron collision, along with multiple soft interactions. The justification for this assumption is that the probability of a single hard scattering is already small, so that the probability for two hard scatterings to occur should be highly suppressed. However, due to the large gluon densities at high energies (or conversely, low x), this assumption becomes increasingly difficult to justify [57]. At the LHC, it is expected that DPS can provide a substantial contribution to di-J/ψ production (at least in certain kinematic regimes).

In the DPS framework, it is assumed that double scatterings can be factorized as two uncorrelated SPS, in a similar way to Eq. 1.3. The general formula for the production cross section then becomes

$$\begin{aligned}\sigma^{\mathrm{DPS}}_{\mathcal{P}_1\mathcal{P}_2} &= \frac{m}{2}\sum_{i,j,k,l}\int dx_1 dx_2 dx_1' dx_2' d^2\mathbf{b}_1 d^2\mathbf{b}_2 d^2\mathbf{b} \\ &\times \Gamma_{ij}(x_1,x_2,\mathbf{b}_1,\mathbf{b}_2,\mu_{F_1}^2,\mu_{F_2}^2)\,\hat{\sigma}_{ik}^{\mathcal{P}_1}(x_1,x_1')\,\hat{\sigma}_{jl}^{\mathcal{P}_2}(x_2,x_2')\,\Gamma_{kl}(x_1',x_2',\mathbf{b}_1-\mathbf{b},\mathbf{b}_2-\mathbf{b},\mu_{F_1}^2,\mu_{F_2}^2), \qquad (1.9)\end{aligned}$$

where $\mathcal{P}$ represents an observed final state particle, the factor m is a symmetry factor equal to 1 if $\mathcal{P}_1 = \mathcal{P}_2$, and equal to 2 otherwise, and Γ is a generalised double parton distribution. The generalised double parton distribution functions depend not only on the previously introduced momentum fractions and energy scales of the two partons, but also their transverse location $\mathbf{b}$. Equation 1.9 is too complex to use, and simplifying assumptions are generally made. By assuming that the transverse and longitudinal components can be factorized, $\Gamma_{ij}(x_1,x_2,\mathbf{b}_1,\mathbf{b}_2,\mu_{F_1}^2,\mu_{F_2}^2)$ can be decomposed to

$$\Gamma_{ij}(x_1,x_2,\mathbf{b}_1,\mathbf{b}_2,\mu_{F_1}^2,\mu_{F_2}^2) = D_{ij}(x_1,x_2,\mu_{F_1}^2,\mu_{F_2}^2)T_{ij}(\mathbf{b_1},\mathbf{b_2}), \qquad (1.10)$$

where D is the double parton distribution function and T a transverse correlation function. Then, it is assumed that

there is no correlation between the partons, so that

$$D_{ij}(x_1, x_2, \mu_{F_1}^2, \mu_{F_2}^2) = f_1(x_1, \mu_{F_1}^2) f_2(x_2, \mu_{F_2}^2), \quad T_{ij}(\mathbf{b}_1, \mathbf{b}_2) = T_i(\mathbf{b}_1) T_j(\mathbf{b}_2), \tag{1.11}$$

where f_i are the single PDFs. By neglecting parton flavor dependence of the transverse correlation functions T, a single overlap function can be defined as

$$F(\mathbf{b}) = \int T(\mathbf{b}_i) T(\mathbf{b}_i - \mathbf{b}) d^2\mathbf{b}_i, \tag{1.12}$$

for which the inverse of the integral is defined as

$$\sigma_{\text{eff}} = \left[\int d^2\mathbf{b} F(\mathbf{b})^2 \right]^{-1}. \tag{1.13}$$

In the end, the so-called 'pocket formula' for DPS is obtained, given by

$$\sigma_{\mathcal{P}_1\mathcal{P}_2}^{\text{DPS}} = \frac{m}{2} \frac{\sigma_{\mathcal{P}_1} \sigma_{\mathcal{P}_2}}{\sigma_{\text{eff}}}, \tag{1.14}$$

where $\sigma_{\mathcal{P}_1}$ is the hadronic cross section for single production of $\mathcal{P}$. Given single production cross sections, the DPS cross section can be computed from Eq.1.14. From the equation, it follows directly that the spectra (versus p_{T} or rapidity) in DPS should be equivalent to those in single J/ψ. By measuring the single cross section of two particles $\sigma_{\mathcal{P}_1}$ and $\sigma_{\mathcal{P}_2}$, as well as their associated cross section $\sigma_{\mathcal{P}_1\mathcal{P}_2}$, the effective cross section σ_{eff} can be computed using Eq. 1.14. However, the DPS fraction $\sigma_{\mathcal{P}_1\mathcal{P}_2}^{\text{DPS}}$ must first be determined for this. The DPS fraction is generally estimated from template fits to the associated production [58, 59].

Equation 1.14 provides an intuitive explanation for the importance of DPS at high energies. The reason is that each of the σ's in the equation contains two parton PDFs so that the DPS cross section is roughly proportional to the fourth power of PDFs. Due to the rapid rise of the PDFs at high energy (low x), DPS is considered to grow more strongly as a function of energy than SPS [57, 60]. However, it should be noted that there are some caveats to the equation. First, although factorisation has been shown to hold in SPS, proofs in DPS are still an ongoing effort [60]. Secondly, some of the simplifying assumptions, such as the irrelevance of parton correlations have been questioned [61]. Furthermore, the given definition of σ_{eff} is computed under the assumption that it only depends on transverse correlations in proton, and should therefore be process independent. However, some tension exists between the extraction of σ_{eff} from different data sets. The extraction from processes sensitive to quark PDFs yield smaller values of σ_{eff}, than those from processes sensitive to gluon PDFs. This could potentially be rooted in a flavor dependence [43, 52].

It is currently expected that DPS contributions dominate over SPS contributions at large values of Δy between the J/ψ's and also at large di-J/ψ invariant masses $M_{J/\psi J/\psi}$ [52].

1.3 Modification of particle productions in heavy nuclei collisions

In the previous sections, production mechanisms of Z bosons and J/ψ (mesons) in proton–proton collisions were discussed. In collisions involving heavy nuclei these production mechanisms can change. Changes can occur due to final state effects, such as interactions with the QGP, or due to initial state effects from the heavy nuclei. The distinction is made between QGP-related effects, which are called hot nuclear effects and non-QGP-related effects, called cold nuclear matter effects (CNM). Although there are exceptions, proton–nucleus (pA) collisions are typically used to study CNM effects, as no QGP is expected to form in these collisions. AA collisions are sensitive to both CNM and hot effects. Measurements in all three systems (pp, pA and AA) are therefore important to disentangle the cold and hot effects from the proton–proton baseline. In the following, a selection of cold and hot nuclear matter effects are discussed.

1.3.1 Cold Nuclear Matter effects

1.3.1.1 nuclear PDFs

In 1983, the European Muon Collaboration measured the structure functions F_2 of iron and deuterium. The structure function is closely related to PDFs through $F_2(x) = \sum_q e_q^2 f_q(x)$, where e_q is the charge of a parton q and f its PDF. Theoretical expectations at the time were that the ratio of structure functions in iron and deuterium should be unity, indicating that a naive counting of nucleons should yield predictions for nuclei. However, the measurement exhibited a clear departure from unity, with a depletion in iron at large x and an enhancement at low x. Although several explanations were proposed for this departure, it has since been well established that parton distributions are different in free nucleons than nucleons bound in nuclei [62]. As a result, cross section computations in the inclusive collinear factorization framework require nuclear PDFs (nPDFs) which are different from the free-nucleon PDFs.

There are two main approaches to parametrize nuclear PDFs. The first is to define a nuclear modification ratio with respect to known proton PDFs [63]

$$f_i^{p/A}(x, Q^2) = R_i^A(x, Q^2) f_i^p(x, Q^2), \tag{1.15}$$

where i indicates a parton (either a quark or gluon), R the nuclear modification ratio, and $f^{p/A}$ and f^p the bound proton (in nucleus A) and free-proton PDFs, respectively. Alternatively, the bound proton PDF can be obtained by a direct parametrization of the distributions, in the same way as for free-nucleon PDFs [64]. An example of this is

$$x f_i^{p/A}(x, Q^2) = c_0\, x^{c_1} (1-x)^{c_2} e^{c_3 x} (1 + e^{c_4} x)^{c_{5.02}}, \tag{1.16}$$

where the A-dependence is included in the parameters $c_k(A) \equiv c_{k,0} + c_{k,1}\,(1 - A^{-c_{k,2}})$ with $k = \{1, \ldots, 5\}$.

In both approaches, the corresponding bound neutron PDFs are obtained by isospin exchange from the bound proton PDFs, i.e. by setting $u^p \overset{\text{IS}}{=} d^n$, $d^p \overset{\text{IS}}{=} u^n$, $\bar{u}^p \overset{\text{IS}}{=} \bar{d}^n$ and $\bar{d}^p \overset{\text{IS}}{=} \bar{u}^n$ [63, 64]. The PDFs of other partons are assumed to be equal between protons and neutrons. After the bound neutron PDFs $f^{n/A}$ are obtained, the nPDF of the full nucleus is computed as

$$f^A(x, Q^2) = \frac{Z}{A} f^{p/A}(x, Q^2) + \frac{A - Z}{A} f^{n/A}(x, Q^2), \tag{1.17}$$

where A and Z are the atomic mass and charge number, respectively.

An example of the nuclear modification factor $R_i^A(x, Q^2) = f_i^{p/A}(x, Q^2)/f_i^p(x, Q^2)$ is shown in Figure 1.12. Four distinct regions in x can be separated. At $x \lessapprox 0.05$, a depletion is present in bound nucleons compared to free nucleons. This region is called the shadowing region. At $0.05 \lessapprox x \lessapprox 0.3$, an enhancement in the so-called anti-shadowing region is seen. After this, the EMC region (the x-range where the original effect was measured) shows another depletion in $0.3 \lessapprox x \lessapprox 0.9$. Lastly, in the Fermi region $x \gtrapprox 0.9$, an enhancement is seen. It should be noted that the given values of the transition points between the different regions are only rough estimates. The precise values depend on the parton flavor and energy scale and are subject to uncertainties in the nPDF modeling. In some cases, even the qualitative behavior can change, and the distinction into four regions does not hold. As a sidenote, in nuclei it is possible for a parton to have $x > 1$ due to Fermi motion of nucleons in a nucleus. However, because data are generally not sufficient to constrain nPDFs at $x > 1$, nPDF models are generally presented at $0 < x < 1$ [15].

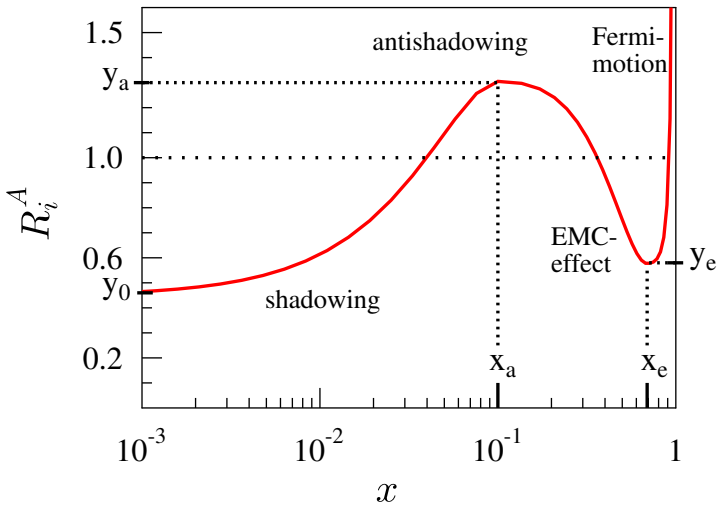

Figure 1.12: Example of the x-dependence of the nuclear modification of PDFs. The four regimes of shadowing, antishadowing, EMC and Fermi motion are indicated. Figure taken from [65].

Almost 40 years after the discovery of nuclear modifications to free-proton PDFs, the physical mechanisms responsible for the various enhancements and depletions are not yet fully understood. Shadowing and antishadowing have been proposed to originate from multiple scattering effects. The scattering amplitudes of quarks can interfere destructively, leading to a depletion (shadowing) or interfere constructively, leading to an enhancement (antishadowing) [66]. For the EMC effect, despite many proposed ideas in the 1980s, few remain viable. One possible mechanism originates from differences in the strong Lorentz scalar and vector mean fields that are known to exist in a nucleus. Another explanation comes from short-range correlations from nucleons that are far off the mass shell [67]. Lastly, the Fermi region is expected to be related to the Fermi motion of nucleons inside a nucleus [68]. Although theoretical advances have been made, the journey to a clear understanding of the physical origin of the nuclear effects is still in progress.

Nuclear PDFs, like their free-nucleon PDF counterparts, are non-perturbative objects that are obtained from global fits to data. EW bosons are sensitive to quark (and antiquark) distributions and are therefore useful tools to constrain nPDF fits. In addition to EW bosons, heavy-flavor mesons (which are sensitive to gluon distributions, particularly at low x) have been proposed to constrain nPDFs [69].

Overview of nPDF models

Throughout the years, different nPDF models have been created. They differ in the datasets included in the fits, as well as the nPDF parametrisation (as discussed before). An overview of a selection of nPDFs will now be given.

The EPS09s [70] and EPPS16 [63] are two nPDF models that are defined with respect to free-nucleon PDFs, as given by Eq. 1.15. The free-nucleon PDF set commonly used is that of CT14NLO [71]. EPPS16 is a more recent nPDF set and includes more data. Specifically, it contains data from p–Pb measurements on di-jets and W/Z bosons in LHC Run-1, as well as data from neutrino DIS experiments. Additionally, EPPS16 has independent flavor parametrization, both for valence and sea quarks. No such flavor separation is done in EPS09s, where only 3 nuclear modifications are considered: a universal modification of valence quarks, a universal modification of sea quarks and a universal modification of gluons. EPPS16 exclusively provides values integrated over the whole nucleus, meaning no impact parameter (centrality) dependence is taken into account in the nuclear modifications. In contrast, EPS09s takes into account a spatial dependence of the nPDFs and therefore is able to provide centrality dependent predictions.

The NCTEQ15 nPDFs are an independent parametrisation (i.e. no anchor PDF set is necessary), according to Eq. 1.16. Similarly to EPPS16, the NCTEQ15 nPDFs contain independent parametrization of up and down valence quarks. However, they contain no separate light sea quark parametrization which reduces theoretical uncertainties at the cost of potentially biaising the calculations. The data included in NCTEQ15 fits are similar to those included in the EPS09s nPDFs. This means that the neutrino DIS and LHC p–Pb data were not used in the fits. As was the case for EPPS16, the NCTEQ15 values are computed integrated over the entire Pb–nucleus.

As new data and theoretical techniques become available, new nPDFs are released and existing nPDFs are

updated. A brief discussion is given of nPDFs that have been released after the analysis (described in Chapter 3) was completed. A new version of the NCTEQ15 nPDFs called NCTEQ15WZ was released a year after the analysis was done [72]. In NCTEQ15WZ, LHC W and Z boson data were added to the global fits. New electroweak measurements have been performed after its release, so that not all LHC W and Z data are included in NCTEQ15WZ. The EPS09s, EPPS16 and nCTEQ15(WZ) nPDFs mentioned so far are at NLO order, but nPDFs at higher order have also been computed. One such example is the KA15 nPDF [73] whose recent successor is the KSAG20 nPDF [74]. Another nPDF, based on machine learning techniques is nNNPDF1.0 [75] is also at NNLO order. Lastly, an open-source nPDF at NNLO called TUJU has been released [76]. Although these nPDFs are computed at NNLO, the data sets used in the fits are only from deep inelastic scattering or Drell-Yan measurements. As a result, they lack certain constraints that are present in the NLO nPDFs, most notably direct gluon constraints [77]. Efforts to include a larger diversity in data are ongoing. For example, the successor of nNNPDF1.0 called nNNPDF2.0 was recently released, in which a variety of RHIC and LHC data was added to the nPDFs [78]. However, their inclusion was done at NLO. As can be seen, the development of nuclear PDFs is in constant evolution.

Table 1.1 shows an overview of the similarities and differences of the various nPDFs discussed.

1.3.1.2 Cronin effect

To quantify deviations between particle production in p–A collisions and pp collisions, the R_{pA} is used. It is defined as $R_{\mathrm{pA}} = \frac{N^{\mathrm{pA}}}{\langle T_{\mathrm{pA}} \rangle \sigma_{\mathrm{pp}}}$, where N^{pA} is the yield of an observable in p–A collisions, σ_{pp} the corresponding cross section in pp collisions and $\langle T_{\mathrm{pA}} \rangle$ the nuclear overlap function. In p–A collisions, partons from the proton can undergo multiple scattering with several partons in the nucleus, from which they gain additional transverse momentum. Consequently, in the p_{T} distribution of the R_{pA} of charged particles, a depletion is seen at low p_{T} and an enhancement at intermediate p_{T} ($\sim 3-5$ GeV/c). This is known as the Cronin effect [81]. At high p_{T}, the R_{pA} goes to unity, as so-called higher twist effects (which are responsible for multiple scattering) are suppressed by powers of p_{T}. An ALICE measurement has shown that at LHC energies, the Cronin effect is small and that the data are consistent with no enhancement at intermediate p_{T} [82].

1.3.1.3 Nuclear absorption

Even without the presence of a QGP, a quarkonium produced inside a nucleus environment can interact with the nucleons and dissociate. The consequent suppression of quarkonia is called nuclear absorption. The survival probability of a pre-resonant quarkonium is related to the absorption cross section σ_{abs} which depends on the crossing time of the collisions. The absorption cross section decreases with energy, as the crossing time decreases [83]. At LHC energies, the crossing time is expected to be so short that the quarkonia are mostly formed outside of the nuclei. As a result, nuclear absorption is expected to be negligible at the LHC [84].

	EPS09 [65, 70]	NCTEQ15 [64]	EPPS16 [63]	NCTEQ15WZ [72]	KSAS20 [74]	TUJU19 [76]	NNNPDF2.0 [78]
DIS in ℓ^-+A	✓	✓	✓	✓	✓	✓	✓
Drell-Yan in p+A	✓	✓	✓	✓			
RHIC pions d+Au	✓	✓	✓	✓			
ν-nucleus DIS			✓		✓	✓	✓
Drell-Yan in π+A			✓				
LHC p+Pb dijets			✓				
LHC p+Pb W, Z			✓	✓			✓
Order in α_s	NLO	NLO	NLO	NLO	NNLO	NNLO	NLO
datapoints	929	708	1811	828	4525	2336	1467
free parameters	15	16	20	19	9	16	256
proton baseline	CT14NLO	CTEQ6M-like	CT14NLO	CTEQ6M-like	CT18	own fit	NNPDF3.1
flavour separation		valence	valence + sea (V + S)	V + S	V + S	V + S	V + S

Table 1.1: Comparison of various nuclear PDF sets. Table adapted from Refs. [79] and [80]. The three vertical lines separate the nPDFs that were compared with the data in this thesis (left) from those that were not (right).

1.3.1.4 Cold energy loss

A cold nuclear medium induces an energy loss on outgoing particles through gluon radiation. Hard processes in p–A collisions are sensitive to two different regimes of gluon radiation timescales [85]. There is the Landau-Pomeranchuk-Migdal (LPM) regime, which corresponds to gluon formation timescales of the order of the length of the nuclear medium $t_f \lesssim L$, and the factorisation regime which corresponds to $t_f \gg L$. The latter gluon radiation is also named fully coherent radiation. The LPM regime is associated with initial and final state energy loss, and its contributions are expected to vanish in high-energy collisions. On the other hand, fully coherent radiation is associated with interference of gluons from incoming particles, produced long before entering the medium, and outgoing particles. The fully coherent radiation could play a key role in the suppression of colored hard probes in p–A collisions. For example, J/ψ suppression in h–A collisions can be described by fully coherent radiation [85]. In contrast, Drell-Yan production in p–A collisions occurs through a colorless hard probe, so that it is not sensitive to fully coherent radiation. Drell-Yan production in p–A collisions could therefore be sensitive to the LPM regime.

1.3.2 Hot Nuclear Matter effects

1.3.2.1 Effects on Z bosons

The production time of the Z boson is inversely proportional to its mass $\sim 1/M_Z \sim 10^{-3}$ fm/c and has a decay time of 0.08 fm/c, while the QGP forms after 1 fm/c. This means that Z bosons are produced and decay before the QGP is formed so that they cannot interact with it. Their leptonic decays carry no color charge and therefore do not interact strongly with the QGP. On the other hand, the charged leptons can interact electromagnetically with the QGP. Calculations show that lepton energy loss is of the order of tens of MeV [86]. Additionally, an ATLAS measurement has shown an observed momentum broadening of $\mu^+\mu^-$ pairs from photon decays [87]. The scale of the broadening was found to be $k_t = 70 \pm 10$ MeV. However, it has been shown that this broadening could also be explained by more detailed modeling of the incoming photon fluxes, removing the need to invoke EM rescatterings [88, 89]. Regardless of the origin of the momentum broadening, it should be noted that typical momentum scales of the leptonic decays of the Z bosons are around 40 GeV/c (half its mass), so that any such broadening can experimentally be ignored in any case.

The lack of sensitivity to final state strong and EM effects means that Z bosons in leptonic decay channels can be used to study initial state effects. This makes them ideal tools for nPDF measurements, both in p–A and A–A collisions.

1.3.2.2 Effects on J/ψ

Although not the main topic of this thesis, the study of J/ψ production in heavy ion collisions is interesting in its own right as it allows to indirectly probe the temperature of the QGP. This is done by a number of effects that will be discussed now.

Debye Screening

The static cornell potential, as given by Eq. 1.4 applies to heavy quark pairs in vacuum. In a hot and dense QCD medium, the potential is modified in two ways. First, the hot medium reduces the string tension σ to 0. Secondly, the high density of colored charges creates a screen between the two heavy quarks. This is known as Debye screening. This is reflected in the potential by the Coulomb-like $\frac{-\kappa}{r}$ term becoming a Yukawa-like term $\frac{-\kappa}{r}e^{-r/r_D}$, where r_D is the Debye screening length, which is inversely proportional to the QGP temperature T [84]. When the radial distance of the quark pair exceeds the screening length, the pair dissociates, which suppresses quarkonia production. Different quarkonia have different binding energies and therefore dissociation lengths. Measurements of a variety of quarkonia can consequently act as a QGP thermometer. In more advanced analyses, the heavy quark potential gains imaginary terms as well [84].

Collisional dissociation

The Debye screening explained above applies to quarkonium dissociation in a static medium. Dynamic dissociation can also occur, from interactions between a heavy quark pair and partons in the QGP. There are two main processes through which this dynamic dissociation takes place [84]. The first is gluon dissociation where a thermal gluon from the QGP is absorbed by the heavy quark pair. If the gluon is energetic enough, the binding energy can be overcome, dissociating the bound state. Alternatively, inelastic parton scattering can also dissociate heavy quark pairs. However, not only partons can induce quarkonium suppression. Inelastic collisions with secondary particles such as π or ρ mesons (called comovers) in a hot and dense medium can also dissociate quarkonia [84].

Regeneration

When comparing the suppression of J/ψ production in Pb–Pb collisions at $\sqrt{s_{\mathrm{NN}}} = 20\,\mathrm{GeV}$ at the SPS, in Au–Au collisions at $\sqrt{s_{\mathrm{NN}}} = 200\,\mathrm{GeV}$ at RHIC and in Pb–Pb collisions at $\sqrt{s_{\mathrm{NN}}} = 2.76\,\mathrm{TeV}$ and $\sqrt{s_{\mathrm{NN}}} = 5.02\,\mathrm{TeV}$ at LHC, a puzzle appears. The suppression is similar between SPS and RHIC, even though the collision energy is roughly 10 times larger in the latter. The larger collision energy should lead to a higher temperature QGP, and therefore a larger suppression. More puzzling is the fact that at the LHC, the observed suppression is smaller than at SPS and RHIC [84, 90]. To make sense of this behavior, the regeneration mechanism was proposed. Charm quark production is expected to be small at SPS, while more than 10 $c\bar{c}$ quark pairs are expected to be produced in central Au–Au collisions at RHIC, and more than 100 in central Pb–Pb collisions at the LHC. Charm quarks from one pair can then form quarkonia with anticharm quarks from another pair, which enhances charmonium production.

In the end, a complex interplay of J/ψ production enhancement and suppression at different p_{T} regimes can help

to understand the temperatures reached in the QGP.

1.4 Existing measurements

1.4.1 EW bosons

Numerous measurements of electroweak bosons have been done at the LHC. The analysis of Z bosons is generally easier to do due to the decay into a high-p_{T} lepton pair with opposite charge, which is easy to detect. On the other hand, W-boson measurements are experimentally more involved because they entail the measurement of a single high-p_{T} charged lepton. Then, either the accompanying (anti)neutrino has to be measured through the reconstruction of missing energy or the p_{T} distribution of the charged lepton is fitted with models obtained from simulations. The main benefit of W bosons is their production cross section, which is larger than that of Z bosons. ATLAS measurements at mid-rapidity indicate that the W^{+}-boson cross section multiplied by the single-lepton branching ratio is roughly 6 times larger than that of Z bosons multiplied by the leptonic branching ratio. For the W^{-}, the production is roughly 4 times larger [31, 91]. The larger cross sections lead to measurements with higher experimental precision than Z-boson measurements, which in turn lead to better constraining power for nPDFs. In this subsection, a non-exhaustive selection of measurements is shown. First, measurements in ALICE are discussed and after that, measurements at LHCb, ATLAS and CMS are presented.

Measurements in ALICE

The separate measurements done in ALICE will be presented based on the boson and collision system. Measurements of Z bosons and W bosons in p–Pb collisions are discussed first, followed by a Z-boson measurement done in Pb–Pb.

Measurements on Z bosons have been done in p–Pb collisions at $\sqrt{s_{\mathrm{NN}}} = 5.02\,\mathrm{TeV}$ and $\sqrt{s_{\mathrm{NN}}} = 8.16\,\mathrm{TeV}$, at forward rapidity and backward rapidity [92, 93]. The integrated luminosity in the $\sqrt{s_{\mathrm{NN}}} = 5.02\,\mathrm{TeV}$ dataset is $5.03 \pm 0.18\mathrm{nb}^{-1}$ at forward rapidity, and $5.81 \pm 0.20\mathrm{nb}^{-1}$ at backward rapidity, while it is $8.40 \pm 0.16\mathrm{nb}^{-1}$ and $12.74 \pm 0.24\mathrm{nb}^{-1}$ at $\sqrt{s_{\mathrm{NN}}} = 8.16\,\mathrm{TeV}$. The measured cross sections were compared with models that include nuclear modifications to PDFs and those without (although they do include isospin). All model predictions are close to each other and agree with the data, as seen in Fig.1.13. The similarity of the predictions is attributed to the fact that only one nucleon is sampled from a nuclear PDF. Furthermore, at backward rapidity, multiple nPDF effects occur that enhance and deplete free-nucleon PDFs so that in the end they tend to cancel each other. On the other hand, at forward rapidity, mainly shadowing is probed so that the nPDF predictions are lower than free-nucleon predictions. Within experimental uncertainty, both models with and without nuclear modifications successfully described the data. No strong conclusions can therefore be drawn regarding the presence of nuclear modifications of PDFs.

W bosons have also been measured in the same datasets mentioned above, and are shown in Fig. 1.14. For

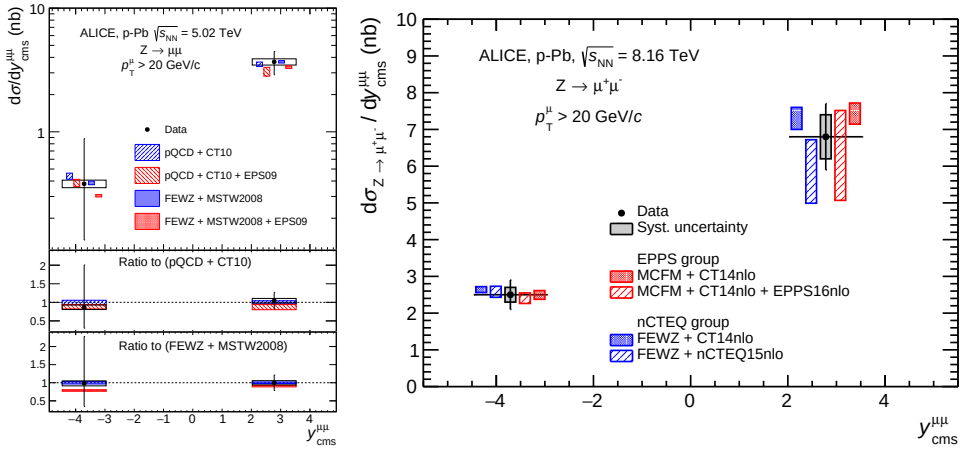

Figure 1.13: Z-boson cross section in p–Pb collisions measured in ALICE, as a function of rapidity at $\sqrt{s_{\rm NN}} = 5.02\,\text{TeV}$ (left) and $\sqrt{s_{\rm NN}} = 8.16\,\text{TeV}$. Figures taken from [92, 93].

the W analysis at $\sqrt{s_{\rm NN}} = 8.16\,\text{TeV}$, stricter event selections were applied than for the Z analysis, so that the integrated luminosity is $6.81 \pm 0.15\text{nb}^{-1}$ at forward rapidity and $10.2 \pm 0.27\text{nb}^{-1}$ at backward rapidity. Comparing with theoretical predictions, both W measurements show a preference for models that include nPDFs, mainly at forward rapidity. This preference is stronger in the $\sqrt{s_{\rm NN}} = 8.16\,\text{TeV}$ dataset where experimental uncertainties are smaller, compared to the $\sqrt{s_{\rm NN}} = 5.02\,\text{TeV}$ dataset. For the W^+ boson, a $2.7\ \sigma$ deviation was observed between the data and the free-nucleon predictions in the $2.03 < y < 3.53$ rapidity interval. The experimental uncertainty on the W^+ boson at forward rapidity is even smaller than the theoretical uncertainty on one of the nPDF models, which allows to constrain the model.

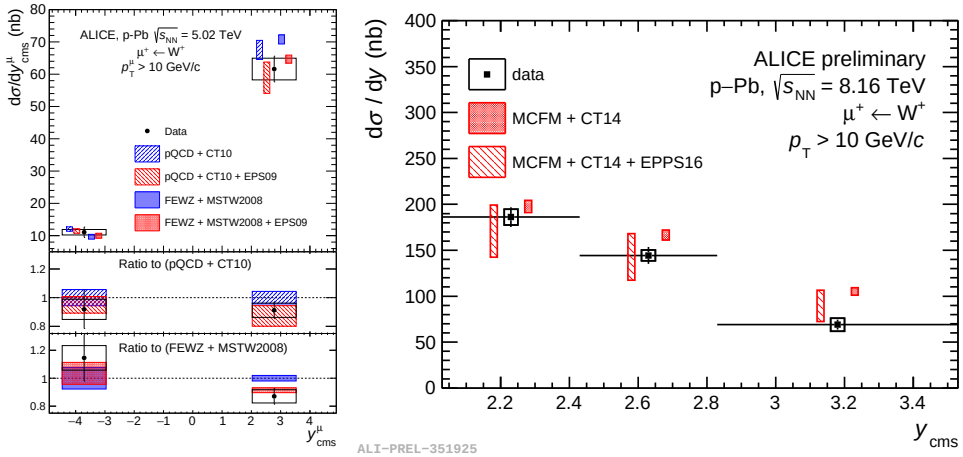

Figure 1.14: W^+-boson cross section in p–Pb collisions measured in ALICE, as a function of rapidity at $\sqrt{s_{\rm NN}} = 5.02\,\text{TeV}$ (left) and $\sqrt{s_{\rm NN}} = 8.16\,\text{TeV}$ (right). Figures taken from [92] and [94]

Lastly, Z bosons have been measured in Pb–Pb collisions at $\sqrt{s_{\rm NN}} = 5.02\,\text{TeV}$, using data collected in 2015. The measurement shows a clear preference for nPDF models, exhibiting a $2.3\ \sigma$ deviation from free-nucleon predictions in the integrated yields. However, because experimental uncertainties are of similar size as theoretical predictions

in the differential invariant yield shown in Fig. 1.15, the data have limited constraining power. In 2018, more data were collected from Pb–Pb collisions at $\sqrt{s_{\mathrm{NN}}} = 5.02\,\mathrm{TeV}$. The main analysis in this thesis pertains to Z-boson production, using the Pb–Pb dataset from 2015 and 2018.

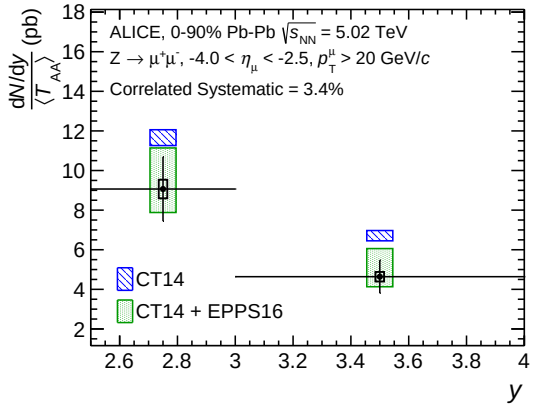

Figure 1.15: Z boson invariant yield as a function of rapidity in Pb–Pb collisions at $\sqrt{s_{\mathrm{NN}}} = 5.02\,\mathrm{TeV}$. Figure taken from [95].

In summary, with the exception of Z-boson measurements in p–Pb collisions which are compatible with both free-nucleon and nPDF models, ALICE measurements show a preference for nPDF models. This is more pronounced at forward rapidity, where the shadowing effect (which leads to a depletion in nPDFs) is probed. In particular, W^+ boson measurements at forward rapidity in p–Pb collisions at $\sqrt{s_{\mathrm{NN}}} = 8.16\,\mathrm{TeV}$ have smaller experimental uncertainties than theoretical uncertainties and therefore have the potential to constrain nPDFs. Z-boson measurements in Pb–Pb collisions are well described by nPDFs, but offer no constraining power.

Other measurements at the LHC

Z bosons in p–Pb collisions at $\sqrt{s_{\mathrm{NN}}} = 5.02\,\mathrm{TeV}$ have also been measured by LHCb, with an integrated luminosity of $1.099 \pm 0.021\mathrm{nb}^{-1}$ at forward rapidity and $0.521 \pm 0.011\mathrm{nb}^{-1}$ at backward rapidity [96]. The measured cross section is shown in Fig. 1.16 (left). The conclusions are similar to those drawn in the ALICE measurements: no definitive statements about preferences for models including or excluding nuclear modifications can be made.

A measurement of W bosons at midrapidity in p–Pb collisions at $\sqrt{s_{\mathrm{NN}}} = 8.16\,\mathrm{TeV}$ was done at CMS [97]. The forward and backward yields were combined to obtain the forward-backward ratio $N_\mu(+\eta^\mu_{\mathrm{CM}})/N_\mu(-\eta^\mu_{\mathrm{CM}})$ shown in Fig. 1.16 (right). As can be seen in the figure, experimental uncertainties are much smaller than theoretical uncertainties and the deviations from free-nucleon predictions are large. This provides strong constraining power for nPDF models.

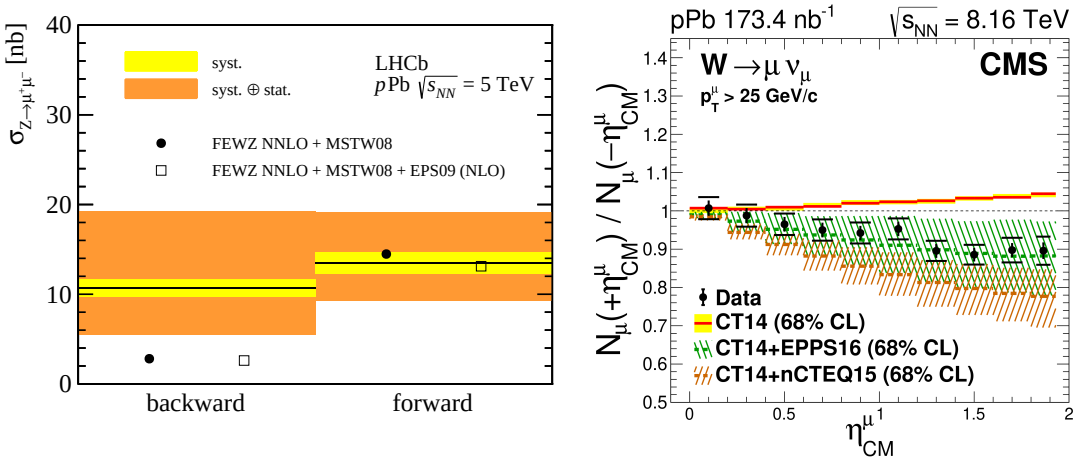

Figure 1.16: Z boson cross section measured at forward rapidity at $\sqrt{s} = 5.02\,\mathrm{TeV}$ by LHCb (left) and W boson forward-backward ratio measured at midrapidity at $\sqrt{s_{\mathrm{NN}}} = 8.16\,\mathrm{TeV}$ by CMS (right). Figures taken from [96, 97].

1.4.2 Di-J/ψ and associated production

J/ψ pair production has been studied in a number of experiments (See Refs [98, 99] and references therein). DPS contributions are sizeable but strong conclusions are difficult to draw due to large theoretical uncertainties. In many cases, the CSM LO + NLO contributions already exceed the measured di-J/ψ cross sections, such that the need for large DPS contributions is reduced [52]. Nonetheless, in certain kinematic regimes such as large Δy, J/ψ pair production is expected to be dominated by DPS. Two such examples are shown in Figure 1.17.

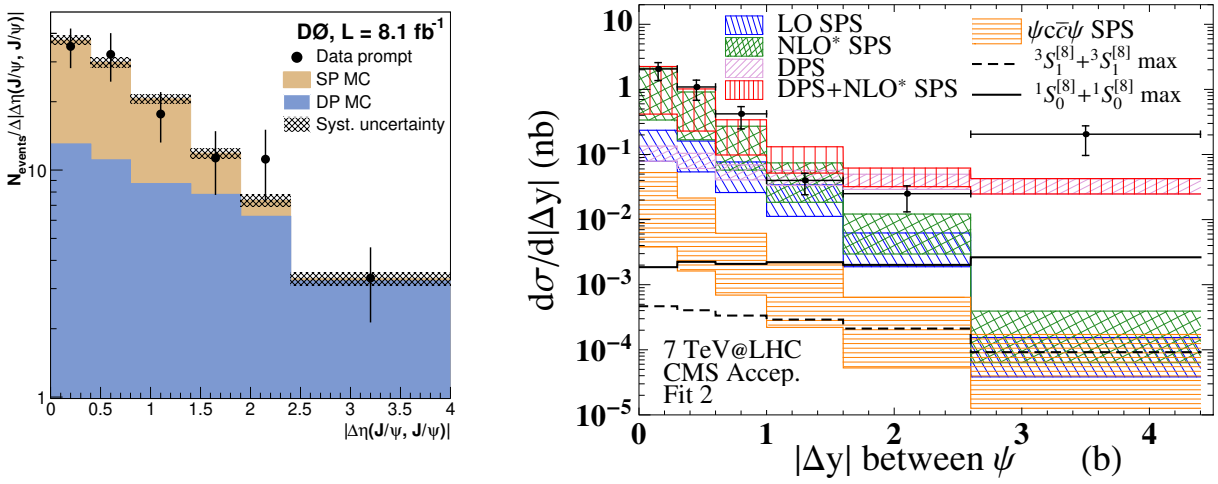

Figure 1.17: Expected contribution of SPS and DPS to di-J/ψ production as a function of rapidity difference between the two J/ψ. The left plot is taken from [43], while the right plot is taken from [52].

In the simplest DPS framework, σ_{eff} is expected to be independent of processes and energy. However, various extractions yield different values of the effective cross section. It was suggested in [43] that this could originate from a flavor dependence. This was evidenced by the fact that extractions from processes that were dominated by gluon

distributions (such as di-quarkonium, or 4-jet production) were different from those from processes dominated by quark distributions (such as W + jet and γ + jet). However, in [100] it was shown that there is already a disagreement between various measurements that are dominated by gluon distributions. Figure 1.18 shows the determination of σ_{eff} from various measurements, indicating that its universality might not hold.

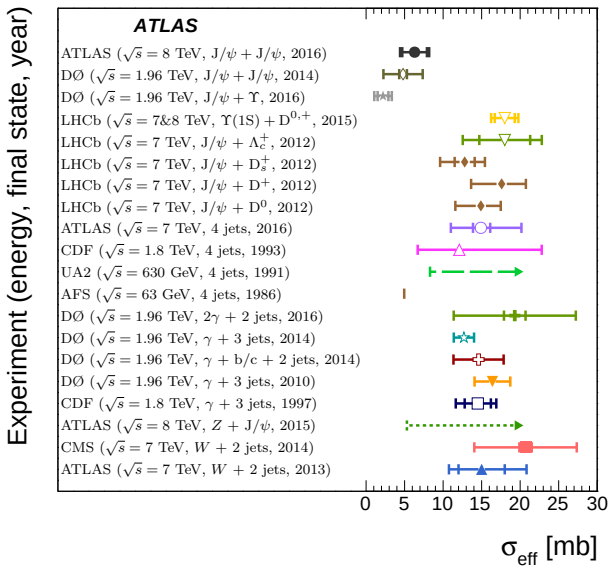

Figure 1.18: Determination of the effective cross section σ_{eff}, used in the DPS framework from various measurements. Figure taken from [100].

The LHCb has measured J/ψ pair production as well as other variations of double charm production in pp collisions at $\sqrt{s} = 7\,\mathrm{TeV}$ [101, 102], and has also measured J/ψ pair production in pp collisions at $\sqrt{s} = 13\,\mathrm{TeV}$ [103]. The left plot of Figure 1.19 shows the production cross section of a multitude of double charm hadrons, showcasing the experimental feasibility of measurements beside di-quarkonia. The differential di-J/ψ cross section in pp collisions at $\sqrt{s} = 13\,\mathrm{TeV}$ as a function of Δy is shown on the right plot of Figure 1.19. Again, theoretical predictions indicate that at large Δy, DPS contributions dominate.

Although it is generally accepted that DPS contributions cannot be neglected in di-J/ψ measurements, their relative size as well as the effect of parton correlations (which can result in process-dependence of σ_{eff} are not yet fully understood. More (differential) measurements are therefore important to establish the nature of DPS contributions in quarkonium pair production.

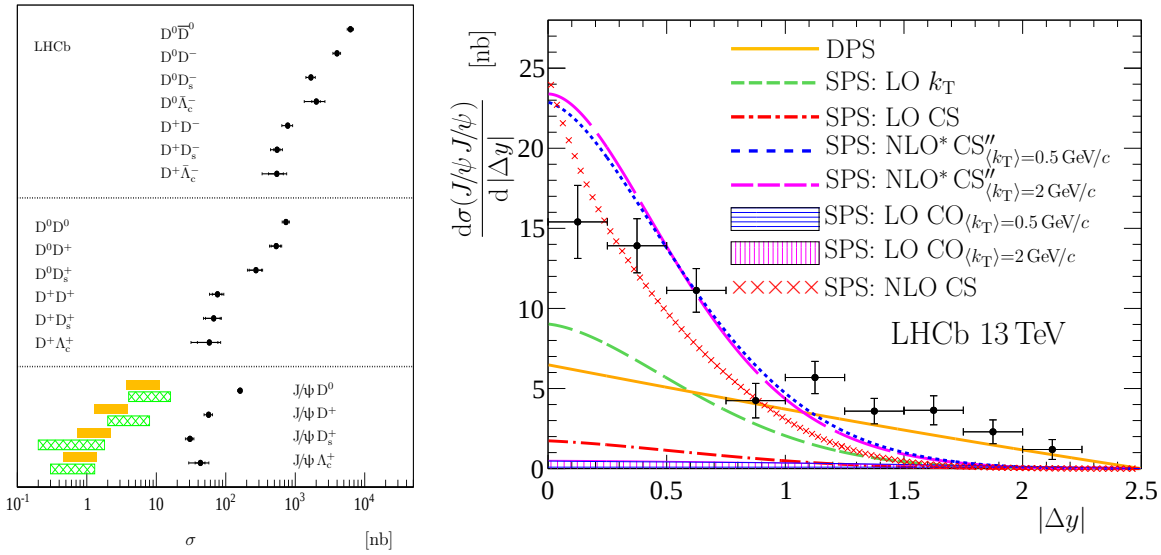

Figure 1.19: Production cross section for several combinations of charm hadrons in pp collisions at $\sqrt{s} = 7\,\mathrm{TeV}$ (left) and production cross section as a function of rapidity difference Δy in pp collisions at $\sqrt{s} = 13\,\mathrm{TeV}$ (right). Figures taken from [102] and [103].

Chapter 2

ALICE detector

2.1 LHC

The Large Hadron Collider (LHC) is a particle collider located at the Franco-Swiss border operated by the European Organization for Nuclear Research (CERN)[1]. The physics goals of the LHC stretch over a wide range of fundamental topics. They include open questions relating to the origin of particle mass (for which the discovery of the Higgs-boson is an important milestone [104, 105]), the existence of dark matter, the existence of supersymmetrical particles, the matter-antimatter asymmetry and the properties of the quark-gluon plasma (QGP). The LHC is a circular collider, with a circumference of 27 km. It is currently the world's largest and most powerful accelerator. Protons can be accelerated up to an energy of $\sqrt{s} = 7\,\mathrm{TeV}$, corresponding to a center-of-mass energy of $\sqrt{s} = 14$ TeV in proton–proton collisions. The LHC was also designed to accelerate and collide Pb-nuclei. Collisions between the latter can reach center-of-mass energies per nucleon pair of up to $\sqrt{s_{\mathrm{NN}}} = 5.52\,\mathrm{TeV}$ [106]. Additionally, asymmetric p–Pb beams and Xe–Xe beams have also been collided, even though they were not originally included in the LHC design [107, 108].

The LHC houses several experiments at the various Interaction Points (IP) where the beams collide. There are the ATLAS and CMS experiments, both of which use a general purpose detector to cover a wide range of physics. In addition there is the ALICE experiment which specializes in QGP/heavy-ion physics as well as the LHCb experiment which focuses on CP violation. Furthermore, three smaller experiments can be found close to some of the mentioned main detectors. The TOTEM experiment, close to the CMS IP, is dedicated to the measurement of the proton-proton total cross section, elastic scattering and diffraction dissociation in the forward direction. These measurements will help in better understanding the structure of protons. Then, near the ATLAS IP is the LHCf experiment, with the main aim of precisely measuring the production spectra of neutral particles in the forward direction. This will allow to simulate and test cosmic ray shower models which are used by ground-based cosmic ray experiments. Lastly, in

[1] The abbreviation is derived from the originally French name, *Conseil Européen pour la Recherche Nucléaire*

the neighborhood of the LHCb detector is the MOEDAL detector whose purpose is to directly search for magnetic monopoles as well as exotic BSM particles.

The hadrons that will eventually collide are not directly injected into the LHC for acceleration. Instead, they first go through a series of smaller accelerators, gradually increasing their energy before being injected into the LHC, where the final acceleration takes place. Furthermore, atoms such as Pb and Xe need to be stripped of their electrons so that only the nuclei remain. This happens concurrently with the acceleration and is also done in phases. The accelerator scheme is shown in Fig. 2.1.

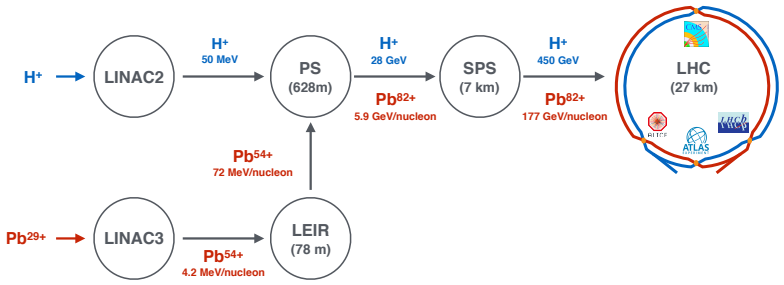

Figure 2.1: Accelerator scheme for the LHC. Hadrons are injected and accelerated in phases before being injected into the LHC. Figure taken from [109].

The LHC is comprised of two concentric rings in which counter-rotating beams are injected and accelerated. A complex system of magnets and electric fields is necessary for its operation. In total, there are almost 10000 magnets, of over 50 different types [110]. 1232 superconducting dipole magnets bend the beams, while 392 quadrupole magnets focus the beams. The focusing is necessary to prevent the beams from diverging due to electromagnetic interactions between the particles themselves. In addition to these so-called main dipole and main quadrupole magnets, other magnets are used as well. These include higher order monopoles such as sextupole, octupole and decapole magnets which correct for imperfections in the fields of the main dipoles and quadrupoles. Also, at each experiment, two sets of triplets of quadrupoles are put in place (one set on each side). Their function is to squeeze the beams before they collide, narrowing the beam diameter to 16 micrometers [111]. This allows for a higher instantaneous luminosity.

The charged particles are accelerated in radiofrequency (RF) cavities. These contain oscillating electric fields at a frequency such that during the accelerating phase the charged particles always feel an accelerating force. The RF cavities contain an electric field that oscillates with a frequency of 400 MHz, while the revolution frequency of the LHC is 11.245 kHz. In order to ensure that a particle always feels an accelerating force when passing through the RF cavity, the RF frequency must be a multiple of the revolution frequency. Particles that travel synchronized with the RF frequency will feel the same force every time. This is referred to as a synchronous particle [112]. Particles that deviate slightly from synchronization will tend to oscillate around the synchronous particles. This results in the formation of groups of particles, which are referred to as bunches. The harmonic number h, defined by $f_{\mathrm{RF}} = h f_{\mathrm{rev}}$,

for the LHC is 35640. It represents the number of buckets in which a bunch can potentially be filled. However, buckets are just virtual points on the ring, so they can be either filled with a bunch or be empty. In fact, the minimum bunch spacing at the LHC is 25 ns $(40$ Mhz). Therefore, practically speaking there can be at most 3564 buckets filled [113]. During the Pb–Pb data taking runs there were 518 (in 2015) and 733 (in 2018) bunches, each containing around $2 \cdot 10^8$ Pb-ions per bunch [114].

During operation, the bunches are not injected equidistantly, but following a certain filling scheme. The reason for this is to create ideal collision settings for each of the four main experiments [113]. At IP1 and IP5, the ATLAS and CMS experiment are located, which are high luminosity experiments. Therefore the goal is to deliver the *maximum* luminosity at IP1 and IP5. However, the specialized experiments at IP2 (ALICE) and IP8 (LHCb), require an *optimum* luminosity, with respect to how fast the detectors can process events. An example of a filling scheme is 25ns_1740b_1728_1570_1636_96bpi_21inj. Here, the 25 ns refers to the bunch spacing. Values of 50 ns, 75 ns, 100 ns, or 525 ns for example are also possible. The second term refers to the total number of bunches present, which is 1740 in this case. The following three numbers are the expected number of colliding bunch pairs at IP1/5, IP2 and IP8 respectively. After that, a suffix can be added to encode information about a specific scheme. In this case, the last two terms indicate that there were 96 bunches per injection for 21 injections [115].

2.2 ALICE Detector

In this section, the ALICE detector is outlined. The information mainly comes from Refs. [116–120], and an interested reader is invited to read these and references therein for additional or more detailed information.

ALICE is a dedicated heavy-ion detector with a focus on QCD, which is the strong sector of the Standard Model. The apparatus, with dimensions $16 \times 16 \times 26$ m^3 and weight of approximately 10000 t is shown in Fig. 2.2. It is able to detect a wide variety of particles such as hadrons, electrons, muons and photons. It was specifically designed to comprehensively study nuclear collisions in both hard scatterings at high energy scales and collective phenomena at low energy scales. To this end, its design was specialized to have high granularity to cope with the large flux of charged particles (up to 8000 per unit of rapidity at mid-rapidity[2]) as well as having tracking down to low momenta, starting at ~ 80 MeV/c [117]. Particle identification can also be provided for tracks with transverse momenta up to 20 GeV/c.

The ALICE detector (Fig. 2.2) consists of many subdetectors which can be divided into three categories. First is the central barrel, containing the Inner Tracking System (ITS), Time-Projection Chamber (TPC), Time-Of-Flight (TOF) detector, Transition Radiation Detector (TRD), High-Momentum Particle Identification Detector (HMPID), Photon Spectrometer (PHOS) and Electromagnetic Calorimeter (EMCAL). The entire central barrel is embedded in a

[2]Original estimates of charged particle multiplicity at LHC energies spanned a range of 2000 up to 8000. The detector was therefore designed for a charged particle density at mid-rapidity of 4000 and tested in simulations at values twice as high [116] . However, in practice a maximum density of about 2000 charged particles at mid-rapidity is reached in the most central Pb–Pb collisions [121].

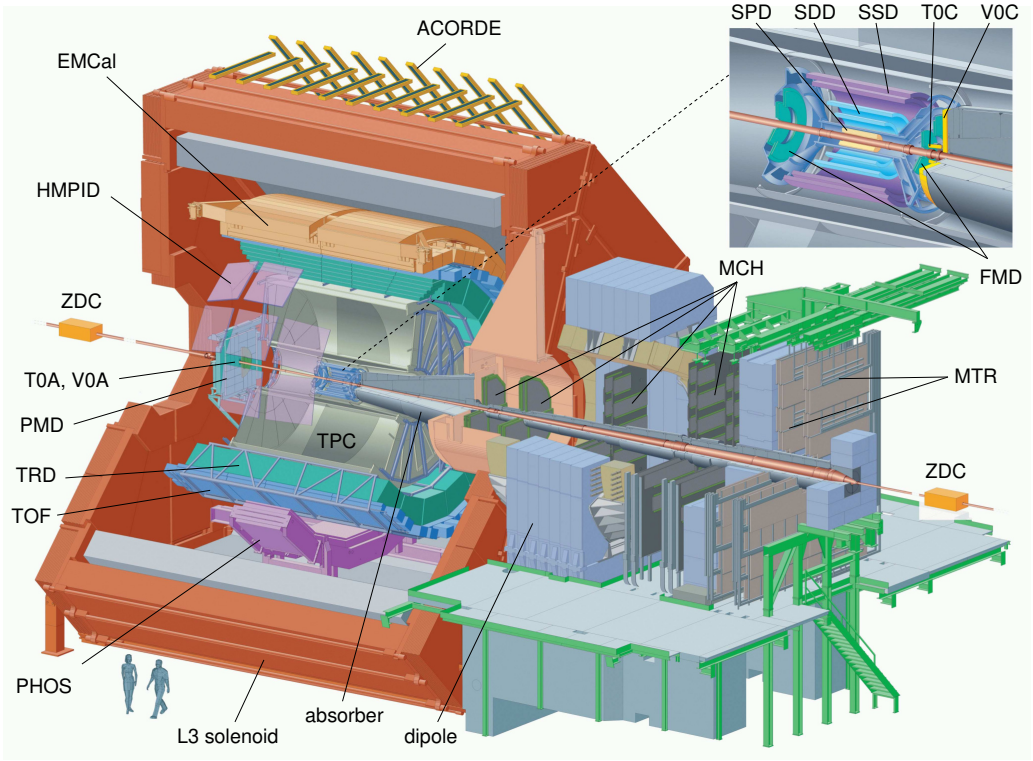

Figure 2.2: Schematic view of the ALICE apparatus. The central barrel measures particle tracks at midrapidity, the forward detectors (PMD, FMD, V0, T0 and ZDC) are used for global event characterization and triggering. The muon spectrometer reconstructs muon tracks at forward rapidity. Figure taken from Ref. [117].

solenoid (also known as the L3 magnet[3]) with a maximum field strength of $B = 0.5$ T. The main use of the central barrel is to measure and identify charged hadrons, photons and electrons. More specifically, the ITS, TPC and TRD reconstruct charged particle tracks. At low p_{T}, the ITS, TPC and TOF are used for particle identification, while at high p_{T} the HMPID and TRD are also available. The EMCAL and PHOS are used for the measurement of photons and electrons. For electrons, identification and measurement are also done with the ITS and TPC.

Secondly there are the global detectors. These are the Zero Degree Calorimeter (ZDC), Photon Multiplicity Detector (PMD), Forward Multiplicity Detector (FMD), V0 detector and T0 detector. Although some of these detectors are physically located in the central barrel, they serve a different purpose than to reconstruct particle tracks. Instead, they are used for triggering, background rejection and global event characterization such as centrality. Moreover, the T0 provides timing information necessary for the particle identification of the TOF. Lastly, located on top of the central barrel is the ALICE Cosmic Ray Detector (ACORDE), for the detection of atmospheric muon events. The ACORDE also is used for the alignment and calibration of some of the central barrel detectors.

Lastly, there is the Muon Spectrometer at forward rapidity. As the name implies, its main function is to detect muons. As it is the main detector used in this thesis, it will be outlined in more detail in subsection 2.2.3.

Coordinate system

[3]L3 was one of four detectors in the Large Electron-Positron collider (LEP), which was the predecessor to the LHC. The magnet from the dismantled L3 experiment was taken over by ALICE.

The ALICE Coordinate System is defined as follows [122]: with the nominal interaction point of the collisions at the origin, a Cartesian coordinate system is defined. The z-axis is parallel to the beam axis and the convention is such that the Muon Spectrometer lies at negative z. The x-axis is perpendicular to the beam (and therefore z-axis), pointing towards the center of the LHC where x-values are positive. Lastly, the y-axis is perpendicular to both the x-axis and z-axis, pointing upwards for positive values. In spherical coordinates, φ denotes the azimuthal angle, from 0 to 2π. The convention is such that it is 0 when it coincides with the positive x-axis, increasing to $\pi/2$ when it coincides with the positive y-axis. The polar angle θ ranges from 0 when it coincides with the positive z-axis, to $\pi/2$ for the positive y-axis, to π for the negative z-axis.

The main detector in the analyses described in this thesis is the muon spectrometer, but the V0 and SPD detectors were used for the event selection. A brief description will be now given of both detectors, followed by the description of the spectrometer.

2.2.1 V0 Detector

The V0 consists of two subdetectors, the V0A and V0C, which are located on opposite sides of the nominal interaction point (see Fig. 2.2). The V0C is fixed to the front absorber of the Muon Spectrometer, at $z = -88$ cm, covering a pseudorapidity range of $-3.7 < \eta < -1.7$. On the other side of the interaction point at $z = 329$ cm is the V0A, covering $2.8 < \eta < 5.1$. Both detectors are segmented in 4 rings in the radial direction, around the beam pipe. Furthermore, each ring is further segmented into 8 sections in the azimuthal direction, covering the full azimuth, as seen in Fig. 2.3. They are equipped with scintillator counters, and their working principle is as follows: when charged particles pass through the scintillators, they lose energy by exciting the scintillator molecules. These molecules then de-excite by emitting photons, which are subsequently guided in optical fibers before being collected in Photo Multiplier Tubes. In these tubes, the photons are converted into an electric signal that is read out.

The V0 has several important functions in the ALICE detector:

- It provides the minimum bias triggers, by requiring a signal in both the V0A as well as the V0C[4].
- The V0 also provides a rejection of beam-induced background events. This rejection is explained in detail in 3.1.1.1.
- Based on the energy deposited in the V0, the charged particle multiplicity in the forward direction can be estimated. As this quantity is related to the event geometry, the V0 can consequently be used as a centrality estimator.
- The V0 also provides a measurement of luminosity which is an essential element for cross section measurements.

[4] During early operation, other MB triggers were used for analyses. One such trigger is defined by a signal in either the V0A OR V0C. Another obsolete trigger is the requirement of a signal in the V0A, V0C or SPD.

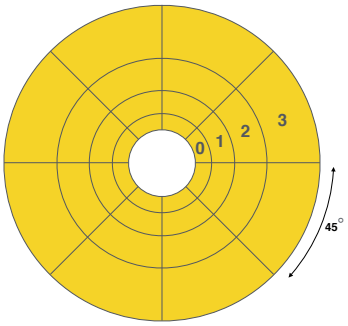

Figure 2.3: Schematic transverse view of the V0A/V0C detectors. They are segmented in 4 rings, each of which is divided into 8 sections. Figure taken from [109].

2.2.2 Silicon Pixel Detector

The Inner Tracking System is a set of concentric cylindrical detectors surrounding the beam pipe around the IP, as shown in the upper right corner of Fig. 2.2. It has several tasks related to the operation of the central barrel, one of which relates to the muon spectrometer: the ITS is used for the determination of the primary collision vertex, with a resolution of better than 100 μm [116]. To do this, the innermost two layers of the ITS, called the Silicon Pixel Detector (SPD), are used. The SPD consists of two cylinders of radius 3.9 and 7.6 cm, both 14.1 cm long. A total of 9.84 million detection cells can be found on the SPD. This high number of cells is necessary, because at such short distances to the IP, track densities can reach values of up to 50 tracks/ cm^2. The high granularity, coupled with the small distance to the IP allows for the determination of the primary interaction vertex, to which tracks from the spectrometer are extrapolated.

2.2.3 Muon Spectrometer

The Muon Spectrometer is the ALICE subsystem that is fully dedicated to muon detection. The muons can originate from decays of light (ω and ϕ) or heavy (J/ψ and Υ families) vector mesons, open heavy flavors (such as D-mesons) or the electroweak vector bosons W$^{\pm}$ and Z. The spectrometer covers the pseudorapidity region $-4 < \eta < -2.5$ and is equipped with a high-granularity tracking system in order to cope with the large expected particle multiplicities in Pb–Pb collisions. One of the important features of the detector is its quarkonium p_{T} coverage, which goes down to $p_{\mathrm{T}_{\mathrm{quarkonium}}} = 0$ GeV/c. This is important because some medium effects, such as heavy quark potential screening or charm recombination, manifest more clearly at low p_{T} [123].

The spectrometer was designed to have a mass resolution of 100 MeV/c^2 at the mass of the Υ ($\sim$10 GeV/c^2). This is necessary to be able to distinguish the Υ, Υ' and Υ'' resonances. It is this last requirement that determined the bending strength of the spectrometer magnet as well as the spatial resolution of the tracking system. In practice, this specification is reached at the J/ψ mass peak, with a resolution of $\sim$73 MeV/c^2 in central Pb–Pb collisions.

However, at the Υ mass peak the resolution is 147 ± 27 MeV/c^2 in minimum bias Pb–Pb collisions, exceeding the design specification [117].

A cross section of the spectrometer is shown in Fig. 2.4, in which the various components of the spectrometer can be seen. A description of these components is given in the following.

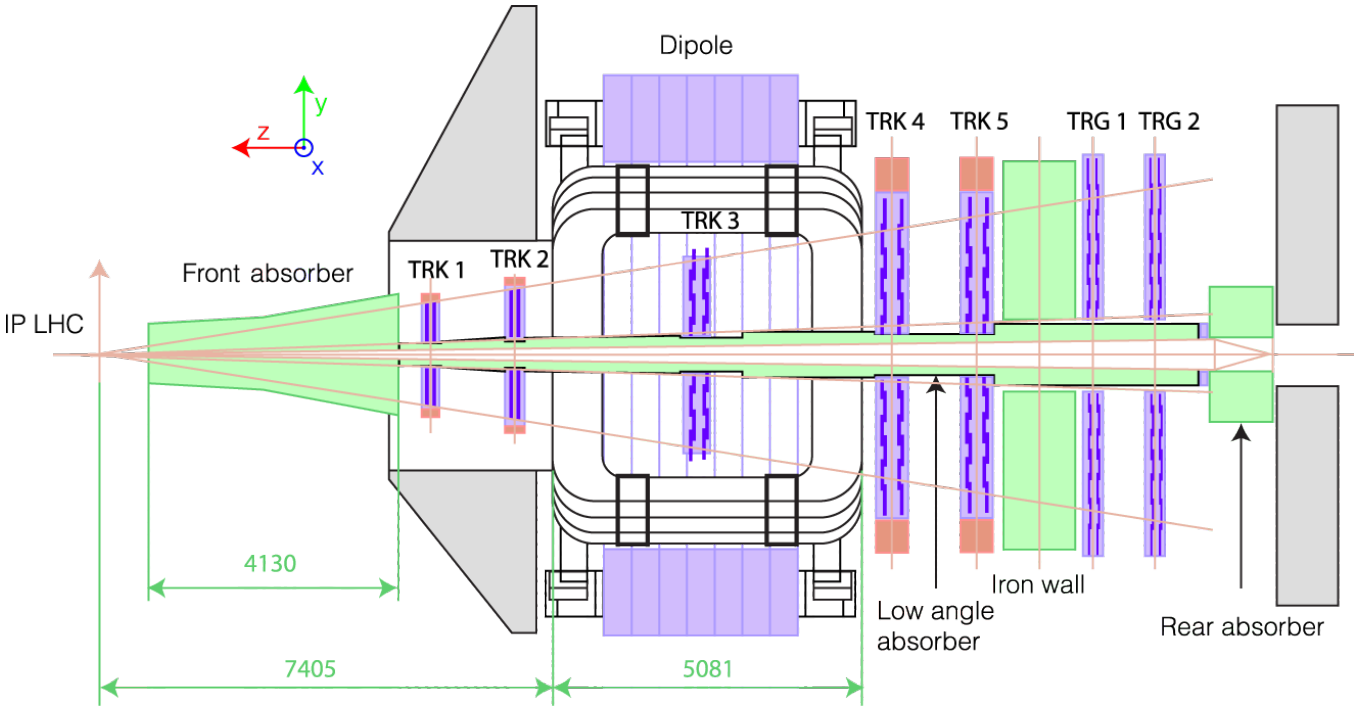

Figure 2.4: Cross section of the muon spectrometer. The different triggering and tracking stations are shown, as well as the absorbers and the dipole magnet. Figure taken from Ref. [124].

2.2.3.1 Absorbers

Several passive absorbers are placed at various locations in the spectrometer. The front absorber is located between the IP and the tracking chambers. It is a cone placed in the central barrel, mainly made of carbon, concrete and steel. The absorber is 4.13 m long, representing ~ 10 interaction lengths λ_{int} as well as ~ 60 radiation lengths X_0[5]. The passive front absorber has two main purposes: to attenuate the flux of charged hadrons by two orders of magnitude and to reduce background from muons that decay from pions and kaons [118]. By placing the absorber as close to the IP as possible (geometrical constraints do not allow closer than 90 cm, to minimally interfere with the functioning of the central barrel detectors), the pions and kaons can be absorbed before they decay. This reduces the rate at which their muonic decay products enter the spectrometer.

Along the length of the beam pipe, another absorber is placed, made of tungsten, lead and stainless steel. This absorber is called the beam shield. Its main function is like that of the front absorber, to protect the tracking and

[5]The hadronic interaction length is a measure for the attenuation power of a material. It represents the mean distance over which a flux reduces by a factor of $1/e$. The radiation length is the mean distance over which an electron's energy is reduced through radiation by a factor of $1/e$. The radiation length influences the effect of multiple scattering. For accurate track reconstruction, multiple scattering should be mimimised.

trigger chambers. It suppresses showers produced in the beam pipe, originating from primary particles. The design of the beam shield is such that it also suppresses showers which may arise due to interactions with the beam shield itself. The two aforementioned absorbers are however still not enough to protect the trigger chambers. For this reason, an iron wall is placed between the last tracking station and the trigger system. The iron wall is 1.2 m thick (with an area of 5.6×5.6 m^2), which corresponds to $\sim 7.2\ \lambda_{\mathrm{int}}$. Due to the additional number of hadronic interaction lengths, the iron wall essentially acts as a muon filter that only lets through muons with a total momentum of at least 4 GeV/c.

Lastly, there is a rear absorber behind the trigger stations to protect the spectrometer from particles coming from beam-gas collisions.

2.2.3.2 Tracking system

The tracking is done with 5 tracking stations. Each tracking station is equipped with two cathode pad chamber planes, which are placed both in front and in the back of the station. This results in a total of 10 detection planes. Every chamber plane provides a different (x, y, z) coordinate for the track reconstruction. The stations are numbered 1 through 5, with station 1 being closest to the IP. Station 1 is placed right after the front absorber to measure the exit point of the muons as accurately as possible. A dipole magnet (see subsection 2.2.3.3) is used to curve the muons which is necessary for the determination of their momentum. Stations 1 and 2 are located in front of the dipole, station 3 is inside of the dipole while stations 4 and 5 are located behind the dipole, as seen in Fig. 2.4.

In order to keep the occupancy below 5% (one of the design specifications), the readout of the chambers is highly segmented. The smallest pads used in the chambers are as small as 4.2×6.3 mm^2 in station 1. The farther away from the IP, the hit density decreases so the size of the readout pads increases to at most 5×100 mm^2 in station 3, 4 and 5.

The acceptance of the detector is such that it can detect muons in a cone with an opening angle between 2° and 9°. The active area of stations 1 and 2 are the geometrical projections of this cone [119], as shown by the diagonal lines in Fig. 2.4. A so-called quadrant structure is used for the tracking chambers of these stations, see Fig. 2.5-left. This means that the active area was divided into four sections of equal size, called quadrants. Stations 3, 4 and 5 need to cover larger surface area as they are further from the IP. However, creating large quadrants is mechanically very challenging. Therefore, these three stations use a so-called slat geometry, where horizontal elements (slats) are mosaically placed in two half-chambers, see Fig. 2.5-right. The semi-modular design allows for more reliable equipment, and reduces the overall cost and manpower requirements [119]. The design of the tracking system allows for a spatial resolution of $70\ \mu$m in the bending plane (vertically).

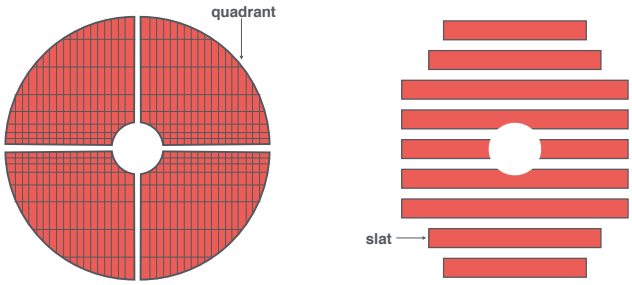

Figure 2.5: Transverse cross section of the tracking chambers. The left plot shows the quadrant structure of stations 1 and 2 while the right plot shows the slat structure of stations 3, 4 and five. Figures taken from Ref. [109].

2.2.3.3 Dipole magnet

The curvature of particles in a magnetic field allows one to measure their momenta and charge. In the spectrometer, a warm (i.e. not superconducting) dipole magnet is used, in which the third tracking station is placed. The dipole magnet, shown in Fig. 2.6, is 5 m long and weighs about 850 tons. It delivers a nominal field strength of 0.7 T and an integrated field strength of 3 Tm. The magnetic field is oriented along the x-axis, perpendicular to the beam and along the LHC radius. Therefore the dipole bends muons in the vertical y direction also perpendicular to the beam. Consequently, the xz-plane and yz-plane are known as the *non-bending plane* and the *bending plane*, respectively. The field polarity of the magnet can be inverted as well, with the magnetic flux either oriented along the positive x-axis or opposite to it.

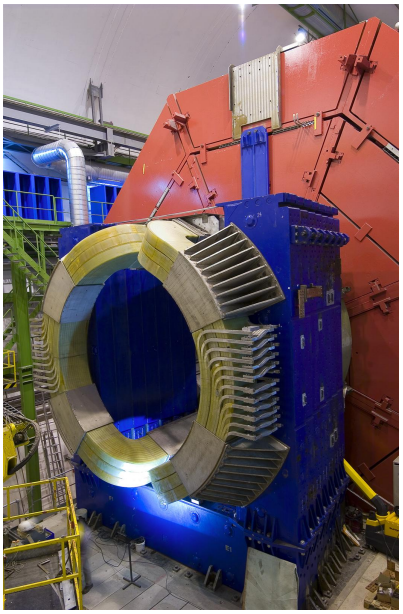

Figure 2.6: ALICE dipole magnet. Figure taken from Ref. [125]

2.2.3.4 Trigger system

The trigger system consists of two trigger stations. Each trigger stations is equipped with two detection planes: one in front and one in the back, totaling 4 detection planes. Each plane consists of 18 resistive plate chamber modules and has a surface area of 6×6 m^2. Due to the fact that muons that reach the trigger must pass through both the front absorber as well as the iron wall, there is a minimum detection threshold on the total momentum of $p = 4$ GeV/c. There is a significant flux of muons from pion and kaon decays, which are not interesting for most analyses. However, they are mainly present at low p_{T} (see Fig. 2.9 in Ref. [126]). In order to avoid triggering on these muons, a p_{T} threshold is applied to the triggering of the individual muon tracks. Two programmable values (low-p_{T} and high-p_{T}) can be used, ranging from ~ 0.5 to ~ 2 GeV/c. The exact configuration depends on the collision system and interaction rate, and can therefore change between different data-taking periods. The trigger system can supply triggers for either single muon tracks (relevant for open heavy flavor or W$^{\pm}$ decays) or for muon pairs (relevant for resonances).

Chapter 3

Z boson: analysis method

The objectives of the analysis are to quantify Z-boson production in Pb–Pb collisions and to compare it to the production in proton–proton (pp) collisions. The production will be expressed as the invariant yield normalized by the average nuclear overlap function, which is defined as

$$\frac{\mathrm{d}N/\mathrm{d}y}{\langle T_{\mathrm{AA}}\rangle} = \frac{N_{\mathrm{Z}}}{A\epsilon \cdot N_{\mathrm{MB}} \cdot \langle T_{\mathrm{AA}}\rangle \cdot \Delta y}. \tag{3.1}$$

N_{Z} is the number of Z bosons and $A\epsilon$ is the acceptance and efficiency of the detector, which corrects for detector accceptance and finite reconstruction and selection efficiency. Strictly speaking, in this analysis the acceptance of the detector is not corrected for, as the yield is given for a specific rapidity interval. Despite this, in literature the term 'acceptance and efficiency' is commonly found, and the same terminology will be adopted in this thesis. N_{MB} is the number of minimum bias (MB) events corresponding to the number of analysed triggered events. Minimum bias refers to the least stringent trigger definition such that the largest fraction of all inelastic collisions are accepted (a more detailed description is given in subsection 3.1.1). The $\langle T_{\mathrm{AA}}\rangle$ represents the average nuclear overlap function and its function is to normalize the Pb–Pb yield to a yield per nucleon–nucleon collision. This allows one to directly compare the yield in Pb–Pb collisions with the production cross section in pp collisions. The last term in the equation is Δy, which is the rapidity interval considered.

Additionally, the nuclear modification factor R_{AA} will be shown. Related to the invariant yield, it is calculated as

$$R_{\mathrm{AA}} = \frac{N_Z}{A\epsilon \cdot N_{\mathrm{MB}} \cdot \langle T_{\mathrm{AA}}\rangle \cdot \sigma_{pp}} = \frac{\mathrm{d}N/\mathrm{d}y}{\langle T_{\mathrm{AA}}\rangle} \cdot \frac{\Delta y}{\sigma_{\mathrm{pp}}}, \tag{3.2}$$

where σ_{pp} is the Z-boson cross section in proton–proton collisions. The nuclear modification factor quantifies the degree to which a Pb–Pb collision can be considered as a linear superposition of pp collisions. A deviation of unity indicates that effects are present in Pb–Pb collisions which are absent in pp collisions.

This chapter is ordered as follows. In the next section, the data sample will be introduced. After that, there are

separate sections each dedicated to the explanation of the terms of Eq. 3.1 and 3.2. The sections appear in the same order as the symbols in the two equations. The last section of this chapter details the systematic uncertainties of the analysis.

3.1 Data sample

The data analysed in this thesis were collected with the ALICE detector and pertain to Pb–Pb collisions at a center-of-mass energy per nucleon pair of $\sqrt{s_{\mathrm{NN}}} = 5.02$ TeV. They were taken in three distinct periods. Periods are generally several weeks long, and consist of runs. A run is an uninterrupted data taking time interval, which can last from a few minutes up to a few hours. Once a run is stopped, the data is transmitted for storage and another run is started. Runs can be stopped for several reasons but the most frequent one is a malfunctioning subdetector. Due to the relatively short timescales of runs, within one run detector and beam conditions can be considered constant. As an aside, the runs discussed here are not to be confused with LHC Runs (with capital R) which last several years and are typically marked by large-scale changes in the detectors and the accelerator itself. In ALICE, each data taking period is appointed a name that consists of the year followed by a letter, starting with *a*, while runs are identified by a unique run number. To specify, the data analysed are those of the 15o, 18q and 18r periods. The 15o period lasted from Nov 24th - Dec 13th 2015, while 18q and 18r lasted from Nov 3rd - 21st and Nov 22nd - Dec 3rd 2018 respectively. Between the 18q and 18r periods, the polarity of the dipole magnet in the muon spectrometer was reversed.

3.1.1 Event selection

In ALICE, various subdetectors are used in the trigger system. A signal from a trigger detector is referred to as a trigger input. Combinations of trigger inputs then define trigger classes that are used to label events. As an important example, the minimum bias (MB) trigger class is defined by the coincidence of an input from both the V0A and V0C detectors. This MB trigger is called the CINT7 trigger class. Here, CINT stands for Collision INTeraction, while 7 refers to the configuration of a coincidence of the V0A and V0C detectors. Initially, other MB triggers with different numbers were also in use. For example, the CINT1 trigger consists of a signal in either the V0A, V0C or SPD. However, as luminosities increased during early LHC operation, the CINT7 trigger class was found to have higher purity than the others [117]. It was consequently adopted as the standard for MB collisions.

Detectors other than the V0 may also provide trigger inputs. The muon spectrometer is equipped with its own trigger system for this very reason. It was designed to be able to provide several trigger inputs, suiting the needs of various types of muon analyses. The unlike-sign dimuon trigger input is fired when two muons of opposite charge pass trough the muon trigger chambers with the additional requirement that each muon has a transverse momentum

above a certain low-p_{T} threshold. This threshold is configurable, but was set to $p_{\mathrm{T}}^{\mu} \gtrsim 1$ GeV/c for the Pb–Pb data taking periods. The combination of simultaneous V0A and V0C inputs (the requirement for MB events) along with the unlike-sign dimuon input defines the CMUL7 trigger class. Here, the *M* indicates a muon event, *U* an unlike sign pair and *L* the low-p_{T} trigger threshold (other trigger classes use a high-p_{T} threshold of $\sim$4.2 GeV/c). In addition to the muon pair triggers, trigger classes for single muons are also defined. The CMSL7 (CMSH7) class is defined by the presence of a single muon above the low-p_{T} (high-p_{T}) threshold in coincidence with the MB requirement.

Because the Z bosons decay into a pair of opposite-sign muons, the analysis was done on CMUL7 events. They were required to have a centrality between 0 and 90%. The centrality was estimated using the V0 detector, and a detailed outline of the framework is provided in subsection 3.6.5. In the 90-100% interval, contamination from electromagnetic interactions becomes considerable so these events were not considered for analysis. However, even in the 0-90% interval, other types of background events contaminate in the dataset. These background events are rejected using criteria that are called the physics selection and are detailed in the following.

3.1.1.1 Physics selection

The physics selection applied on the data comprises two criteria.

The first criterium is to reject beam-background events. These events can be either beam-gas interactions (due to the fact that the beam pipe does not contain a perfect vacuum) or interactions between the beam halo and accelerator components. They can be distinguished using the timing information of the V0A and V0C signals, see Fig. 3.1. The baseline for the collision time is always given by the LHC clock, which gives the reference time for a bunch crossing. For collisions at the IP, the signal arrives in the V0A (V0C) after $\sim 11(3)$ ns, which leads to the main peak visible in the plot. Beam-background events from the A (C) side however, will cause a negative arrival time of -11(-3) ns, leading to the two smaller peaks. By making selections on the arrival time information of the V0A and V0C, such background contributions can be greatly reduced.

The second criterium is a selection on the collision timing of beam-beam events, such that the collisions occur at specific intervals. In the LHC, buckets are spaced 2.5 ns apart, while bunches (i.e. filled buckets) are separated by multiples of 25 ns. This means that at most 1 out of every 10 buckets is filled with a bunch. These are called main bunches. However, particles can drift into an adjacent bucket, which is then named a satellite bunch. Satellite bunches can collide as well, giving rise to main-satellite and satellite-satellite collisions. These types of collisions are called parasitic collisions, and can be rejected using timing information of the ZDC detectors. Namely, the signals in the ZDC originating from parasitic collisions are displaced by multiples of 2.5 ns, as seen in Fig. 3.1. Similarly to the usage of the V0 detectors, selections in the arrival time can be used to reject these unwanted parasitic events.

After the physics selection, 127, 110 and 163 million CMUL7 events remain in the 15o, 18q and 18r periods, respectively. Online measurements were done for the integrated luminosity of the data sets. For 15o, the integrated luminosity is roughly $225\mu\mathrm{b}^{-1}$, while the 18q and 18r periods amount to an integrated luminosity of $525\mu\mathrm{b}^{-1}$ together.

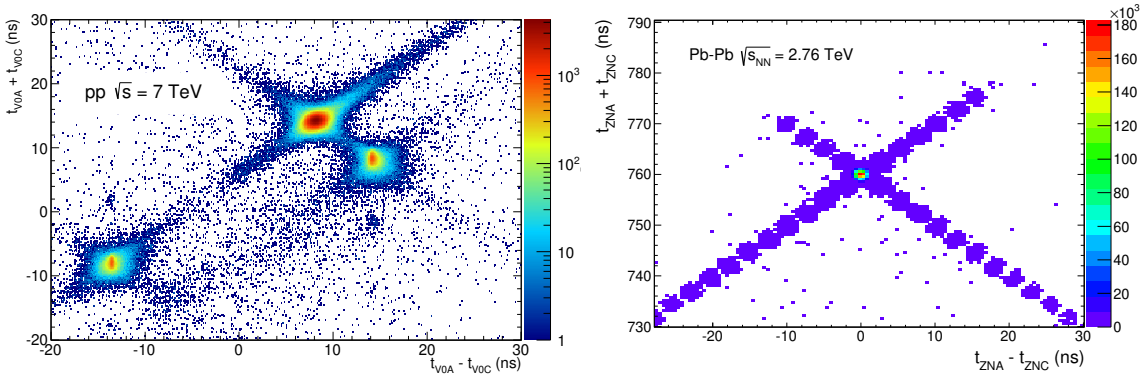

Figure 3.1: Left: signal sum and difference of V0 detectors, used to reject beam-background events. In addition to the main peak from beam-beam events, the left (right) smaller peak is from background events in the A (C) side. Right: signal time sum versus difference of the ZDC detectors, used to reject parasitic collisions. The cluster in the middle originates from main-main collisions, while the diagonals represent parasitic collisions. Both figures taken from [117].

Therefore, the total integrated luminosity of the data set is about $750\mu\mathrm{b}^{-1}$.

3.1.2 Track reconstruction and selection

As muons traverse the spectrometer, they interact with it to produce hits in the tracking and trigger chambers. From the hits in the 5 tracking stations (10 tracking chambers), a muon chamber track is reconstructed. This is done only if there is at least 1 hit in each of the first three stations and 3 in the last two stations. The reconstruction then occurs in two stages.

In the first stage, the reconstruction starts at the station 4 or 5, depending on which station contains two hits. A track segment is made from the two hits, and extrapolated to the other station (5 or 4). The track segment is further extrapolated to stations 3, 2 and 1 to obtain a muon chamber track. From the muon chamber track, the exit point of the track at the front absorber is calculated. The polar angle of this exit point is called θ_{abs}, as seen in Fig. 3.2. In the second stage, the muon chamber track is extrapolated to the vertex through the absorber. The z coordinate of the interaction vertex, determined with the SPD detector, is used for this. The muon chamber track is forced to point to the interaction vertex and additionally, the vertex information is used to apply physical corrections due to energy loss and multiple scattering effects. After these corrections, the muon tracks (as opposed to muon chamber tracks) are considered reconstructed and track parameters such as pseudorapidity and transverse momentum are determined.

Hits are also produced in the trigger chambers. These are not directly used in the track reconstruction, although the reconstruction would not improve much due to the low resolution of the trigger chambers. Instead, by requiring that a reconstructed muon track can be matched to a track segment in the trigger stations, background tracks can be rejected. This is discussed in more detail in the next paragraph. After the matching is performed, the tracks are considered matched muon tracks.

The tracking algorithm reconstructs a large number of tracks, but not all of these are useful for analysis. For example, some tracks can originate from hadrons that make it through the front absorber or from muons that undergo significant scattering in parts of the absorber. In order to improve the quality and purity of the data sample, the following criteria were applied on the reconstructed tracks:

- $-4 < \eta_\mu < -2.5$. This interval matches the geometrical acceptance of the muon spectrometer.

- $170° < \theta_{\text{abs}} < 178°$. Outside of this interval, the absorber consists of high-Z material, see Fig. 3.2. Below $170°$, Pb and polyethylene is used to protect the chambers from tracks that escape the beam, while at $178° < \theta < 180°$ the beam shield made of Pb and Tungsten is located (missing in Fig. 3.2 but shown in Fig. 2.4). Tracks that traverse these high-Z regions of the absorber undergo significant multiple scattering. This complicates the energy loss and scattering corrections and these tracks are therefore rejected. This criterium is different than the one above as the pseudorapidity at the vertex relates to the entrance point at the front absorber, while θ_{abs} relates to the exit point. The combination of both selections ensures that the geometrical acceptance of the detector is respected while not traversing the high-Z region of the front absorber and beam pipe.

- $p_\mu \times DCA < 6\sigma$, where p_μ is the muon momentum and DCA (Distance of Closest Approach) is its closest distance to the primary vertex, as shown in Fig. 3.2. To obtain the DCA, the muon chamber tracks are extrapolated to the z component of the primary vertex. A 2-dimensional DCA (in the xy plane) can subsequently be determined. Due to multiple scattering in the front absorber, the DCA distribution of particles produced in a collision is Gaussian with a width that depends on the amount of material crossed and is proportional to $1/p_\mu$. On the other hand, background tracks (from beam–gas interactions) have a DCA of around 40 cm, independent of p_μ [92]. The measured DCA distribution is therefore fitted with a Gaussian function whose width is used in the product with the momentum of a track to reject background tracks.

- Only muon tracks that can be matched to track segments in the trigger stations were considered. This criterium reduces the low-p_{T} muon background from pions and kaons that do not reach the trigger chambers due to the iron wall placed in front of it.

- $p_{\text{T}} \geq 20$ GeV/c. Due to the high mass of the Z boson, its decay muons will have a large transverse momentum. As will be explained in the following subsection, the signal extraction is performed in the 60-120GeV/c^2 mass interval, so pairs of low-p_{T} muons will not contribute to it.

The cumulative effect these criteria have on the number of (di)muons is shown in Tab. 3.1.

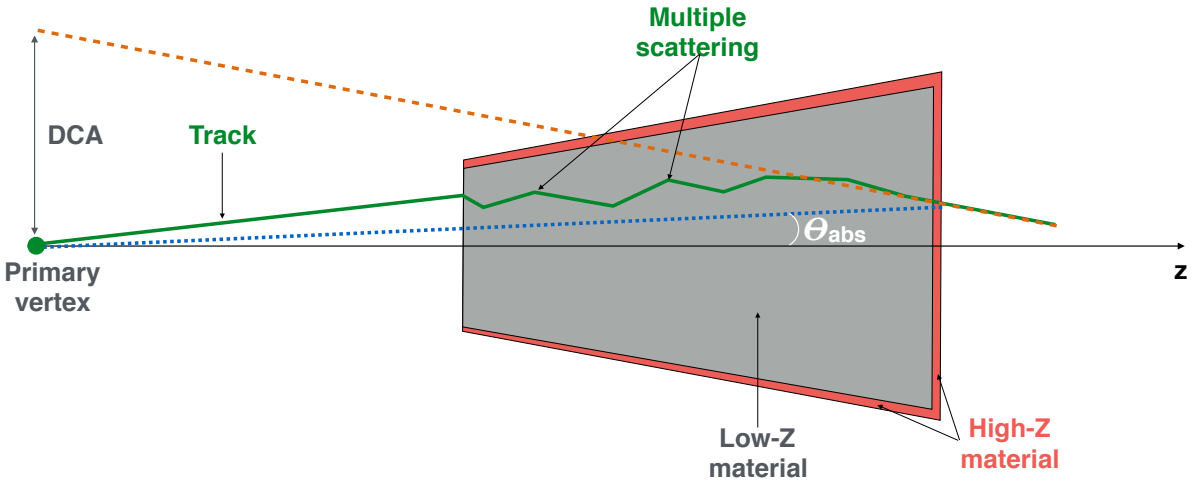

Figure 3.2: Illustration of the distance of closest approach (DCA). The angle at the end of the front absorber θ_{abs} as well as the distance of closest approach (DCA) are shown. For visual clarity, the DCA is strongly exaggerated. Figure taken from [109].

	LHC15o	**LHC18q**	**LHC18r**	
no selection	2080 M	1740 M	2470 M	muons
η_μ selection	1300 M	1118 M	1605 M	muons
η_μ and θ_{abs} selection	1251 M	1087 M	1556 M	mons
η_μ, θ_{abs}, $p_\mu \times DCA$, trigger match	163 M 51 M	146 M 46 M	212 M 66 M	muons unlike sign pairs
previous + $p_{\mathrm{T}} \geq 20$ GeV/c	81	66	105	unlike sign pairs

Table 3.1: Number of muon tracks per step of track selection criteria as well as number of unlike sign dimuon pairs before and after the p_{T} criterium. Values are shown for each data taking period separately.

3.2 Signal extraction N_{Z}

An invariant mass spectrum is computed from all possible opposite-sign muon pairs per event. An additional selection, on the rapidity[1] of the dimuon pair, is applied: $2.5 < y^{\mu\mu} < 4.0$. The number of Z-boson candidates is then obtained by counting the number of dimuons in the 60–120 GeV/c^2 mass interval. This is roughly symmetric around the PDG mass of the Z-boson of 91.1876 ± 0.0021 GeV/c^2 [127]. The invariant mass spectrum is shown in Fig. 3.3. The spectrum is compared to one obtained from simulations (which are discussed in detail in section 3.3.1). The simulated spectrum was scaled to match the number of candidates in the 60-120 GeV/c^2 interval, and shows good agreement with the data. A slight shift in the simulated distribution is present and the effect of this is discussed later, in subsection 3.6.9.

[1] In the ALICE convention, the spectrometer lies at negative z, and therefore at negative (pseudo)rapidity. Due to the symmetric nature of the collisions however, the rapidity of the Z (dimuon) is given in positive values.

3.2.1 Combinatorial background

In addition to decays from Z bosons, opposite-sign muon pairs can also originate from uncorrelated muons. This can happen for instance when several pairs of muons are produced in jets. This combinatorial background from uncorrelated pairs is estimated in the analysis as follows. For muons in the kinematic regime defined by the analysis, the occurrence of same-sign pairs should be of similar magnitude as for unlike-sign pairs. Therefore, the invariant mass distribution for same-sign pairs is also computed. The CMUL7 events, on which the analysis is performed, cannot be used for this, as these events do not trigger on pairs of like-sign muons. Instead, single muon triggered CMSH7 events were used. Using these CMSH7 events, the invariant mass spectrum was computed for like-sign pairs. There is one like-sign pair present in the fiducial region, represented by the red square in Fig. 3.3. This pair was subtracted from the signal extraction to reduce the number of candidates by one. As a check, the unlike-sign pair invariant mass spectrum was also computed from the CMSH7 events and the same spectrum was found as when analysing the CMUL7 events.

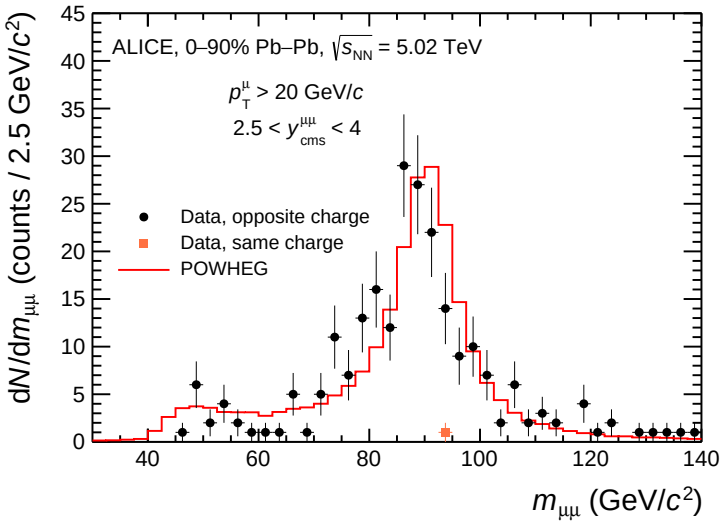

Figure 3.3: Invariant mass distribution of unlike-sign muon pairs, including the 15o, 18q and 18r periods. One like-sign pair, shown in red, was found as well.

3.2.2 Signal extraction results

Table 3.2 shows the number of candidates N_{Z} for each period as well as for the full dataset, which comprises the 15o, 18q and 18r periods. In the table, the aforementioned like-sign signal has already been subtracted. The full fiducial region consists of the muon pairs of muons with $p_{\mathrm{T}} > 20$ GeV/c and $-4 < \eta_{\mu} < -2.5$, and dimuons with rapidity $2.5 < y_{\mu\mu} < 4$. The signal extraction is also shown as a function of centrality and rapidity. For this, several different bin intervals were considered. In the end, the bins were chosen such that each bin has a relative statistical uncertainty of less than 20%. A Poisson distribution is assumed for the number of candidates, meaning that the

statistical uncertainty of each count is given by its square root.

	15o	18q	18r	full
full fiducial region	65^*	59	84	$208^* \pm 14$ (7%)
0-10%	21	18	33	72 ± 9 (12%)
10-20%	18	22	23	63 ± 8 (13%)
20-90%	26^*	19	28	$73^* \pm 9$ (12%)
$2.50 < y < 2.75$	15	15	13	43 ± 7 (15%)
$2.75 < y < 3.00$	20^*	15	32	$67^* \pm 8$ (12%)
$3.00 < y < 3.25$	16	22	28	66 ± 8 (12%)
$3.25 < y < 4.00$	14	7	11	32 ± 6 (18%)

Table 3.2: Number of Z-boson candidates in the fiducial region. The results versus centrality are integrated over rapidity and vice versa. The values with (*) are after the subtraction of one like-sign count found in 15o data sample.

3.3 Acceptance and Efficiency $A\epsilon$

3.3.1 Simulation setup

Muon tracks are reconstructed from hits in the detector chambers. These hits arise from interactions between the muons and the detector. However, due to finite detector resolution differences may be present between track parameters and the muon properties such as transverse momentum. This consequently affects the reconstruction of the Z bosons. In order to obtain the produced yield from the detected yield, the efficiency of the detector must be accounted for, denoted by the symbol $A\epsilon$. The $A\epsilon$ was evaluated using Monte Carlo (MC) simulations, which include both the $\mathrm{Z} \to \mu\mu$ and $\gamma^* \to \mu\mu$ processes.

The simulations consist of a three-step procedure. First, an event generator calculates matrix elements and cross sections of desired processes. Primary particles and their decay products are then created following the cross section distributions. Some event generators also include initial and final state radiations, and subsequent parton showers. Secondly, the particles are passed to a transport code (GEANT3 [128]) which simulates the propagation of the particles through the detector as well as their interactions with the detector. These interactions then create hits in detection elements. Thirdly, a reconstruction algorithm uses the hits as input to reconstruct particle tracks that are used for analysis. During data taking, only the third step can be done.

In the MC simulations, Z bosons and virtual photons were set to decay to two muons, each with a $p_{\mathrm{T}} > 15$ GeV/c. Two separate sets of MC productions were used in the evaluation of the $A\epsilon$. The two sets differ in the event generator employed.

- One set was produced using PYTHIA 8 which is an event generator at leading order (LO) [129]. In Pb–Pb collisions, the $A\epsilon$ depends on the detector occupancy and therefore on the event centrality. Unfortunately, simulations generally do not properly reproduce multiplicities in Pb–Pb collisions. Therefore, an embedding technique was used, which will be explained now. Z bosons, decaying into muon pairs, were simulated from

pp collisions and steps 1 and 2 of the procedure above were followed. At this point, the hit information from the muon interactions with the detector is obtained. This information is then added to the raw data (i.e. hits) from measured Pb–Pb events. Finally, the reconstruction algorithm was reran on embedded event, which contains both the measured and simulated hits. Because the embedding essentially adds a simulated event into a measured event, this ensures that multiplicities are realistic. This way, the centrality dependence of the $A\epsilon$ can be properly taken into account. In the remainder of the text, this set will be referred to as the embedded simulations.

- On the other hand, a set using POWHEG as event generator was also used [130]. POWHEG can generate events at next-to-leading order (NLO) accuracy. Because POWHEG only produces the events, it was interfaced with PYTHIA 6 [131] which handles initial/final state radiation and decay kinematics. As was the case for the embedding, the Z bosons were created from simulated pp collisions. In contrast, no embedding technique was done with this set. For brevity, this set will be referred to as the POWHEG simulation, although it also includes PYTHIA 6.

Ideally, the embedding would have been done with POWHEG as event generator instead of PYTHIA8. This would combine the higher order calculations in POWHEG together with the centrality dependence of the embedding in a single set of simulations. However, the embedding technique is computationally intensive. Therefore, in order to prevent various analysers from each creating their own embedding, one multi-purpose embedding simulation was created by a senior member of ALICE. This embedding contains electroweak bosons and also several quarkonia. For the Z bosons, the standard generator in PYTHIA was used. On the other hand, the POWHEG simulations were created privately by the Z-boson analysers and only for Z bosons. Due to a lack of computing resources, the POWHEG events were not embedded. In the end, both sets of simulations were combined, as will be explained in subsections 3.3.4 and 3.3.5.

3.3.2 Calculation of $A\epsilon$

In the simulations one has access to kinematic variables of all particles at both generated and reconstructed levels. The procedure for the signal extraction explained in section 3.2 was used to extract the number of reconstructed dimuon pairs N_{rec} as well as the number of generated dimuon pairs N_{gen}, so that the $A\epsilon$ is calculated as

$$A\epsilon = \frac{N_{\mathrm{rec}}}{N_{\mathrm{gen}}}. \tag{3.3}$$

For the reconstructed pairs it was checked that the decay muons originated from a Z boson. As a technical remark, N_{gen} refers to the number of generated dimuon pairs that obey the selection criteria and not directly the number of generated Z bosons. Due to final state radiation, differences in (transverse) momentum of the muons may arise. This

subsequently influences the invariant mass of the dimuons. Because the $A\epsilon$ is computed specifically for dimuons in the 60-120 GeV/c^2 interval, this can influence the value of the $A\epsilon$. In the data, the muons that are measured in the detector have already undergone final state radiations. For consistency, the reconstructed dimuon pairs (therefore including radiation) were used for the calculations.

3.3.3 Run dependence of $A\epsilon$

Detector conditions can vary in time, for example due to different bunch filling schemes or random subdetector malfunctions. As a consequence, the $A\epsilon$ will vary as well. In order to take this time dependence into account, the $A\epsilon$ is calculated on a run-by-run basis. Figure 3.4 shows the $A\epsilon$ obtained from the POWHEG simulation as a function of the run number for the 18q and 18r periods. The $A\epsilon$ is relatively stable, with the exception of some runs that show a lower $A\epsilon$. This behavior originate from temporary issues such as high-voltage trips in the tracking chambers.

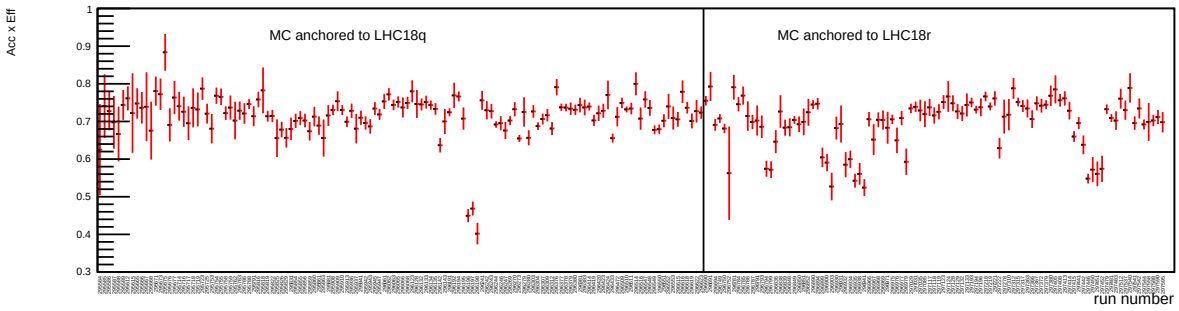

Figure 3.4: Detector acceptance and efficiency as a function of data taking run for the LHC18q and LHC18r periods. POWHEG was used as event generator for the simulations.

These run-by-run values are then averaged to a single value. However, not all runs contain the same number of stored events. Differences can arise for example from differences in run duration, variability of beam intensity during a fill or downscaling factors. Therefore, instead of simply taking the arithmetic average, a weighted average is calculated using the number of CMUL7 events N_{CMUL} in the corresponding data taking runs. The calculation is therefore done as

$$A\epsilon = \frac{\sum_i A\epsilon_i \, N_{\mathrm{CMUL},i}}{\sum_i N_{\mathrm{CMUL},i}}, \tag{3.4}$$

where the subscript i indicates a run.

3.3.4 Centrality dependence of $A\epsilon$

Figure 3.4 shows the run-by-run values of the $A\epsilon$ for the 18q and 18r periods, as computed with the POWHEG simulation. The POWHEG events were not embedded in Pb–Pb events and therefore by default contain no centrality dependence. In central Pb–Pb collisions, the number of produced particles is very high, which subsequently leads

to a high detector occupancy. The high occupancy negatively impacts the trigger efficiency. The tracking efficiency is also affected, but to a lesser degree due to the higher granularity ($1.08 \cdot 10^6$ readout channels in the tracking chambers versus $2.1 \cdot 10^4$ in the trigger chambers [116]). To take the centrality dependence of the $A\epsilon$ into account, the embedded simulations were used. Figure 3.5 shows the centrality dependence of the $A\epsilon$ for the 15o, 18q and 18r data taking periods. In peripheral collisions, the $A\epsilon$ is stable and the value is relatively constant. Towards central collisions, the occupancy increases and the $A\epsilon$ decreases, as expected. In general, the $A\epsilon$ in 15o is higher than in the 18q and 18r periods. This can be attributed to detector deterioration as well as an increased frequency of detector issues due to higher beam intensities during the 2018 data taking. Namely, the higher beam intensity results in higher activity in the detector, which can lead to high-voltage trips in the detector elements. In 15o (18q and r), the $A\epsilon$ at the plateau is about 76% (71%), decreasing to 71% (65%) in the most central collisions. Comparing with the POWHEG simulations, $A\epsilon$ is higher than the embedded simulations in the 15o period, while it is lower in the 18q and 18r periods.

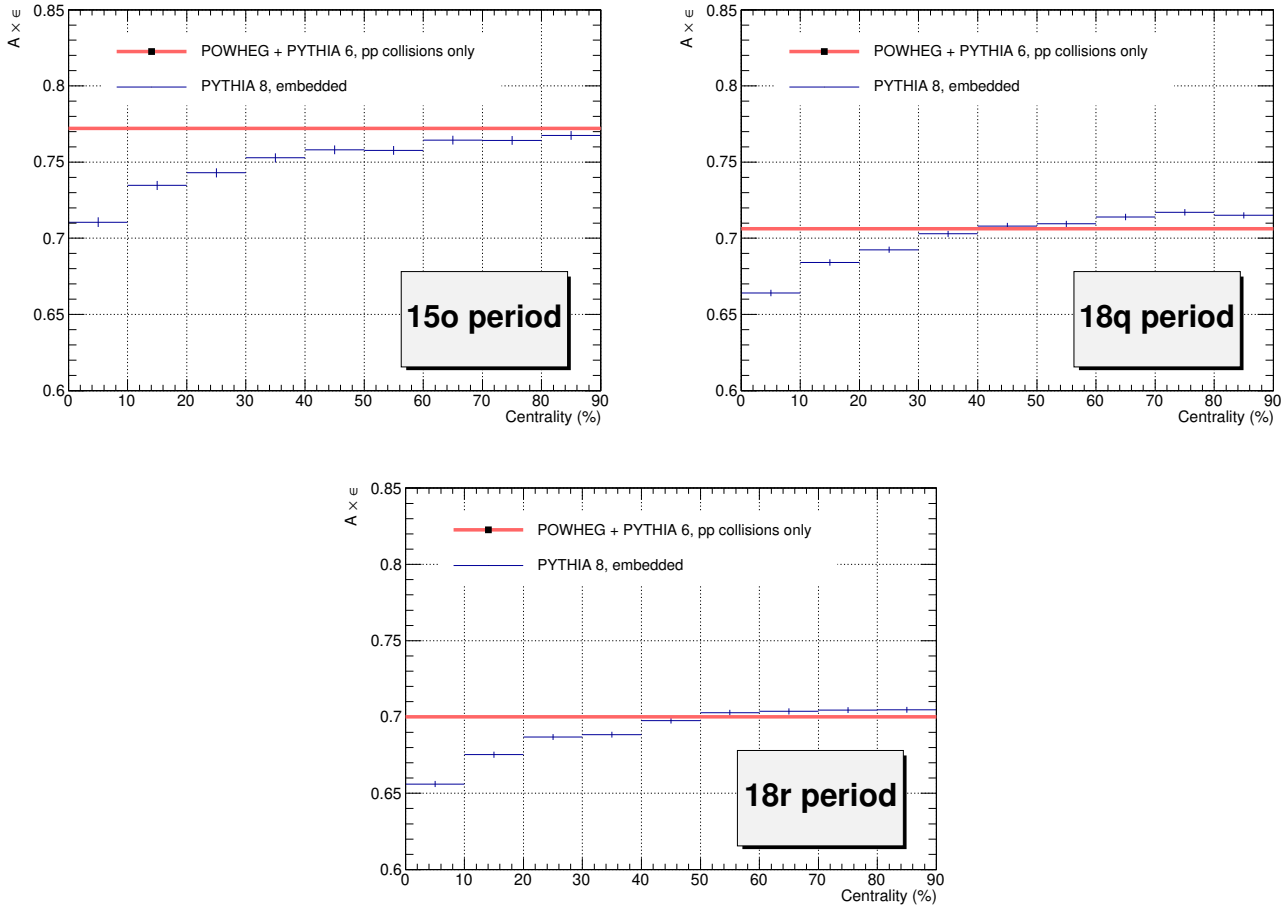

Figure 3.5: Centrality dependence of the $A\epsilon$, as calculated using the PYTHIA 8 embedded simulation. The POWHEG value (calculated using pp, therefore containing no centrality dependence) is shown as well.

The embedding simulations were set up such that each centrality interval contains the same number of generated

Z bosons. In real CMUL7 events however, the distribution of Z bosons is skewed towards central events. Similarly to the case of the run-by-run averaging explained earlier, an arithmetic average of the centrality intervals would be biased because the centrality distribution of Z bosons would be neglected. In order to obtain the proper value of the $A\epsilon$ for different centrality intervals, the $A\epsilon$ was first calculated in 10% wide bins, as can be seen in Fig. 3.5. After this, a weighted average was computed. Ideally, the measured number of Z-boson candidates per centrality interval would be used for such an averaging, because such a quantity naturally reflects the proper centrality distribution of Z bosons. However, the low number of candidates does not allow for such a weighting, due to large statistical uncertainties in the more peripheral centrality intervals. Instead, the average number of binary collisions $\langle N_{\mathrm{coll}} \rangle$ per centrality bin was used. Because the Z bosons are exclusively produced in the initial hard scatterings, their production is directly proportional to the number of binary collisions [132]. Therefore, $\langle N_{\mathrm{coll}} \rangle$ can be used as a substitute for the weights. The values of $\langle N_{\mathrm{coll}} \rangle$ were obtained from MC Glauber simulations [133], and are shown in Tab. 3.6. As an example, the $A\epsilon$ for the 0–90% centrality bin was calculated as

$$A\epsilon(\mathrm{embedding}, 0-90\%) = \frac{\sum_{c=0-10\%}^{80-90\%} A\epsilon(\mathrm{embedding}, c)\langle N_{\mathrm{coll}} \rangle_c}{\sum_{c=0-10\%}^{80-90\%} \langle N_{\mathrm{coll}} \rangle_c}, \tag{3.5}$$

where the subscript c indicates a centrality bin.

In pp collisions, similar multiplicities are reached as in peripheral Pb–Pb collisons. Therefore, the $A\epsilon$ value of the POWHEG simulation should be equal to that of the embedded simulations in peripheral events. The $A\epsilon$ value per centrality interval was then calculated as

$$A\epsilon(c) = A\epsilon(\mathrm{POWHEG}) \times \frac{A\epsilon(\mathrm{embedding}, c)}{A\epsilon\,(\mathrm{embedding}, 80-90\%)}. \tag{3.6}$$

where the subscript c indicates the centrality bin. This method combines the higher accuracy of the POWHEG simulations (NLO instead of LO) together with the centrality dependence of the embedding. Figure 3.5 shows that there is a discrepancy between the $A\epsilon$ in the POWHEG simulations and in the $80-90\%$ centrality bin in the embedding simulations. The discrepancies, going from the POWHEG value to the value from the $80-90\%$ centrality bin in the embedding, are -0.6%, $+1.2\%$ and $+0.6\%$, in the 15o, 18q and 18r period respectively. This challenges the assumption that value of the $A\epsilon$ in the POWHEG simulation should be equal to that in the peripheral events of the embedding, which was used in Eq. 3.6. In order to test the stability of the $A\epsilon$, two methods were used to compute the $A\epsilon$ over the full data set. The first method is the one using Eq. 3.6, combining the POWHEG values with the centrality dependence given by the embedding. For the second method, the $A\epsilon$ was computed using only the embedding simulation (without normalization to the POWHEG value). The difference in $A\epsilon$ between the two methods was found to be $< 0.5\%$ with the exception of one the $3.25 < y < 4.00$ rapidity bin in which it was 1% (the rapidity dependence is detailed in the following subsection). In subsection 3.6.8, the systematic uncertainty of the $A\epsilon$ is detailed. The uncertainty is estimated to be 5%, which covers the discrepancy observed between the two

methods described above.

3.3.5 Rapidity dependence of $A\epsilon$

The invariant yield will be presented as a function of rapidity, so a rapidity-dependent $A\epsilon$ was calculated. The rapidity dependent yield is integrated in centrality, so the same procedure was applied to the $A\epsilon$. Namely, for a specific rapidity interval Δy, the $A\epsilon$ was first calculated on a run-by-run basis in 10% wide centrality bins. The run-weighted average was then computed for each centrality bin. After this, the $A\epsilon$ was calculated for the 0-90% centrality interval, using $\langle N_{\mathrm{coll}} \rangle$ as weights. Lastly, the embedded simulations were combined with the POWHEG simulations. To increase the statistical precision, the 70–90% interval was used for peripheral events instead of the 80–90% considered earlier, as the $A\epsilon$ already reaches its plateau starting at 70% centrality. The $A\epsilon$ as a function of rapidity was then calculated as

$$A\epsilon(\Delta y) = A\epsilon(\mathrm{POWHEG}, \Delta y) \times \frac{A\epsilon(\mathrm{embedding}, 0-90\%, \Delta y)}{A\epsilon\,(\mathrm{embedding}, 70-90\%, \Delta y)}. \tag{3.7}$$

3.3.6 Summary

The values of the detector acceptance and efficiency are shown in Tab. 3.3. They are shown both as a function of centrality and rapidity. The $A\epsilon$ as a function of centrality is integrated over rapidity and vice versa. The obtained values are computed specifically for muons that satisfy the track selection criteria outlined in section 3.1.2. For these values, the weighted average of the three periods was computed, using the number of CMUL7 events in each period as weight (see Eq. 3.4). This essentially treats the entire ensemble of runs as one large data taking period.

Dimuon Rapidity	Centrality	$A\epsilon$ (%)
$2.5 < y < 4$	$0-90\%$	68.83 ± 0.20
$2.5 < y < 4$	$0-10\%$	67.10 ± 0.27
	$10-20\%$	69.08 ± 0.27
	$20-90\%$	70.77 ± 0.20
$2.50 < y < 2.75$	$0-90\%$	72.21 ± 0.42
$2.75 < y < 3.00$		71.68 ± 0.27
$3.00 < y < 3.25$		67.19 ± 0.29
$3.25 < y < 4.00$		65.25 ± 0.38

Table 3.3: Detector acceptance and efficiency as a function of centrality and rapidity.

3.4 Number of minimum bias events N_{MB}

One objective of the analysis is to compare the yield in Pb–Pb collisions with the theoretical cross section in pp collisions. Although the latter can be calculated for a specific kinematic region (with selections on muon p_{T} and

dimuon rapidity), it is not computed for specific triggers or detectors. Effectively, the theoretical cross section is calculated for minimum bias events. However, the analysis is performed on CMUL7 events, which are events containing at least one unlike-sign dimuon pair. Therefore, the number of CMUL7 events must be converted into an equivalent number of minimum bias events. This conversion is given by the normalization factor, as

$$N_{\mathrm{MB}} = F_{\mathrm{norm}} \times N_{\mathrm{CMUL7}}, \tag{3.8}$$

where N denotes the number of events and F_{norm} the normalization factor. It should be noted that there exist several trigger classes for MB events. As is the case for the analysis, both the MB as well as CMUL7 events must pass the physics and centrality selections described earlier.

There are three different methods to obtain the normalization factor. Two of these use offline data, i.e. stored events. However, not all triggered events are stored. This would be unfeasible due to storage limitations and because the readout time for some detectors is too slow to allow this. Therefore, only a fraction of triggered events is stored, a procedure referred to as downscaling. The third method makes use of the online trigger counters. These count the number of instances that various trigger inputs were fired. Because the counting precedes any event storage and therefore downscaling, the online method benefits from higher statistical precision.

In the following, the three methods will be outlined, after which the description and choice of the MB triggers is given. Then, the calculation of the normalization factor per run and period are outlined. Finally, the obtained normalization factors are shown in a summary table.

3.4.1 Methods

The first method is called the offline direct method. For the calculation of the normalization factor, the trigger inputs in all MB events that pass the physics selection in a run are inspected (see 3.1.1). The normalization factor is obtained by

$$F^{i}_{\mathrm{norm}} = \frac{N^{i}_{\mathrm{MB}}}{N^{i}_{\mathrm{MB\&0MUL}}}, \tag{3.9}$$

where N denotes the number of a certain event per run i, and 0MUL the trigger input for an unlike-sign dimuon pair. For example, the CINT7 trigger class is defined by the 0VBA && 0VBC trigger inputs, which represent a hit in the V0A and V0C respectively. However, it can occur that the 0MUL input was also fired for a CINT7 event. Therefore, this method essentially computes the inverse of the fraction of MB events that contains an unlike-sign muon pair.

A second method, called the offline indirect method was also used. In this method, the CMSL7 and 0MSL were used as intermediate trigger class and trigger input respectively. The reason for using the intermediate class is to increase the statistical precision of the calculation. Namely, there should be a larger overlap between the 0MSL

input than 0MUL in MB events due to the less stringent criterium of only 1 muon present instead of an unlike-sign pair. By the same reasoning, there should be a larger overlap between CMSL7 events and CMSL7 events where the 0MUL input was fired. For the indirect method, the trigger inputs of all MB events that pass physics selection and all CMSL7 events that pass physics selection were inspected. The normalization factor is then calculated as

$$F^i_{\text{norm}} = \frac{N^i_{\text{MB}}}{N^i_{\text{MB\&0MSL}}} \times \frac{N^i_{\text{CMSL7}}}{N^i_{\text{CMSL7\&0MUL}}}. \tag{3.10}$$

Thirdly, it is also possible to use the online trigger counters. However, no physics selection is applied at the counting stage, so they also contain background events such as from beam-gas interactions. Therefore, a correction is applied to the counters, using the physics purity. This is defined as the fraction of events that pass the physics and centrality selections, and is computed using offline data. For this method, the normalization factor is calculated as

$$F^i_{\text{norm}} = \frac{L0b^i_{\text{MB}} \times P^i_{\text{MB}}}{L0b^i_{\text{CMUL7}} \times P^i_{\text{CMUL7}}}, \tag{3.11}$$

where L0b indicates the number of online trigger counts and P the physics purity for a run i.

Regardless of the method used, the normalization factor must be corrected for pileup events. These arise when multiple collisions occur within the time resolution of the detector. The reason for this pileup correction is that no pileup events were rejected in the data sample. When determining the number of MB events however, they must be taken into account in the normalisation factor. The values in Eqs. 3.9, 3.10 and 3.11 are therefore multiplied by

$$F^i_{\text{pileup}} = \frac{\mu^i}{1 - \mathrm{e}^{-\mu^i}}, \tag{3.12}$$

where μ^i is the mean number of collisions per bunch crossing in a run i. μ^i itself is calculated as

$$\mu^i = -\ln(1 - \frac{P^i_{\text{MB}} \times L0b\text{Rate}^i_{\text{MB}}}{n^i_b \times f_{\text{LHC}}}), \tag{3.13}$$

where P^i_{MB} is the purity factor, $L0b\text{Rate}^i_{MB}$ the rate of MB data taking, n^i_b the number of colliding bunches of a given run i and $f_{\text{LHC}} = 11245$ Hz the revolution frequency of LHC. In Pb–Pb collisions, the interaction rate is much lower than in pp and p–Pb collisions and the order of magnitude of the pileup correction is of the per mille level.

3.4.2 Choice for MB trigger

There are several triggers that can serve as MB triggers. Depending on the period and method, different MB triggers were used for the calculation of the normalization factor. In this subsection, the choice of MB trigger for each method is outlined.

Both offline methods used the CINT7 trigger for the 15o period. In 2018 a related trigger was introduced, called the CINT7ZAC trigger. This trigger class requires a 1ZAC input on top of the 0VBA && 0VBC inputs mentioned earlier. The 1ZAC is defined as the coincidence of a signal in the ZNA and ZNC detectors, which are subdetectors of the ZDC. Its purpose is to remove electromagnetic contributions, which are present mainly in peripheral events. The CINT7ZAC trigger is also less downscaled than the CINT7, which yields a higher precision in the determination of the normalization factor. Therefore, CINT7ZAC was used for the 18q and 18r data for both offline methods. However, for the CINT7(ZAC) triggers, the normalization factor for the online method was found to be systematically higher than for the offline methods. This behaviour had also been found in an earlier ALICE analysis and was attributed to V0 afterpulses, which caused an overcounting of the CINT7(ZAC) triggers.

For the online method, another MB trigger class, called C0V0M, was used. The C0V0M trigger fires when the sum (instead of the logical AND, for CINT7) of the V0A and V0C surpasses a threshold. The threshold is set such that the C0V0M does not cover the entire 0–90% centrality range, as can be seen in Fig. 3.6. The C0V0M is therefore by design a semi-central, or high-multiplicity trigger. In the calculations involving C0V0M events, only the most central 60% in 2015 and the most central 50% in 2018 were used. Subsequently, the normalization factor must be rescaled to obtain a normalization factor in the 0–90% centrality range. Because there is no selection on the final state in MB events, the centrality distribution should by definition be flat. In Fig. 3.6, it can be seen that this is indeed the case. Therefore the normalization factor was rescaled by 9/6 in the 15o period and 9/5 in 18q and 18r. Because there are less C0V0M events than CINT7(ZAC), C0V0M was not used as the MB trigger for the offline methods.

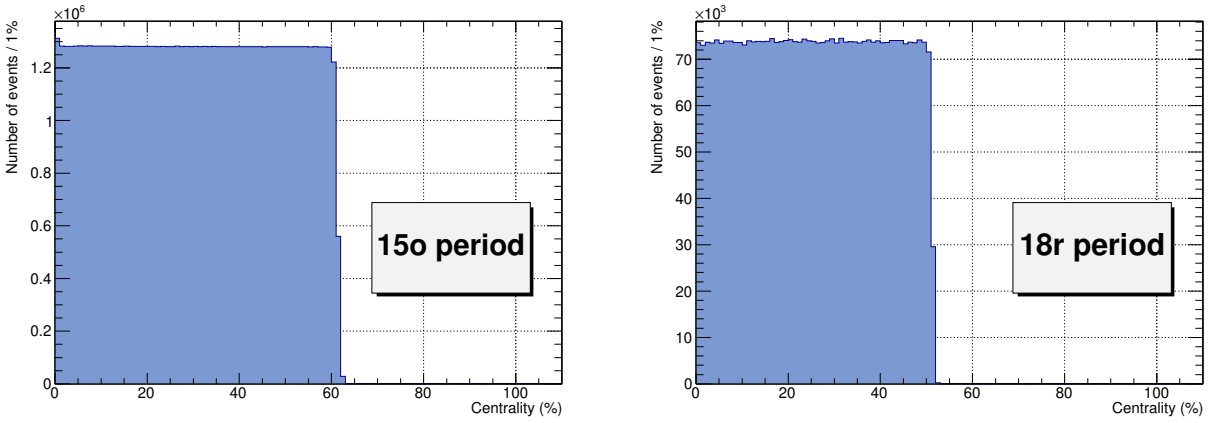

Figure 3.6: Centrality distribution of the C0V0M trigger for the 15o (left) and 18r (right) periods.

3.4.3 Run by run normalization factor

The normalization factor for each method was determined on a run-by-run basis. Fig. 3.7 shows the run-by-run values of the normalization factor for the three data taking periods.

Similarly to what is done for the $A\epsilon$, these run-by-run values are then averaged using the number of CMUL7

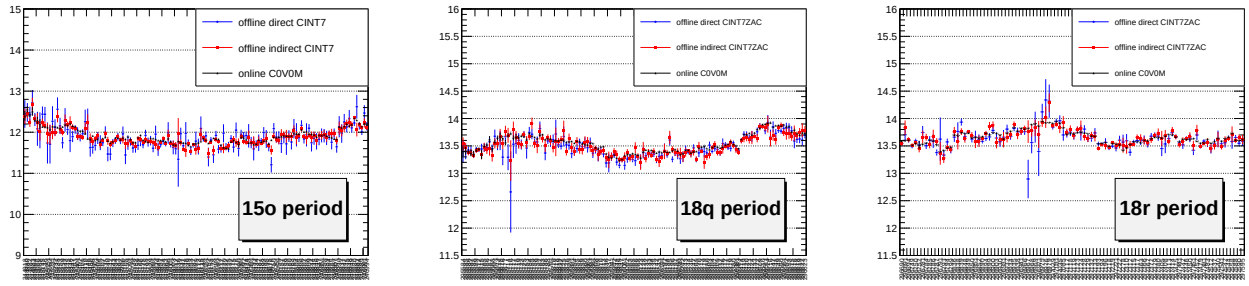

Figure 3.7: Run by run normalization factor for 15o, 18q and 18r periods.

events per run as weight. Because the statistical precision of the online method is the largest, it was taken as the central value of the normalization factor. The systematic uncertainty due to the normalization factor will be discussed in subsection 3.6.2.

3.4.4 Centrality dependent normalization factor

The Z-boson production will be presented as a function of centrality. To obtain the number of MB events in a given centrality range, one can either compute a centrality dependent normalization factor, or calculate the normalization with respect to the full 0–90% centrality range and then rescale the number of events. The latter relies on the flatness of the centrality distribution of MB events. This should by definition be flat because MB events are supposed to represent collisions without specific selections on physics (such as the presence of a dimuon pair). To this end, the number of MB events per centrality interval was calculated both with the normalization factor over the full centrality range as well as centrality dependent. The values for both calculations are shown in Tab. 3.4. The two methods are well in agreement with each other, so it was not found necessary to compute a normalization factor per centrality interval. Therefore, in the end only one normalization factor is reported per period.

centrality	cent. dep. norm. million MB events	rescaled norm. million MB events
0-90	5190.35	
0-10%	576.37	576.71
10-20%	576.64	576.71
20-90%	4037.76	4036.94

Table 3.4: Comparison of the number of minimum bias events calculated using either a centrality dependent normalization factor or a full 0-90% one that is rescaled assuming MB flatness.

3.4.5 Summary

The values of the normalization factor for each period are shown in Tab. 3.5. Together with the total number of CMUL7 events, the number of equivalent MB events N_{MB} can be obtained according to equation 3.8. To be precise, the normalization factors shown were used to convert the number of CMUL7 events in the 0-90% interval to the

number of MB events in the 0-90% interval. The statistical uncertainties of the values were found to be negligible. Instead, only the systematic uncertainties on the values are shown. The procedure to obtain the systematic uncertainty is detailed in subsection 3.6.2. To determine the normalization factor for the full data set, the weighted average of the three periods was calculated, using the total number of CMUL7 events per period as weight.

	F_{norm}	N_{CMUL7}
15o	11.88 ± 0.03 (0.3%) syst	127 M
18q	13.55 ± 0.06 (0.5%) syst	110 M
18r	13.65 ± 0.02 (0.1%) syst	163 M
full	13.06 ± 0.07 (0.5%) syst	400 M

Table 3.5: Values of the normalization factor and number of CMUL7 events per period as well as for the full data set. The absolute systematic uncertainty is shown, followed by the corresponding relative systematic uncertainty in parentheses.

3.5 Nuclear overlap function $\langle T_{\mathrm{AA}} \rangle$ and proton–proton cross section σ_{pp}

In this section, the values of the average nuclear overlap function $\langle T_{\mathrm{AA}} \rangle$ and proton–proton cross section σ_{pp} used in Eqs. 3.1 and 3.2 are given.

3.5.1 Nuclear overlap function

Per Pb–Pb collision, the Z-boson yield is higher than in a pp collision, simply because there are more colliding nucleons. In order to make a fair comparison with the pp cross section, the yield in Pb–Pb must be normalized by the number of binary collisions. This normalization is given by the $\langle T_{\mathrm{AA}} \rangle$. The values of the $\langle T_{\mathrm{AA}} \rangle$ are calculated from Glauber MC simulations, and were taken from Ref. [133]. For the bins unlisted in [133], an averaging over centrality was calculated, using $\langle N_{\mathrm{coll}} \rangle$ as weights. Due to correlations between the bins, the uncertainty was conservatively estimated as the average of the uncertainties as well. The values of the $\langle T_{\mathrm{AA}} \rangle$ are shown in Tab. 3.6, along with the systematic uncertainties which are detailed in subsection 3.6.3. The last column shows the average number of participating nucleons, scaled by the average number of binary collisions. In heavy-ion collisions, the centrality of an event can also be expressed by the average number of participants $\langle N_{\mathrm{part}} \rangle$. Participants are nucleons that undergo at least one binary collision. However, because the Z bosons are created in hard scatterings, their production scales with the number of binary collisions. By scaling $\langle N_{\mathrm{part}} \rangle$ by $\langle N_{\mathrm{coll}} \rangle$, more central events are given larger weights to reflect that the majority of binary collisions occur in these events. This $\langle N_{\mathrm{coll}} \rangle$-weighted average of $\langle N_{\mathrm{part}} \rangle$, shown in the last column of Tab. 3.6 is therefore a better measure of the centrality.

centrality	$\langle T_{\mathrm{AA}} \rangle (1/\mathrm{pb})$	$\langle N_{\mathrm{part}} \rangle$	$\langle N_{\mathrm{coll}} \rangle$	$\langle N_{\mathrm{part}} \rangle_{\langle N_{\mathrm{coll}} \rangle}$
0-90%	6.28 ± 0.07 (1.0%)	125.91 ± 0.80	424.59 ± 5.51	260.51 ± 1.00
0-10%	23.26 ± 0.17 (0.7%)	357.30 ± 0.75	1572.00 ± 17.40	357.30 ± 0.75
10-20%	14.40 ± 0.13 (0.9%)	262.00 ± 1.15	973.40 ± 11.30	262.00 ± 1.15
20-90%	2.70 ± 0.04 (1.5%)	73.41 ± 0.75	182.27 ± 2.98	140.32 ± 1.19

Table 3.6: Values for nuclear overlap function $\langle T_{\mathrm{AA}} \rangle$, number of participating nucleons $\langle N_{\mathrm{part}} \rangle$, number of binary collisions $\langle N_{\mathrm{coll}} \rangle$ and weighted number of participants as a function of centrality. The uncertainties shown are systematic and for the $\langle T_{\mathrm{AA}} \rangle$, the relative uncertainties are shown as well in parentheses. Values were taken from [133].

3.5.2 Proton–proton cross section

One of the tools to quantify physical effects in particle production due to the Pb-nucleus environment is the R_{AA}. For the calculation of the R_{AA}, the proton–proton cross section is needed. Ideally, a measurement of the Z-boson production at the same center-of-mass energy would be used for this. Although data were collected from pp collisions at $\sqrt{s} = 5.02$ TeV, the luminosity is not high enough to allow for the measurement of Z bosons. Additionally, no measurements done by other experiments in the kinematic regime of the analysis ($2.5 < y^{\mu\mu} < 4$, $p_{\mathrm{T}}^{\mu} > 20$ GeV/c) exist. Instead, theoretical values were used, provided by H.Paukkunen [134]. The values of σ_{pp} were calculated using NLO pQCD, and are shown in Tab. 3.7. The cross section was computed for the fiducial region detailed in section 3.2, with the same selections as for the signal extraction. This means that the single muons were required to have $p_{\mathrm{T}}^{\mu} > 20$ GeV/c and $-4 < \eta^{\mu} < -2.5$ while for the dimuon pairs additional selections of $2.5 < y_{\mu\mu} < 4$ and $60 < m_{\mu\mu} < 120$ GeV/c^2 were applied. The systematic uncertainties on the cross section, which will be detailed in subsection 3.6.4, are also shown in the table.

y range	$\sigma^{pp}_{Z\to\mu^-\mu^+}$ [pb]
$2.5 < y < 4$	11.92 ± 0.46 (3.9%)
$2.50 < y < 2.75$	1.69 ± 0.06 (3.5%)
$2.75 < y < 3.00$	3.86 ± 0.14 (3.7%)
$3.00 < y < 3.25$	3.99 ± 0.16 (4.0%)
$3.25 < y < 4.00$	2.38 ± 0.12 (5.0%)

Table 3.7: Values for pp cross section σ_{pp}, provided by Ref.[134]. The absolute systematic uncertainty is shown, followed by the corresponding relative systematic uncertainty in parentheses.

3.6 Systematic uncertainties

In this section, the systematic uncertainties related to the analysis will be presented. Each systematic uncertainty is detailed in a separate subsection, and in the last subsection a summary table is given.

3.6.1 Background estimation

The method used for the signal extraction is to count the number of dimuon entries in the 60–120 GeV/c^2 mass region. This relies on the assumption that this region contains only signal candidates. It is therefore important to check and verify this assumption. In an earlier ALICE publication, also on Z-boson production in Pb–Pb collisions at $\sqrt{s_{\rm NN}} = 5.02$ TeV, possible backgrounds were analysed using MC simulations [95]. Because the collision system, collision energy and fiducial selections are identical between the two analyses, the same values were assigned in this thesis. A description of each background will be given here.

- Heavy quarks, present in beauty or charm hadrons, can decay (semi-)leptonically into a W which then decays into a $\mu\nu$ pair. If two such decays occur, a muon pair can be formed that could potentially be a background in the analysis. To estimate such a contribution, D (B) $\rightarrow \mu\nu$ samples were generated and normalized to their production cross section using first order next-to-leading-log (FONLL) [135] calculations and the integrated luminosity of the data set used. The FONLL code was interfaced with PYTHIA 6 for the subsequent parton shower and decay kinematics. It was found that due to the rapidly decaying $p_{\rm T}$ spectrum, the $p_{\rm T} > 20$ GeV/c cut removes any contributions from this source of background.

- A pair of t quarks can also produce a pair of muons, in a $t\bar{t} \rightarrow \mu\mu$ process. In this case, the decays occur in isolated quarks instead of quarks contained in hadrons. The $\mathrm{Z}/\gamma^* \rightarrow \tau\tau \rightarrow \mu\nu\mu\nu$ process was also considered. Here, instead of directly decaying into a pair of muons, the Z/γ^* first decays into a pair of tauons which then decay weakly into a pair of muons and neutrinos. Because the neutrino's carry away part of the energy, the distribution of this process does not follow the peak structure of the direct muon decay. Background contributions from these two processes were estimated from a POWHEG simulation, interfaced with PYTHIA 6. Figure 3.8 shows the distributions of these, compared to the main process of $\mathrm{Z}/\gamma^* \rightarrow \mu\mu$. As can be seen in the figure, in the 60-120 GeV/c^2 interval, contributions from these processes are small.

The fraction of dimuons of these background processes of the main $\mathrm{Z}/\gamma^* \rightarrow \mu\mu$ process (with the same kinematic selections applied as in data) was less than 1%. A conservative value of 1% was therefore assigned as the systematic uncertainty. Note that the backgrounds discussed in this subsection differ from the combinatorial background described earlier. Namely, they only contribute a systematic uncertainty, while the combinatorial background is subtracted from the extracted signal to obtain the central value of the number of candidates.

3.6.2 Normalization factor

The systematic uncertainty of the normalization factor arises from the different methods that can be used to determine it, which give different values of the normalization factor. The central value of the normalization factor is given by the online method. The systematic uncertainty is then assigned as the largest difference between online method

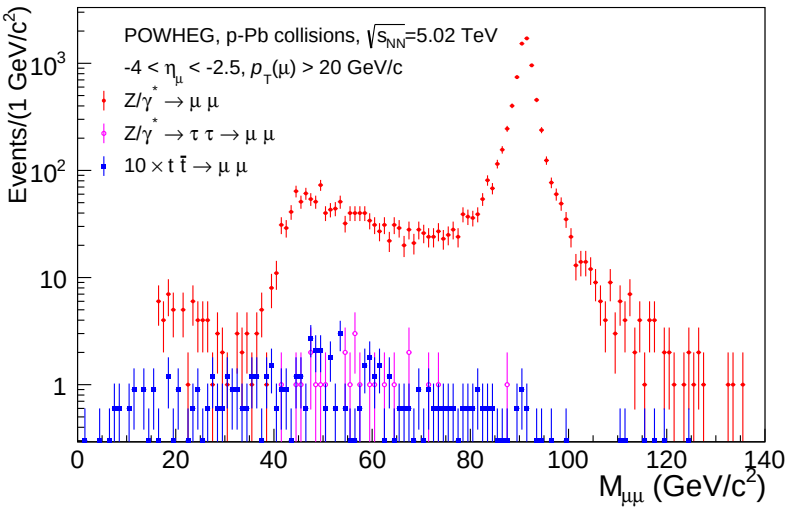

Figure 3.8: Invariant mass distributions of Z-boson decay into two muons along with two background processes. The distributions of the latter two were used to determine the systematic uncertainty of the signal extraction. Figure taken from Ref. [109]

with either offline method. The normalization factor and systematic uncertainty were first calculated per period and the values were shown in Tab. 3.5. After the weighted averaging of the three periods, the largest deviation of 0.5% was kept as the final systematic uncertainty.

3.6.3 Nuclear overlap function

The nuclear overlap function of the Pb–nucleus is obtained from MC Glauber simulations. In the MC Glauber simulations, the Pb-nuclei in the collisions must be modelled. This is done stochastically by the assignment of nucleons within the nuclei where the positions of the nucleons are taken from a nuclear density function. For the latter, a so-called modified Woods-Saxon distribution is used. The distribution contains two parameters: R is the radius parameter, indicating the size of the Pb–nucleus. The other parameter a is the skin thickness, which is a measure for how quick the nuclear density decreases at the edge of the nucleus. The parameter values were obtained from low-energy electron-nucleus experiments. By varying them by one standard deviation from their central values, systematic uncertainties can be obtained on the $\langle T_{\mathrm{AA}} \rangle$ (shown in Tab. 3.6).

3.6.4 Proton–proton cross section

To compute the Z-boson cross section in pp collisions, two energy scales must be set. These are the factorization scale and the renormalization scale. The factorization scale μ_{F} is the scale at which the PDFs are evaluated. At energies lower than μ_{F}, collisions are considered soft (i.e. non-perturbative), while at energies higher than μ_{F}, perturbative calculations allow for the determination of scattering matrix elements. The renormalization scale represents the scale at which ultraviolet divergencies are absorbed by redefining fields. By varying these scales, and the

strong coupling constant, systematic uncertainties of the cross section can be obtained. Additionally, uncertainties in the proton PDFs contribute to the systematic uncertainty of the cross section. The values of the Z-boson cross section and systematic uncertainties have already been shown in Tab. 3.7.

3.6.5 Centrality estimation

The centrality was estimated using the so-called V0M centrality estimator, defined as the sum of the V0A and V0C signals. The underlying framework is based on MC Glauber simulations [133, 136]. For the classification of the centrality percentile, the anchor point (AP) must be determined. This is defined as the V0M amplitude equivalent to 90% centrality. At V0M amplitudes higher than that of the AP, meaning towards more central collisions, the efficiency and purity of hadronic event selection are considered to be 100%. This means that all hadronic interactions are measured and that electromagnetic background are fully rejected. At centrality percentiles below the anchor point (i.e. with centrality above 90%), the efficiency and purity drop, which is why events in that centrality range are typically rejected for analyses. After the anchor point has been determined, the remaining events are assigned centrality percentiles, such that the same number of events are present in every 10% of centrality.

After the anchor point has been determined, the V0M amplitudes that set the centrality percentiles are determined by integrating the measured amplitude distribution normalized by the full integral defined by the anchor point. For example, the V0M amplitude for the top 5% centrality class is determined by the point that satisfies

$$\frac{\int_{V0_{5\%}}^{\infty}(dN_{\mathrm{evt}}/dV)dV}{\int_{V0_{\mathrm{AP}}}^{\infty}(dN_{\mathrm{evt}}/dV)dV} = \frac{1}{18}, \tag{3.14}$$

where dN_{evt}/dV is the amplitude distribution of the V0M.

A systematic uncertainty of 0.5% is assigned to the value of the anchor point [136]. Alternative V0M estimators, with the anchor point shifted by $\pm 0.5\%$ are also available for centrality estimation. A shift in the anchor point changes the assignment of the centrality percentile for a given event. Therefore, in a given centrality interval, the number of Z bosons as well as the number of MB events may change. To first order, the other terms in Eq. 3.1 are not expected to change due to AP variations. Therefore, the relative uncorrected yield (number of candidates per million MB events) was computed for both the anchor point shifted up or down by 0.5%. To prevent any biases, the normalization factor was computed separately for each estimator. The difference in the relative uncorrected yield can be seen in the last column of Tab. 3.8. For comparison, the central values, obtained with V0M, are shown as well. Half of the difference between V0Mplus05 and V0Mminus05 was assigned as the systematic uncertainty for each centrality interval (otherwise the evaluation would be assigned due to a full percent difference in anchor point).

centrality	Z boson		MB (million)		Z / (MB (million))		rel. diff. Z /(MB (million))
	V0M						
0-90%	207		5190.35		0.040 ± 0.003		
0-10%	71		576.37		0.123 ± 0.015		
10-20%	63		576.64		0.109 ± 0.014		
20-90%	73		4037.76		0.018 ± 0.002		
	AP+0.5% versus AP-0.5%						
0-90%	207	207	5157.58	5190.43	0.040 ± 0.003	0.040 ± 0.003	-0.6%
0-10%	70	71	572.72	579.12	0.122 ± 0.015	0.123 ± 0.015	0.3%
10-20%	63	63	573.00	579.39	0.110 ± 0.015	0.109 ± 0.014	-1.1%
20-90%	74	73	4012.37	4032.40	0.018 ± 0.002	0.018 ± 0.002	-1.8%

Table 3.8: Comparison of the V0M estimator with the AP shifted up by 0.5% versus shifted down by 0.5%. The number of candidates, million MB events, their ratio and the relative difference between the ratios are shown. As a reference, the values for the V0M estimator without AP shift are shown as well.

3.6.6 MC - isospin effect on $A\epsilon$

In subsection 3.3.1 it was mentioned that both for the embedding as well as the POWHEG simulations, pp collisions were simulated. However, Pb–Pb collisions also contain contributions from pn (np) and nn collisions. These differ in the content of up and down quarks. In turn, the difference in up and down quark content can lead to a difference of the proton/neutron PDFs. The production cross section in nucleon–nucleon collisions σ_{NN} is the weighted average of all binary collision types, according to

$$d\sigma_{NN} = \frac{Z^2}{A^2}\, d\sigma_{pp} + \frac{(A-Z)^2}{A^2}\, d\sigma_{nn} + \frac{Z(A-Z)}{A^2}\, (d\sigma_{pn} + d\sigma_{np})\,. \tag{3.15}$$

σ_{NN} is the averaged nucleon–nucleon cross section, while σ_{pp}, σ_{pn}, σ_{np} and σ_{nn} represent the cross section in pp, pn, np and nn collisions respectively. For Pb–nuclei, the atomic and mass number are respectively $Z = 82$ and $A = 208$. The change in production cross section σ_{pp} and σ_{NN} due to the difference in up and down quark content is referred to as the isospin effect. For the calculation of the $A\epsilon$, it should be verified what the effect is of only considering pp collisions for the simulations. Using the POWHEG simulations, the $A\epsilon$ was calculated in two separate runs (with differing dipole polarity) for all collision types, and the results are shown in Tab. 3.9. Within uncertainties, for each run all values of the $A\epsilon$ agree. The isospin effect therefore weakly affects the $A\epsilon$ for Z bosons at large rapidity. Therefore, only pp collisions will be considered for its computation in the following.

	pp	pn	np	nn
Run 295788 (LHC18q)	78.77 ± 0.18	78.74 ± 0.17	78.92 ± 0.18	78.74 ± 0.17
Run 296749 (LHC18r)	72.09 ± 0.19	72.43 ± 0.19	72.33 ± 0.20	72.08 ± 0.19

Table 3.9: Comparison of efficiencies in two different runs for different colliding systems. The two runs differ in the polarity configuration of the spectrometer dipole. For the events, POWHEG was used as generator. For this comparison, no smearing was applied on the tracks.

3.6.7 Trigger, tracking and matching efficiencies

For the calculation of the $A\epsilon$, simulations were used. It is therefore vital that the interactions between muons and the spectrometer, known as the detector response, are properly simulated. An important realization here is that it does not matter if the detector response itself is not perfect, as long as the simulations show the same behavior. In this subsection, the systematic uncertainty on the trigger, tracking and matching efficiency in the simulations is discussed. The exact procedure and estimation of the three uncertainties will be presented in separate paragraphs.

Trigger efficiency

The response function of the trigger represents the probability to trigger on a muon with a given p_{T}. It is 0 at very low p_{T} and then sharply increases to a plateau. The response function systematic uncertainty can be divided into two components. The first component is the shape, which depends on the triggering algorithm, the cluster size, the strength of the magnetic field and the alignment of the detector. The second component, which is independent from the first, is the trigger efficiency at the plateau, which depends on the intrinsic chamber efficiency.

The uncertainty on the shape was investigated in another ALICE analysis. The response functions of the data and MC were found to overlap, starting at a transverse momentum of $p_{\mathrm{T}} > 2$ GeV/c. Because the current analysis is done using muons with p_{T} above $20GeV/$c, no uncertainty was attributed due to the shape of the response function.

For the intrinsic chamber efficiency, the uncertainty was determined as follows. From data, a standard chamber efficiency map can be calculated using some general track selection criteria. A modified map is then calculated by varying these criteria, and choosing those that yield the largest difference with respect to the standard map. The $A\epsilon$ was then computed using both the standard as well as the modified efficiency maps. The difference was taken as the uncertainty due to the intrinsic chamber efficiency. For the two data taking periods in 2018, the difference was 1%, while for the 2015 period it was 1.5%. In order to simplify the assignment of the uncertainty, and because the absolute difference is small, an uncertainty of 1.5% was assigned.

Tracking efficiency

A difference in the tracking performance between the simulations and data can be associated to, for example, a high-voltage trip of a detector element. Should such a trip occur half way through a run, a detection element is turned off and this information is then taken into account in the simulation as well. However, in the simulation the detection element will be rejected for the entire run, leading to a difference. However, differences can already arise due to different kinematic distributions of the muons in data and simulations, which is unrelated to the tracking performance of the detector. To prevent biases, dedicated single muon simulations are used which are tuned to reproduce the single muon distributions that are seen in data. To determine the systematic uncertainty due to the tracking efficiency, an iterative procedure is applied to ensure that the generated muon distributions (versus y and p_{T}) agree with the corrected (by the $A\epsilon$) distributions in data. Once satisfactory agreement is reached, the calculations for the tracking efficiency in the simulations is done.

The calculation of the tracking efficiency, which is done both in data and in the simulations, goes as follows. The efficiency per chamber per station is calculated first. Figure 3.9 shows the four ways a muon can interact with a tracking station: a cluster in both chambers, a cluster in either or a cluster in none.

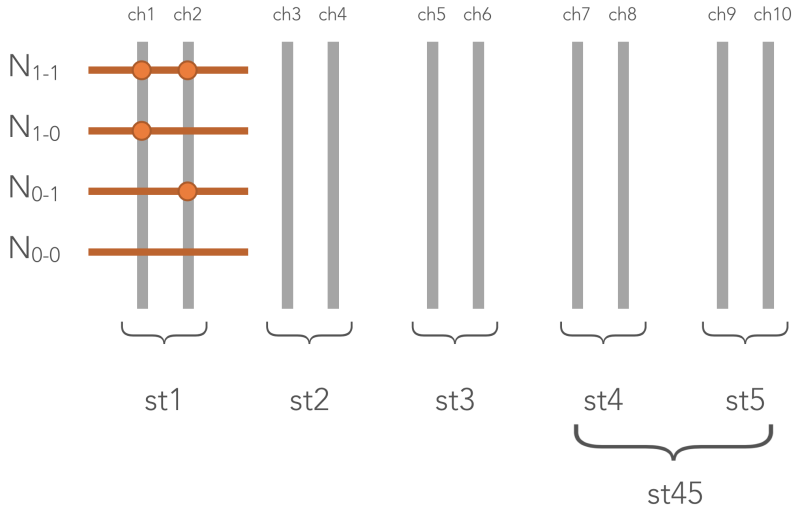

Figure 3.9: Schematic representation of the five tracking chambers. The four possible ways a muon can interact with the first station is shown as well. Figure provided by [137].

The efficiency for chamber i (j) can be calculated as

$$\epsilon_{\mathrm{ch,i}} = \frac{\mathrm{N}_{ij}}{\mathrm{N}_{ij} + \mathrm{N}_{0j}}, \epsilon_{\mathrm{ch,j}} = \frac{\mathrm{N}_{ij}}{\mathrm{N}_{ij} + \mathrm{N}_{i0}} \tag{3.16}$$

where N_{ij} is the number of tracks with reconstructed clusters in both chambers of a station and N_{0j} the number tracks with no reconstructed clusters in chamber i, but with one in chamber j (the other chamber of the same station) and vice versa for N_{i0}. This method relies on the principle that the efficiency for chamber i is independent of that of chamber j, thus removing the need to know the number of tracks with no reconstructed clusters in either chamber (which cannot be extracted in data).

After this, the efficiency per station can be calculated. The calculations per station follow the requirements of the tracking algorithm. The algorithm requires at least 1 cluster in stations 1, 2 and 3 each, so the efficiency for these stations is given by

$$\epsilon_{\mathrm{st,k}} = \epsilon_{\mathrm{ch,i}}\epsilon_{\mathrm{ch,j}} + (1 - \epsilon_{\mathrm{ch,i}})\epsilon_{\mathrm{ch,j}} + (1 - \epsilon_{\mathrm{ch,j}})\epsilon_{\mathrm{ch,i}} \tag{3.17}$$

where i and j indicate the two chambers belonging to station k. On the other hand, at least three hits are required in stations 4 and 5 combined so that their efficiency is computed together as

$$\epsilon_{\mathrm{st,45}} = \prod_{i=7}^{i=10} \epsilon_{\mathrm{ch,i}} + \sum_{i=7}^{i=10} \left((1 - \epsilon_{\mathrm{ch,i}}) \prod_{j=7;j\neq i}^{j=10} \epsilon_{\mathrm{ch,j}} \right). \tag{3.18}$$

The efficiency of the entire detector is then calculated as the product of the four efficiencies detailed above, $\epsilon_{\mathrm{tot}} = \epsilon_{\mathrm{st},1}\epsilon_{\mathrm{st},2}\epsilon_{\mathrm{st},3}\epsilon_{\mathrm{st},45}$. This total efficiency ϵ_{tot} is then calculated on a run-by-run basis and averaged to a single value per period. Finally, the difference between the simulation and the data is taken as a systematic uncertainty in the tracking efficiency. For all three periods, an uncertainty of 1.5% was found for the single muon tracking efficiency. Assuming the efficiency to be uncorrelated for a dimuon, this yields twice the uncertainty, thus giving a 3% uncertainty for the dimuon tracking efficiency.

Trigger-tracking matching

In the analysis, tracks are required to produce clusters in both the tracking as well as the triggering chambers. These clusters are then used to construct corresponding tracking tracks and trigger tracks. To decide whether the two tracks match well enough, a χ^2 value is computed using certain matching criteria. Tracks with a χ^2 higher than a cutoff value are rejected. In order to compute the systematic uncertainty in the simulations due to the matching efficiency, the cutoff value was increased by 50%, which increases the efficiency both in data and in simulations. The difference in this increase between the data and simulations is taken as systematic uncertainty. For single muons, this is 0.5% such that the uncertainty for dimuons is 1%.

3.6.8 MC - smearing

Detector response

One of the main tasks of the MC simulation is modeling the detector response of the interaction between the muons and the chambers. As muons pass through the chambers, an electric signal is induced on the cathode pads. The pads are grouped together to form preclusters, which are fitted with Mathieson functions. From the Mathieson fits, the clusters and their coordinates are extracted, which serve as input for the tracking algorithm. The clusters have a certain spatial resolution, which is driven by the intrinsic detector resolution, the precision of the clusters extraction, and the residual misalignments between the various detection elements.

The resolution of the chambers can be estimated from fits to cluster-track residuals. These are the distance between tracks and the clusters used to reconstruct them. Figure 3.10 shows the resolving power for the y-coordinates per tracking chamber. The lower the value of σ, the smaller the distances that can be differentiated and therefore the higher the resolution. Not only is the resolution overestimated in the simulations, but there is a strong variability in the overestimation per chamber.

A better resolution leads to a higher precision in the momentum estimation, which subsequently leads to narrower reconstructed resonance mass peaks. This means the reconstructed mass peak of the Z is narrower in the simulations than in data. As a result, the $A\epsilon$ is higher due to the inclusion of more reconstructed dimuons in the 60-120 GeV/c^2 interval. In order to get a more realistic description of the detector response, the track parameters were smeared to obtain the same resolution as in the data. This smearing was done by a parametrization of the

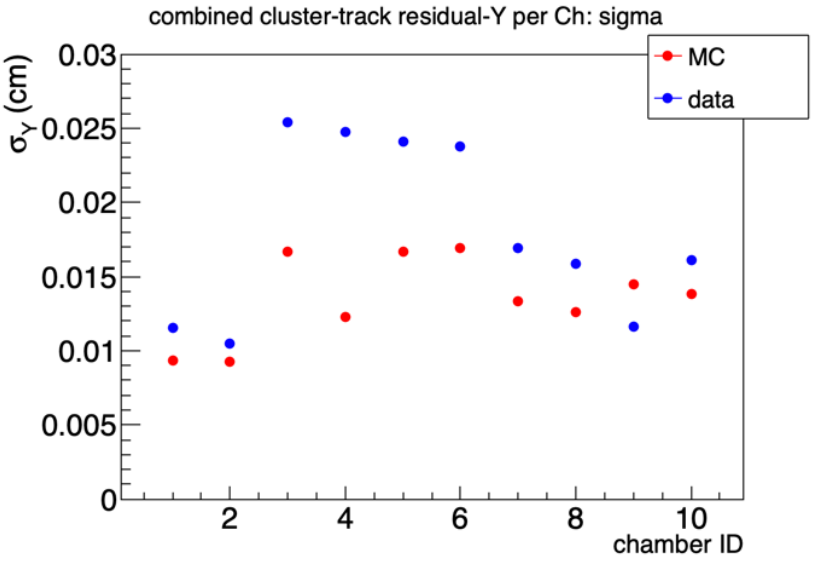

Figure 3.10: Spatial resolution for the y-coordinate per tracking chamber between data and simulations. The simulations generally overestimate the resolution compared to the data. Figure provided by Ref. [138].

cluster resolution obtained by fitting cluster-track residuals. A Crystal Ball function, tuned to data was used as fitting function.

A different parametrization was also tested, tuned to the MC itself. This parametrization was found to yield an invariant mass distribution nearly identical to that of the MC without smearing. Although this may sound trivial, it is an important check for the smearing procedure since it is a parametrization which is supposed to replicate the entire detector response. Figure 3.11 shows the invariant mass spectrum for reconstructed dimuons for the two sets of smearing parametrizations. The data-tuned CB has a wider distribution and larger tails than the MC-tuned one. Because the $A\epsilon$ is calculated specifically over the 60-120 GeV/c^2 interval, this decreases the $A\epsilon$.

The smearing is a simple parametrisation of the full detector response, including interactions with the front absorber and chambers, and also a misalignment of the chambers themselves. Additionally, the smearing does not take into account chamber-by-chamber variations of the resolution which can vary up to a factor 2 (see Fig. 3.10). Due to the many uncertainties related to the smearing, it was decided to adopt a conservative estimate for the systematic uncertainty. The full difference of the $A\epsilon$ values between the two sets (i.e. CB tuned to the data and CB tuned to the MC) was assigned as the systematic uncertainty due to the smearing. The full difference amounts to 5% and is the dominant source of uncertainty in the analysis.

Relative misalignment

For the simulations, alignment files are created from data. From these files, the displacement of subdetectors for the simulation is obtained. However, it was found in the analysis that when inspecting the per-pair p_{T} difference $\Delta p_{\mathrm{T}} = p_{\mathrm{T}\,\mu^+} - p_{\mathrm{T}\,\mu^-}$ of the dimuons, the distributions were centered around different values in the simulations than in data. This was attributed to a remaining relative misalignment of the spectrometer chambers. To take this into

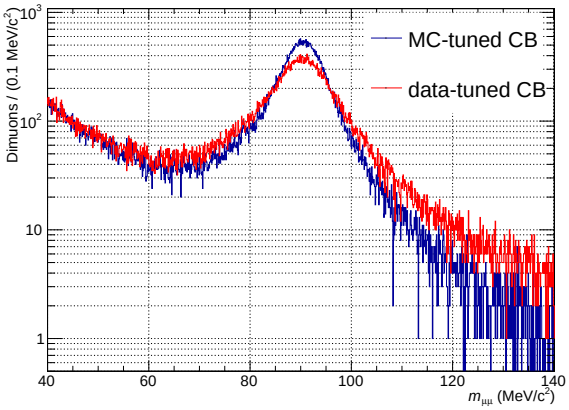

Figure 3.11: Invariant mass distribution of reconstructed dimuons in simulations. A smearing procedure was applied to the muon tracks, using Crystal Ball (CB) functions. The data-tuned CB yields a wider distribution, decreasing the $A\epsilon$.

account, a systematic shift was added to the deviation angle of the tracks during the smearing process explained above. The shift is parametrised by the formula $q \times n \times \sigma_\theta$, where q is the charge of a track σ_θ a value in the smearing task and n a value to be tuned. The sign of the shift was opposite between positively and negatively charged tracks. Some data were taken with the dipole magnet set to positive polarity, others were taken with negative polarity. The sign of the shift was reversed between these configurations. The shift was tuned to reproduce the per-pair p_{T} difference in data for each period. Figure 3.12 shows Δp_{T} as a function of n for the 18q and 18r periods.

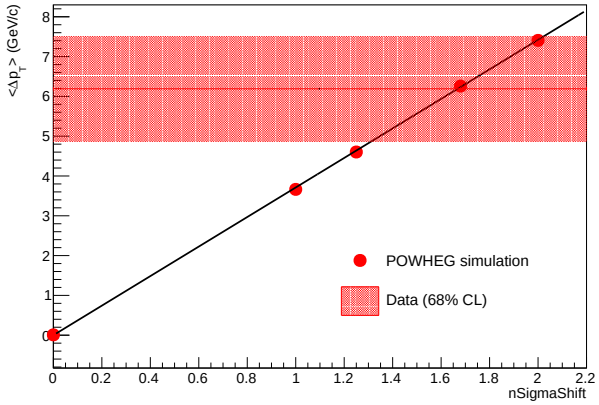

Figure 3.12: Per-pair p_{T} difference as a function of the size of a systematic shift in the deviation angle of tracks. The value in data are shown in the red band, as well as various values for the simulations.

The optimum value (i.e. to be equal to the value in data) of n was established to be 1.68. However, the effect of the tuning of n was found to have a small effect on the $A\epsilon$. For example, the $A\epsilon$ is $(70.43 \pm 0.20)\%$ for $n = 1$, while it is $(70.29 \pm 0.20)\%$ for $n = 2$. Instead, the parametrization of the detector response and subsequent smearing explained above was the dominant source of change of $A\epsilon$ in the simulations.

3.6.9 MC - peak shift

Figure 3.3 shows the invariant mass distribution together with the smeared POWHEG distribution, which was normalized such that the integral over 60-120 GeV/c^2 was equal to that of the data. A slight shift in the peak of the distributions appears to be present. In the data, the average mass in the 60-120 GeV/c^2 interval was 90.6 ± 1.4 GeV/c^2 in 2015 and 87.1 ± 0.9 GeV/c^2 in 2018. In the MC simulations, the average was 88.93 ± 0.02 GeV/c^2 and 88.53 ± 0.01 GeV/c^2 in 2015 and 2018, respectively. The deviation between the data and MC are therefore $1.2\ \sigma$ in 2015 and $1.6\ \sigma$ in 2018. They agree relatively well, which can be attributed to the large statistical uncertainty in the data. Such a shift can influence the $A\epsilon$ as it is calculated specifically over the [60-120] GeV/c^2 interval.

To compute the effect of a shift, a shift in the peak mass of size S was assumed to be present. In this case, the simulated spectrum should be shifted by S before calculating the $A\epsilon$ over the 60-120 GeV/c^2 interval. Note however, that this is mathematically equivalent to integrating the spectrum over the interval $[60 - S, 120 - S]$. In the following, the effect of such a shift in integration will be quantified. In the 15o data set, the peak in data occurs at a lower mass than in the MC, while in 2018 the opposite is true. Therefore, two definitions for S were used, according to

$$S_{\pm} = \mu_{\mathrm{MC}} - \mu_{\mathrm{data}} \pm e_{\mathrm{data}} \tag{3.19}$$

where μ represents the mean over the 60-120 GeV/c^2 interval and e the error on the mean. The integrals were then compared to the number of counts in data. For the 15o period, the maximum difference of 0.4% was observed, while for the 2018 periods, this difference was 0.9%. However, due to the conservative estimate of 5% already taken into account due to the smearing of the tracks (which can also influence the peak mass), no further systematic uncertainty for a potential peak shift was assigned.

3.6.10 Summary

To conclude this chapter, Tab. 3.10 shows a summary of all the systematic uncertainties present in the analysis. Symbols are used to indicate whether an uncertainty is correlated versus centrality and/or rapidity. A correlation of an uncertainty versus a quantity means that all data points will tend to fluctuate collectively up or down with respect to their central values. This is in contrast with statistical or uncorrelated systematic uncertainties, where fluctuations around the central values will occur randomly between different data points.

source of systematic	effect [%]
Track smearing ■	5
pp cross-section ■	3.5-5.0
Tracking efficiency ■	3
Trigger efficiency ■	1.5
Matching efficiency ■	1
Normalization factor ■ ★	0.5
Centrality estimation ★	0.2 - 0.9
$\langle T_{AA} \rangle$ ★	0.7 - 1.5
Background contribution	1

Table 3.10: Systematics. Values expressed as percentage. The symbol ■ (★) indicates that the systematic is correlated versus centrality (rapidity).

Chapter 4

Z boson: results

The normalized invariant yield and nuclear modification factor, introduced in Chap. 3, are presented for the Z boson in this chapter. The normalized invariant yield quantifies the production, and will be shown integrated over centrality and rapidity, as well as a function of each. The nuclear modification factor quantifies deviations between the production in Pb–Pb collisions and pp collisions, and will be shown as a function of rapidity and centrality. The results presented in this chapter were obtained during this thesis and have been published in the Journal of High Energy Physics [93].

The data will be compared with various theoretical predictions. Before discussing the results, a brief outline of the theoretical models is given.

4.1 (nuclear) parton distribution functions

To obtain the theoretical values of the cross sections and invariant yields, the following was done. Simulation codes that compute partonic cross sections were interfaced with (n)PDF sets (presented in subsection 1.3.1.1) for partonic distributions. Two such codes were used: Monte Carlo for Femtobarn processes (MCFM) [139] and Fully Exclusive W and Z (FEWZ) [140]. The two codes are now detailed separately.

The MCFM code computes cross sections at NLO order and was coupled with the CT14NLO PDF set. From the CT14NLO PDF set, the proton–proton cross section was computed. The invariant yield and nuclear modification factor were also computed, but for these the isospin content of the Pb–nuclei was taken into account. However, no nuclear modifications to the PDFs were considered. To include nuclear modifications, the EPS09 and EPPS16 nPDF sets were used. EPPS16 exclusively provides values integrated over the whole nucleus, meaning no impact parameter (centrality) dependence is taken into account in the nuclear modifications. In contrast, EPS09s takes into account a spatial dependence of the nPDFs and therefore is able to provide centrality dependent predictions.

The other code that was used is the FEWZ code which contains NNLO QCD computations. Although it is in

principle possible to obtain values of the proton–proton cross section, invariant yield and nuclear modification factor for free-nucleon PDFs from FEWZ as well (in addition to the ones obtained from the MCFM code), they were not computed. Instead, only nPDF computations were done, coupling the FEWZ code with NCTEQ15 nPDFs. As was the case for EPPS16, the NCTEQ15 values are computed integrated over the entire Pb–nucleus.

4.2 Invariant yield

The invariant yield, integrated over the centrality interval 0-90% and rapidity interval $2.5 < y^{\mu\mu}_{\rm cms} < 4.0$, is shown in Fig. 4.1. A previously published measurement from ALICE, with a subsample of the current dataset is also shown [95]. The publication pertains to an earlier analysis done on only the 2015 dataset. As expected, the inclusion of the 2018 data in the current analysis decreases the statistical uncertainty of the measurement. The systematic uncertainty has slightly increased with respect to the previous measurement. More specifically, the increase comes from a difference in the evaluation of the systematic uncertainty originating from the $A\epsilon$ correction. In the current analysis, the procedure to obtain the uncertainty was re-evaluated and a more conservative method was adopted. The current method yields a systematic uncertainty of 5% for the $A\epsilon$ correction, while a value of 3.5% was assigned in the earlier publication.

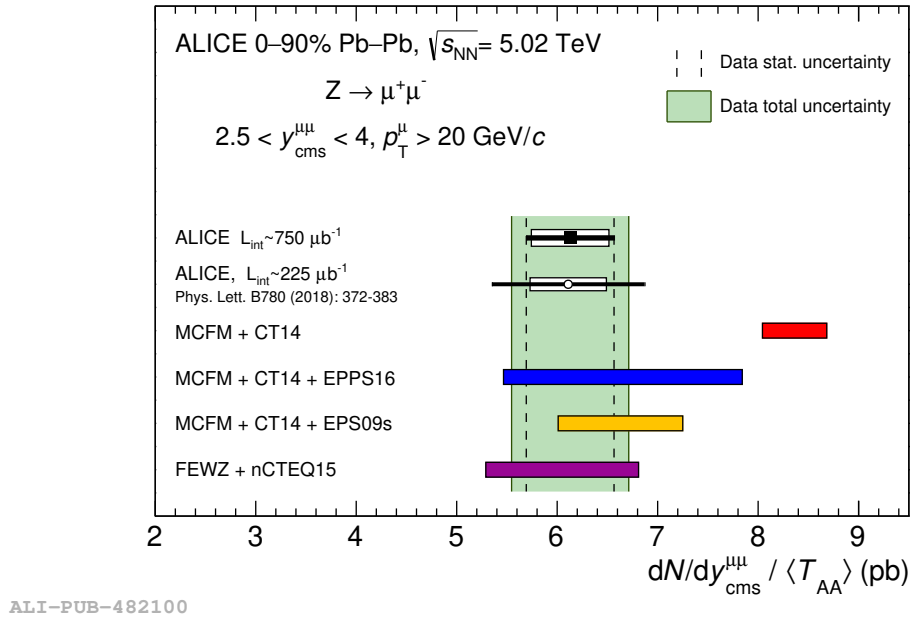

Figure 4.1: Normalized invariant yield integrated over centrality and rapidity. The measured value is shown along a previous measurement done over part of the current data sample. For both measurements, lines indicate the statistical uncertainty while boxes indicate the systematic uncertainty. The green shaded area displays the total uncertainty of the measurement. Several theoretical computations are shown as well, some of which include nuclear modifications to PDFs [63, 64, 70, 71, 139, 140]. Figure taken from [93].

In addition to the measurement itself, Fig. 4.1 shows the predictions from various theoretical models. In general, there is better agreement between the data and nPDF models than with the free-nucleon model. The nPDF models have larger theoretical uncertainties because of the convolution of uncertainties in the nuclear modifications on top of uncertainties in the modeling of the proton (and neutron) PDFs themselves. The EPPS16 calculations contain a larger uncertainty than the NCTEQ15 and EPS09s models, due to the inclusion of more free parameters in the model.

The EPPS16 and NCTEQ15 models only provide predictions integrated over the Pb–nucleus, i.e. over the centrality interval of 0-100%. In contrast, the measurement was done over the 0-90% centrality interval. However, because the production of Z bosons scales with the number of binary collisions (as will be shown later), the majority of Z bosons are produced in central events. The stability of the measurement was tested by estimating the yield in the 90-100% interval, and using it to compute the yield in the 0-100% interval. The estimation of the yield in the 90-100% interval was done in two ways. The first was to apply binary collision scaling to the yield in 0-90% interval. This results in a yield in the 0-100% interval that is exactly equal to that in 0-90% by definition of binary scaling. The second method to estimate the yield in the 90-100% interval was to assume the value given by the CT14NLO predictions without nuclear modifications. From Fig. 4.1, it can be seen that the CT14NLO value overpredicts the data, so the estimation obtained from this method provides an upper limit of the yield in the 90-100% interval. The yield in the 0-100% interval was then computed from the yields in the 0-90% and 90-100% intervals, under the assumption of binary scaling. The difference in normalized yields of the 0-100% interval between the two methods is 2 per mille. This means that although the extrapolation of the normalized invariant yield from 0-90% to 0-100% depends on the modeling of the yield in 90-100%, the uncertainty due to the modeling is more than covered by the systematic uncertainty of the measurement. In summary, the measurement can be regarded as a measurement integrated over the full Pb–nucleus.

Figure 4.1 shows that the CT14NLO computations overestimate the data and this can be understood as follows. The spectrometer is located away from the interaction point, at forward rapidity. This means that only Z bosons with large longitudinal momentum will decay in the acceptance of the spectrometer. In collisions of partons with equal bjorken-x, the net longitudinal momentum of the Z boson is 0, and subsequently no muon pair at large y is produced. To create a Z boson with large longitudinal momentum, a asymmetry between the x values of the two colliding partons is necessary. Therefore, the Z bosons that decay in the spectrometer originate from collisions between low-x and high-x partons. A leading order estimate of the bjorken-x values necessary to create a Z boson at rapidity y is given by

$$x_{1,2} = \frac{M_Z}{\sqrt{s_{\mathrm{NN}}}} e^{\pm y}, \tag{4.1}$$

where $x_{1,2}$ are the bjorken-x values of the two participating partons, M_Z the Z-boson mass, $\sqrt{s_{\mathrm{NN}}}$ the center-of-mass (cms) energy per nucleon pair and y the rapidity in the cms frame [141]. For symmetric collision systems

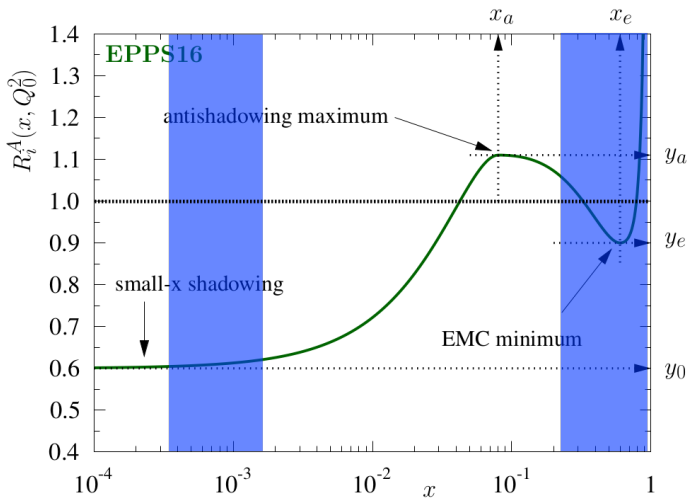

Figure 4.2: Nuclear modifications as a function of bjorken-x. The two blue bands indicate the bjorken-x probed simultaneously in Pb–Pb collisions at $\sqrt{s_{\mathrm{NN}}} = 5.02\,\mathrm{TeV}$ at $2.5 < y < 4.0$ at ALICE. Figure adapted from [63].

(such as pp or Pb–Pb), the cms rapidity is equal to the rapidity measured in the laboratory frame. From Eq. 4.1, it follows that the bjorken-x values probed in the measurement are $x_1 = [3.3 \cdot 10^{-4}, 1.5 \cdot 10^{-3}]$ and $x_2 = [0.22, 0.99]$. At low x (< 0.05), nPDFs predict shadowing, meaning that there is a depletion of partons in nuclei compared to free nucleons. At high x, several competing effects are present. These are a surplus in the antishadowing region at $0.05 < x < 0.3$ and a depletion in the EMC region at $0.3 < x < 0.9$. At x, $0.9 < x < 1$, some nPDF models include the Fermi region in which another surplus is expected, although uncertainties in this regime are large and not all nPDF models predict this region. Figure 4.2 shows the nPDF effects described along with the bjorken-x probed in the Pb–Pb collisions. It should be noted that the given values of x for the transitions between the different nuclear effects are only a rough estimate. In reality, the exact values depend on the nPDF uncertainties, parton flavor and scale of the hard process Q. Nevertheless, the convolution of shadowing at low x and the EMC effect at high x can explain the decrease in the data compared to the CT14NLO-only computations.

In order to quantify the difference between the CT14NLO-only computations, the deviation between the measured and predicted yield was calculated as

$$\frac{|Y_{\mathrm{data}} - Y_{\mathrm{theory}}|}{\sqrt{\sigma^2_{\mathrm{data,stat}} + \sigma^2_{\mathrm{data,syst}} + \sigma^2_{\mathrm{theory}}}}, \tag{4.2}$$

where Y represents the yield and σ a given uncertainty. With this equation, the CT14NLO-only computations of the integrated invariant yield are calculated to deviate $3.4\ \sigma$ from the measured value. The larger data set allows for a measurement with higher precision compared to the previous publication, in which a deviation of $2.3\ \sigma$ was found [95]. In the remainder of the chapter, the deviation will also be given for differential quantities, which contain correlated and uncorrelated systematic uncertainties. For these, the correlated and uncorrelated systematic

uncertainties were added in quadrature separately so that $\sigma^2_{\text{data,syst}} = \sigma^2_{\text{data,corr syst}} + \sigma^2_{\text{data,uncorr syst}}$.

4.2.1 Differential yields

The data set was large enough to allow for the measurements of differential yields. In this subsection, the normalized invariant yield will be presented as a function of centrality and of rapidity. The rapidity differential yields were integrated versus centrality, and vice versa.

Versus rapidity

Figure 4.3 (left) shows the rapidity distribution of the normalized invariant yield. The measured yields are presented alongside CT14NLO-only and EPPS16 nPDF calculations. The EPPS16 predictions are in agreement with the data in all rapidity intervals. The free-nucleon predictions agree with the yield in the $2.50 < y^{\mu\mu}_{\text{cms}} < 2.75$ rapidity interval. However, at larger rapidities a discrepancy arises between the yield and free-nucleon predictions, as the free-nucleon predictions overestimate the data. This is expected, as at more forward rapidities, smaller values of x are probed, leading to a stronger shadowing effect. The largest difference is found at $3.25 < y^{\mu\mu}_{\text{cms}} < 4.00$, where the deviation is $3.3\ \sigma$. The deviation found is larger than in the earlier analysis with a subset of the current data, where a maximum deviation of $2\ \sigma$ was seen in the $3.00 < y^{\mu\mu}_{\text{cms}} < 4.00$ rapidity bin [95].

Versus centrality

In Fig. 4.3 (right), the centrality dependence of the normalized invariant yield is shown. The CT14NLO-only predictions are shown as a horizontal band. The reason for this is that they are computed for nucleon–nucleon collisions. Because centrality is not defined at the nucleon scale, but rather at the nucleus scale, the predictions contain no centrality dependence and are the same for each centrality interval. The EPS09s model is the only one of the three nPDF models provided that includes an impact parameter dependence and is therefore shown in the figure as well. The EPS09s predictions are generally in good agreement with the data, although a slight tension is present in the 0-10% centrality interval. The free-nucleon predictions overestimate the data, showing a maximum deviation of $3.9\ \sigma$ in the 0-10% centrality interval. This deviation is larger than the $2.6\ \sigma$ deviation observed in the 0-20% centrality bin in the previous analysis.

The EPS09s predictions show a monotonic increase from the 0-10% to 20-90% interval and the relative difference between the two intervals is 4.1%. On the other hand, the data show an increase from $0 - 10\%$ to $10 - 20\%$ centrality, but a decrease from $10 - 20\%$ to $20 - 90\%$, hinting at the measurement of fluctuations around a common value.

The observations are in agreement with the expectation that the invariant yield of colorless hard probes (such as the Z boson) depends on the number of binary collisions $\langle N_{\text{coll}} \rangle$. Because the $\langle T_{\text{AA}} \rangle$ normalizes the yield with respect to the number of binary nucleon–nucleon collisions per centrality interval, it should be flat as a function of centrality and this is what is observed. This supports the earlier assumption of binary collision scaling for the

extrapolation of the results to 0-100% centrality.

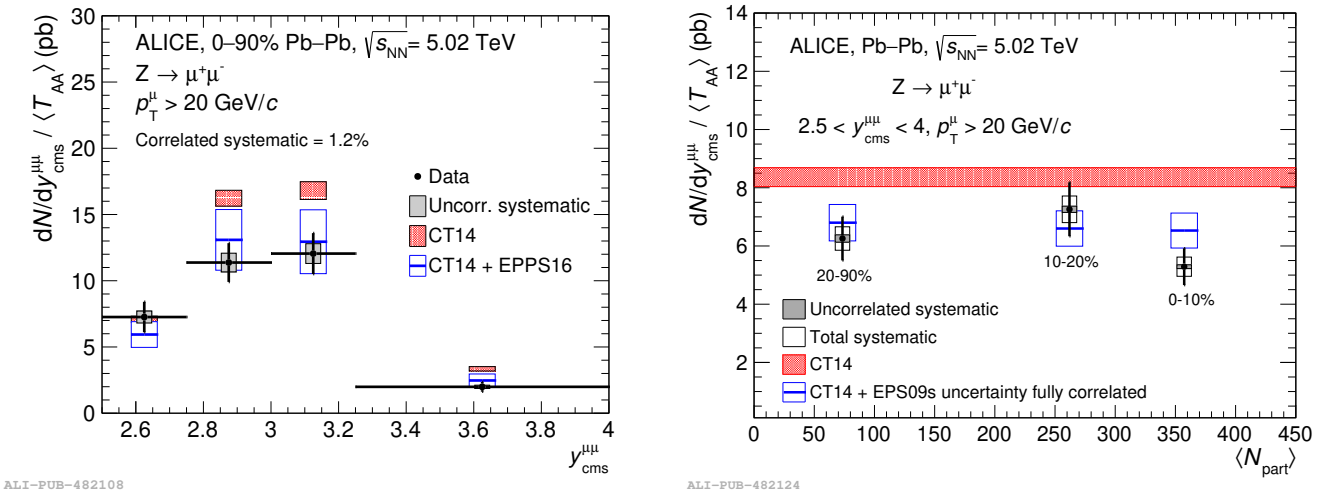

Figure 4.3: Normalized invariant yield, shown as a function of rapidity (left) and centrality (right). Statistical uncertainties are shown as lines, while systematic uncertainties are represented by boxes. Although not specified in the plot legends, CT14 refers to CT14NLO computations. Figure taken from [93].

4.3 Nuclear modification factor

The nuclear modification factor R_{AA} is used to quantify medium effects in heavy-ion collisions. In principle, a measurement of the Z-boson proton–proton cross section should be used for the calculation of the R_{AA} (see Eq. 3.2). However, the integrated luminosity in pp collisions at $\sqrt{s} = 5.02\,\mathrm{TeV}$ in ALICE is not large enough to allow for such a measurement at forward rapidity. Instead, a theoretical value of the cross section was used, obtained from the MCFM code interfaced with the CT14NLO PDFs. An R_{AA} value of 1 typically indicates that there are no dominant medium effects (or alternatively that there are competing effects that cancel each other). This would imply that heavy-ion collisions can be described as a superposition of independent nucleon–nucleon collisions. However for the production of electroweak bosons, the R_{AA} must be interpreted with more caution. The reason for this is that the R_{AA} is obtained by dividing the invariant yield by specifically the proton–proton cross section. However, contributions from neutrons (isospin) can cause the R_{AA} to deviate from unity even without taking into account nPDF modifications.

Versus rapidity

The R_{AA} as a function of rapidity is shown in Fig. 4.4 (left), alongside the CT14NLO-only (including isospin) and EPPS16 predictions. There is no uncertainty on the values of the free-nucleon predictions, because the proton PDF uncertainties cancel out in the ratio of the nucleon-nucleon cross section over the proton–proton cross section. The deviation from unity due to isospin is of the order of $+5\%$. At $2 < y^{\mu\mu}_{\mathrm{cms}} < 2.75$, the data is well described by both

the CT14NLO-only as well as the EPPS16 predictions. On the other hand, at $2.75 < y^{\mu\mu}_{\mathrm{cms}} < 4$, the data are in agreement with EPPS16 but differ from the CT14NLO-only predictions. As is the case for the invariant yield, the difference between the free-nucleon PDFs and nPDFs grows towards larger rapidities. The deviation between the measured R_{AA} and the CT14NLO-only computation is largest in the rapidity interval $3.25 < y^{\mu\mu}_{\mathrm{cms}} < 4.00$, where it amounts to $3.3\ \sigma$. This deviation is the same as the deviation in the differential invariant yield versus rapidity, because the addition of the uncertainty of the pp cross section in the data compensates for the loss of of theoretical uncertainty.

Versus centrality

Figure 4.4 (right) shows the R_{AA} as a function of centrality. Alongside the data, CT14NLO-only and CT14NLO+EPPS16 predictions are shown. For both theory models, no impact parameter dependence is included in the model, which is why the predictions are shown as bands. The CT14NLO-only computations overpredict the measured R_{AA}, which is below unity for all three data points. The CT14NLO+EPPS16 predictions, on the other hand, are in agreement with the data.

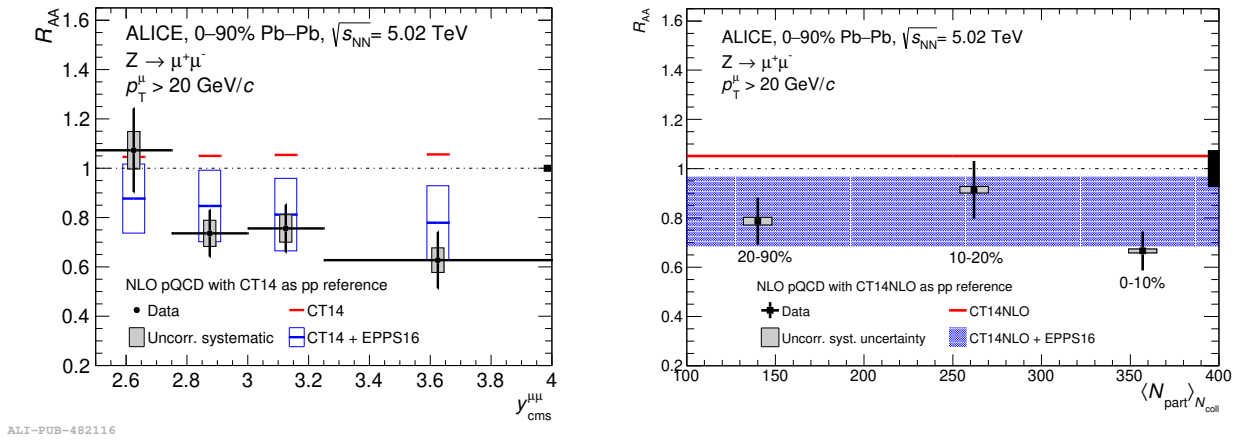

Figure 4.4: Nuclear modification factor R_{AA} as a function of rapidity (left) and centrality (right). Statistical uncertainties are shown as lines, while correlated systematic uncertainties are represented by boxes. The uncorrelated systematic uncertainty of 1.2% (7.3%) versus rapidity (centrality) is shown in black on the right axis. The CT14NLO predictions deviate from unity even without nuclear modifications due to isospin. Left figure taken from [93], while right figure was created for this thesis.

4.4 Comparison

In this section, the results obtained in this thesis are compared to other EW measurements done at the LHC for Pb–Pb collisions at $\sqrt{s_{\mathrm{NN}}} = 5.02\,\mathrm{TeV}$. The results will first be compared as a function of rapidity, then as a function of centrality.

At ATLAS, the production of W and Z bosons has been studied [142, 143]. For the W bosons, the electron and muon decay channels were measured in the kinematic regime defined by ${p_{\mathrm{T}}}^{\ell} > 25$ GeV/c, $|\eta^{\ell}_{cms}| < 2.5$, ${p_{\mathrm{T}}}^{\nu} > 25$ GeV/c, $m_{\mathrm{T}} > 40$ GeV/c. Here, ℓ stands for the lepton, ν for the (anti)neutrino and $m_{\mathrm{T}} > 40$ represents the transverse mass of the lepton and neutrino system. A measurement of Z bosons was also done, in the kinematic regime of ${p_{\mathrm{T}}}^{\ell} > 20$ GeV/c, $|\eta^{\ell}_{cms}| < 2.5$ and dilepton mass $66 < m_{\ell\ell} < 116$ GeV/c^2. For both the W and Z bosons, the electron and muon decay channels were combined, and the normalized invariant yield and R_{AA} versus centrality and rapidity were measured. At CMS, Z bosons were measured in the electron and muon decay channels in the kinematic regime $|\eta^{\ell}_{cms}| < 2.4$ (2.1) for muons (electrons), ${p_{\mathrm{T}}}^{\ell} > 20$ GeV/c, $60 < m_{\ell\ell} < 120$ GeV/c^2 and $|y^{\ell\ell}_{\mathrm{cms}}| < 2.1$ [144]. The decay channels were combined and the production cross section as a function of rapidity and the normalized invariant yield versus centrality were measured.

Production versus rapidity

Both the ATLAS and CMS data were measured at midrapidity, whereas the ALICE data were measured at forward rapidity. Nuclear effects are generally more pronounced at forward rapidity and the data show that free-nucleon PDFs and nPDF predictions at midrapidity are closer to each other than at forward rapidity. In both the ATLAS and CMS data, the difference between free-nucleon and nPDF predictions grows at larger rapidity. Figure 4.5 shows that a light preference for free-nucleon computations is present in the ATLAS W and Z boson measurements as well as the CMS Z boson measurement. Also at both experiments, both the free-nucleon and nPDF predictions consistently underestimate the data. In the ATLAS Z-boson measurement, the models underpredict the data by $1-3$ deviations, where the larger deviations are found at forward rapidities [143]. The production of W bosons is underestimated by $2-3\%$ by the CT14NLO-only computations [142]. However, the authors of [142] note that already in pp collisions at $\sqrt{s} = 5.02\,\mathrm{TeV}$, the CT14NLO-only predictions underestimate the W data by roughly $1\,\sigma$ [91]. The CMS Z-boson data lie on the upper edge of the CT14NLO-only predictions. In contrast to the ATLAS measurements, data from pp collisions at $\sqrt{s} = 13\,\mathrm{TeV}$ are well described by CT14NLO-only predictions within theoretical uncertainties [145].

A direct comparison of the yields at different experiments cannot be made due to the different kinematic regimes in which the measurements were performed. Instead, Fig. 4.6 shows the ratio of the data divided by the CT14NLO-only predictions as a function of rapidity. It should be noted that at ATLAS and ALICE, the normalised invariant yield was measured, while at CMS the cross section was measured. At midrapidity both CMS and ATLAS data are systematically above the CT14NLO-only predictions. Both experiments show a light preference for the CT14NLO-only predictions over EPPS16 nPDF predictions. At forward rapidity, the shadowing and EMC effects become more

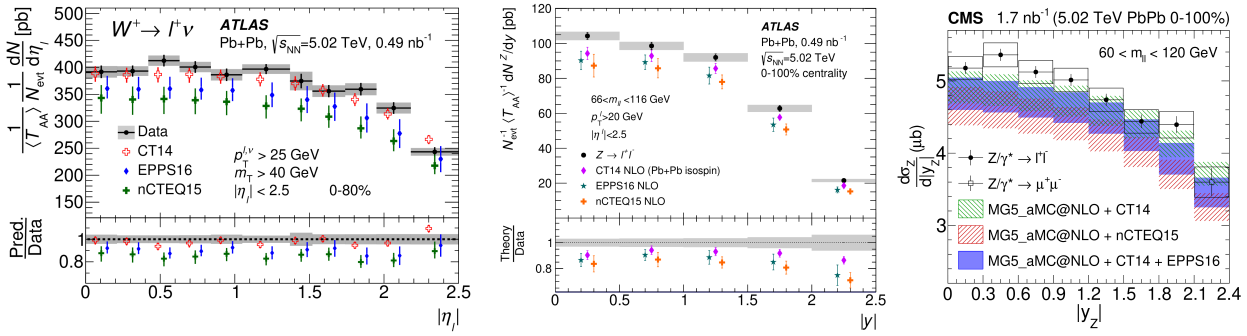

Figure 4.5: Production of electroweak bosons in Pb–Pb collisions at $\sqrt{s_{\mathrm{NN}}} = 5.02\,\mathrm{TeV}$ as a function of (pseudo)rapidity. The left and middle plot show respectively the normalized invariant yield of W^+ bosons and Z bosons measured in ATLAS. The right plot shows the production cross section of Z bosons measured in CMS. Figures taken from Refs. [142–144].

prominent and in the ALICE measurements the ratio falls below unity indicating that the CT14NLO-only predictions overestimate the data. The ALICE data show a strong preference for the EPPS16 nPDF predictions.

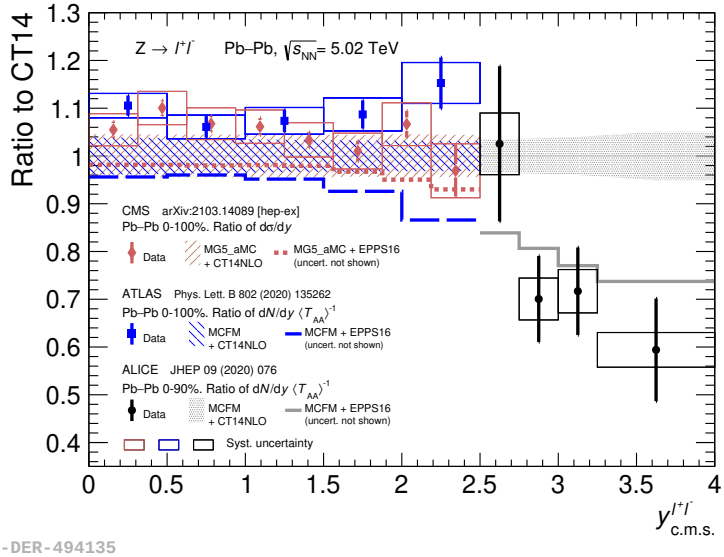

Figure 4.6: Comparison of the ratio of normalized invariant yield (for ATLAS and ALICE) or cross section (for CMS) in Pb–Pb collisions at $\sqrt{s_{\mathrm{NN}}} = 5.02\,\mathrm{TeV}$ to free-nucleon predictions made with CT14NLO PDFs as a function of rapidity [93, 142–144]. Plot provided by [146].

Production versus centrality

In the ATLAS measurements, the R_{AA} of the W and Z bosons are consistent with a constant value, although for all three bosons, a light increase in R_{AA} towards peripheral collisions is seen in Fig. 4.7 (left). The CMS data on Fig. 4.7 (right) show the normalized invariant yield as a function of centrality, rather than the R_{AA}. However, the conversion to R_{AA} is done by dividing the normalized invariant yield by the pp cross section which is the same for all centrality bins. The rescaling of the y-axis on the plot will therefore have no effect on the trend of the data. In the CMS data, a decrease is seen in the normalized invariant yield in peripheral collisions. This observation seems to

be in conflict with the trend of the ATLAS measurements. Earlier measurements of W and Z bosons by both ATLAS and CMS were not sensitive enough to such changes in the production as a function of centrality, because the data were less precise (especially in the peripheral events) [144].

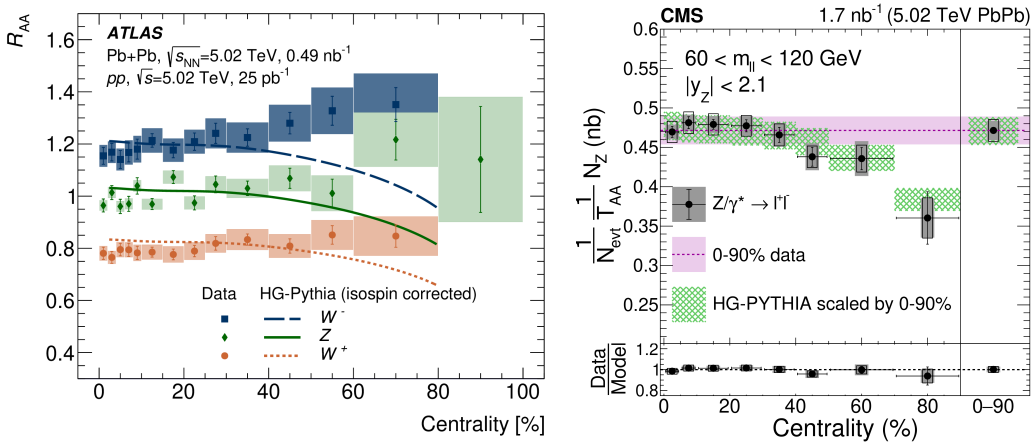

Figure 4.7: Measurement of electroweak bosons as a function of rapidity in ATLAS (left) and CMS (right). The ATLAS values shown are of the R_{AA}, while the CMS values are of the normalized invariant yield. The explanation of the HG-PYTHIA model is proved in the text. Figures taken from Refs. [143, 144].

An ALICE analysis of the R_{AA} of charged particles in Pb–Pb collisions at $\sqrt{s_{\mathrm{NN}}} = 5.02\,\mathrm{TeV}$ as a function of centrality showed that the R_{AA} in peripheral collisions (above 80%) was below unity. This was attributed to biases originating from collision geometry and criteria for event selection. These biases lead to an apparent suppression in peripheral events. A modified version of PYTHIA, called HG-PYTHIA was created in which the collision geometry and event selection biases are included [147]. Both plots in Figure 4.7 show predictions using the HG-PYTHIA simulations. The trend of decreasing normalized invariant yield in peripheral events in CMS data is in agreement with values from the HG-PYTHIA model. On the other hand, in ATLAS no such decrease is observed, and the data are in contrast with the values from HG-PYTHIA.

An explanation for the apparent increase of the ATLAS data was proposed in Ref. [148]. For the computation of centrality dependent quantities, the nuclear overlap $\langle T_{\mathrm{AA}} \rangle$ is necessary, which is obtained from Glauber MCs. One of the inputs for the Glauber MC is the inelastic nucleon–nucleon cross section $\sigma_{\mathrm{nn}}^{\mathrm{inel}}$. The authors note that the $\sigma_{\mathrm{nn}}^{\mathrm{inel}}$ is generally obtained from extrapolations of proton–proton data. They suggest that in heavy-ion collisions, shadowing effects might lead to a lower value of $\sigma_{\mathrm{nn}}^{\mathrm{inel}}$. By equating the theoretical and experimental formulae of the R_{AA}, a different value of $\sigma_{\mathrm{nn}}^{\mathrm{inel}}$ can be extracted. Instead of the commonly used value of 70 mb, a value of $41.5^{+16.2}_{-12.0}$ mb is found. With this lower value, the $\langle T_{\mathrm{AA}} \rangle$ can be recomputed as well as the centrality dependence of the W and Z production. With the new $\langle T_{\mathrm{AA}} \rangle$ values, the increasing trend towards peripheral collisions vanishes and the EW production measured in ATLAS becomes flat as a function of centrality. However, it should be noted that in the CMS data, no discrepancies with the Glauber MC are observed, and therefore do not require a shadowed inelastic cross section to describe the data. In the analysis done in this thesis, the R_{AA} as a function of centrality is consistent

with a constant value that is slightly below unity (see Fig. 4.4-right). Due to limited luminosity, the most peripheral centrality bin is the $20 - 90\%$ centrality bin. This prevents any conclusive statement on a possible enhancement or decrease of the normalized invariant yield above 50% centrality, where the decrease becomes visible in the CMS data.

Chapter 5

Z boson: LHC Run 3 projections

For the LHC Run 3 data taking period, special runs involving oxygen nuclei instead of lead nuclei have been proposed. The purpose of these special runs would be to complement existing data from Pb and Xe collisions. In this chapter, their relevance for measurements of Z-boson production for nPDF studies is discussed.

The LHC has provided numerous data points involving Pb–nuclei that can be included in nPDF fits. However, there are few data at high energy with nuclei other than Pb. As a result, the A-dependence (atomic mass number) of nPDFs is not well understood. This creates a need for measurements at high energy with $A << 208$. The isotope considered for the oxygen runs is $^{16}\mathrm{O}^{8+}$. Therefore, data from p–O and O–O collisions would be well suited to shed light on this A-dependence.

This chapter will detail the projections of Z-boson production in p–O and O–O collisions in LHC Run 3 in order to determine whether measurements might be feasible.

5.1 p–O and O–O data taking configurations

At the time of writing, the specific collision energies and configurations have not yet been finalized. Several configurations are being considered, which will be discussed here. The final configurations will be decided based on accelerator capabilities, time constraints (only a certain number of days are allotted for the oxygen data taking) and physical motivations (such as having a pp baseline already at $\sqrt{s} = 7\,\mathrm{TeV}$). The oxygen runs are planned to take place after a period of Pb–Pb runs at $\sqrt{s_{\mathrm{NN}}} = 5.02\,\mathrm{TeV}$. If the beam optics remain the same during the oxygen data taking, the corresponding center of mass energy per nucleon pair will be $\sqrt{s_{\mathrm{NN}}} = 9\,\mathrm{TeV}$ in p–O collisions and $\sqrt{s_{\mathrm{NN}}} = 6.37\,\mathrm{TeV}$ in O–O collisions. To facilitate a more direct comparison between Pb–Pb data taken at $\sqrt{s_{\mathrm{NN}}} = 5.02\,\mathrm{TeV}$, the possibility of O–O collisions at the same energy is under consideration. However, this would require two additional days of setup time and is currently not the preferred configuration. In contrast to p–Pb collisions, where data taking generally occurs both in proton–going (forward) and Pb–going (backward) directions,

only proton–going collisions are considered for the p–O collisions.

The expected integrated luminosity for the p–O collisions is 5 nb^{-1}, while it is 1 nb^{-1} for the O–O collisions (ranging from 0.5 to 4 nb^{-1}).

5.2 Extrapolation method

The projections were obtained by extrapolating existing measurements of the Z-boson pp cross section. In pp collisions, there is no measurement at forward rapidity in ALICE due to limited luminosity. Therefore, an LHCb measurement at $\sqrt{s} = 7\,\mathrm{TeV}$ was taken instead [149]. Alternatively, a pp cross section can be approximated from a measured p–Pb cross section using $\mathrm{A} \times \sigma_{\mathrm{pp}} = \sigma_{\mathrm{pA}}$. For this, an ALICE measurement from p–Pb collisions at $\sqrt{s_{\mathrm{NN}}} = 8.16\,\mathrm{TeV}$ was used [93]. The formula used to calculate the projected measured yield is

$$N^{\mathrm{config}} = \mathcal{L}(A\epsilon)\ \sigma_Z^{\mathrm{config}} = \mathcal{L}(A\epsilon)\ A_1 A_2\ \sigma_Z^{pp}\ C_{\mathrm{acc}} C_{\mathrm{energy}}, \tag{5.1}$$

where the superscript config refers to the configuration of the measurement. This includes the collision system (p–O or O–O), center-of-mass energy and rapidity (either forward or backward). $\mathcal{L}$ represents the integrated luminosity, while $A\epsilon$ is the detector reconstruction and selection efficiency, and A_1 and A_2 refer to the mass numbers of the colliding hadrons. Lastly, the pp cross section is corrected for differences in acceptance and energy between the measurement and the projection configuration. These corrections are given by C_{acc} and C_{energy} respectively. They were obtained with PYTHIA simulations and are detailed in the remainder of this section.

5.2.1 Acceptance and energy corrections

5.2.1.1 PYTHIA setup

Existing measurements were extrapolated to obtain the projections in p–O and O–O collisions. However, Z-boson production depends on the collision energy and system as well as detector acceptance and kinematic selections. Corrections were therefore applied to accommodate for this dependence. The corrections were obtained with PYTHIA 6.4 simulations, in which Z bosons were generated and subsequently forced to decay into dimuons [131]. Per event, one Z boson was generated and for each configuration 50000 events were simulated. The Z bosons were generated with a rapidity $-12 < y < 12$. In order to compute the acceptance corrections between different fiducial rapidity ranges, no kinematic selections were applied on the decay muons at the generated level.

Isospin was taken into account in the simulations by simulating separately pp, pn, np and nn collisions. Depending on the collision configuration (p–O or O–O), different contributions of binary collisions were considered. Also, in configurations involving nuclei, nuclear modifications of PDFs were included. For example, for pp simulations in

p–O configuration the parton from one proton is sampled from a free-proton PDF, while the parton from the other proton is sampled from a nuclear PDF of oxygen. Additionally, in asymmetric collisions, the center-of-mass frame was boosted according to $\Delta y = 0.5 \ln\left(\frac{Z_1 A_2}{Z_2 A_1}\right)$ where Z and A represent respectively the atomic and mass number of the colliding hadrons. The rapidity boost introduces a global shift of the rapidity distribution, while isospin and nuclear modifications influence the shape of the distribution as well as the total cross section. Lastly, it should be noted that the detector reconstruction and selection efficiency is treated separately in Eq. 5.1. Therefore, the kinematic output from PYTHIA was studied directly instead of passing it through the detector interaction and data reconstruction chain.

In the following, the acceptance and energy correction are separately detailed.

5.2.1.2 Acceptance correction

The acceptance correction C_{acc} takes into account differences in the rapidity distribution of fiducial Z bosons (defined below) in different collision systems and energies. An example of the Z-boson rapidity distributions of pp collisions at $\sqrt{s} = 7\,\mathrm{TeV}$ and pp collisions (in p–O configuration) at $\sqrt{s_{\mathrm{NN}}} = 9\,\mathrm{TeV}$ without kinematic selections is shown in Fig. 5.1 (left). As seen in the plot, the difference of their means is -0.28, while $0.5 \ln\left(\frac{8 \cdot 1}{1 \cdot 16}\right) \approx -0.35$. The discrepancy arises because isospin and the nPDFs skew the distribution of the p–O configuration towards negative rapidities, which lowers the mean.

However, because the experimentally measured cross sections are fiducial, the kinematic selections on the decay muons must also be taken into account. Fig. 5.1 (right) shows the rapidity distributions in the same configurations, but now of the fiducial Z bosons. Fiducial Z bosons are defined as those Z bosons that satisfy certain kinematic selections on the decay muons. In this case, both decay muons were required to have $p_{\mathrm{T}} > 20$ GeV/c and a dimuon mass of $60 < m_{\mu\mu} < 120$ GeV/c^2. A selection on the pseudorapidity of the muons was also applied. For ALICE measurements, this selection was $2.5 < \eta < 4.0$ or $-4.0 < \eta < -2.5$ at forward and backward rapidity respectively. For LHCb measurements, the muons were required to have $2.0 < \eta < 4.5$.

Finally, C_{acc} is given by the ratio of fiducial Z bosons in two different collision configurations. To account for isospin, the number of fiducial Z bosons for each configuration was averaged over the relevant contributions of binary collisions using Eq. 5.2 and 5.3.

$$N_{\mathrm{iso}}^{\mathrm{pA}} = \frac{Z}{A} N_{\mathrm{pp}} + \frac{A-Z}{A} N_{\mathrm{pn}} \tag{5.2}$$

$$N_{\mathrm{iso}}^{\mathrm{AA}} = \frac{Z^2}{A^2} N_{\mathrm{pp}} + \frac{Z(A-Z)}{A^2} N_{\mathrm{pn}} + \frac{(A-Z)Z}{A^2} N_{\mathrm{np}} + \frac{(A-Z)^2}{A^2} N_{\mathrm{nn}} \tag{5.3}$$

where N represents the number of fiducial Z bosons in a given configuration. For example, to compute the correction for ALICE p–O collisions at $\sqrt{s_{\mathrm{NN}}} = 9\,\mathrm{TeV}$ at forward rapidity from LHCb pp collisions at $\sqrt{s} = 7\,\mathrm{TeV}$ (see Fig. 5.1

(right)), $C_{\text{acc}} = \frac{\#\text{fiducial Z in } 2.5 < y < 4 \text{ in pO config 9 TeV}}{\#\text{ fiducial Z in } 2 < y < 4.5 \text{ in pp 7 TeV}} = \frac{2131.5 \pm 33}{3875 \pm 62} = 0.55 \pm 0.01$.

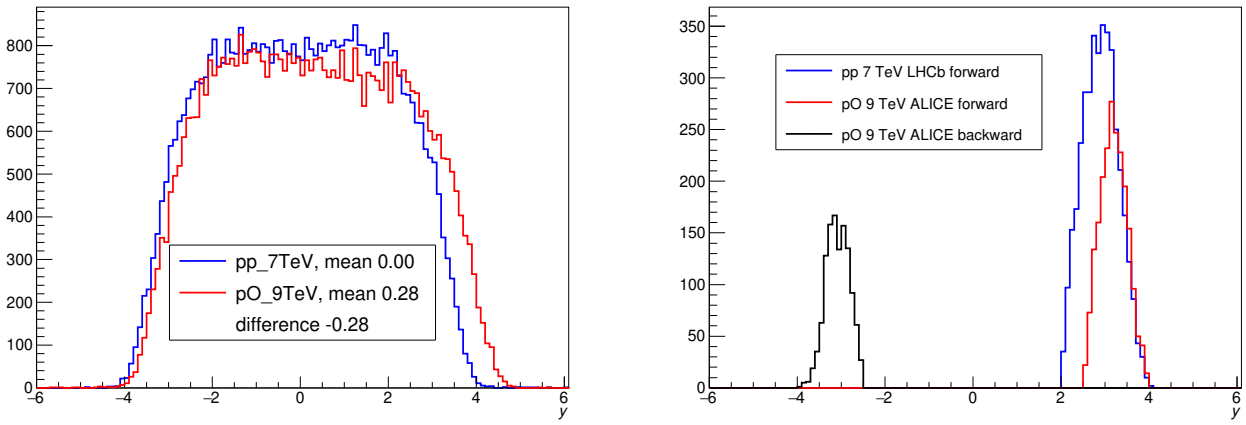

Figure 5.1: Rapidity distribution of all Z bosons (left) and of fiducial Z bosons (right) in two different collision configurations. The rapidities shown are in the laboratory frame.

5.2.1.3 Energy correction

At the end of each simulation, PYTHIA outputs the cross section for the processes it generates. These cross sections were used to correct for the energy dependence of measured cross sections. This was necessary because the measured cross sections are generally at different energies than those needed for the projections. The energy correction C_{energy} is given by the ratio of the PYTHIA cross section in two different configurations. As for the acceptance correction, an isospin-weighted average of the cross section was computed following Eq. 5.2 and 5.3 where necessary. For example, the energy correction between pp collisions in p–O configuration at $\sqrt{s} = 9\,\text{TeV}$ and pp collisions at $\sqrt{s} = 7\,\text{TeV}$ is given by $C_{\text{energy}} = \frac{\sigma_{\text{NN (pO config), 9 TeV}} = 9.003\text{e}{-07}\text{mb}}{\sigma_{\text{pp, 7 TeV}} = 6.760\text{e}{-07}\text{mb}} = 1.33$. Note that this correction is separate and independent of the aforementioned acceptance correction. Because PYTHIA only provides the value of the cross section without an uncertainty, no uncertainty was propagated for the energy correction.

5.3 Pythia simulation internal cross-checks

In order to compute the projections with Eq. 5.1, corrections for acceptance and energy differences are necessary. These corrections were obtained from PYTHIA simulations. However, in order to apply them, it must be verified that the rapidity distributions of the (fiducial) Z bosons and cross sections in PYTHIA match those of the data. In order to test the corrections, Eq. 5.1 was applied to compute various cross sections that have already been measured. By doing this, a direct comparison can be made between PYTHIA calculations and data and thereby justify the correction factors.

This section is dedicated to several consistency checks done with the PYTHIA simulations. The cross-checks on the total cross sections (used for the energy correction) and rapidity distributions (used for the acceptance corrections) are detailed in the following subsections.

5.3.1 Cross section in PYTHIA

In this subsection, the cross sections outputted by PYTHIA are compared with data. In addition to the value of the cross sections themselves, i.e. the absolute cross sections, the ratio between cross sections at different energies are also compared between PYTHIA and data.

Absolute cross sections in PYTHIA

The PYTHIA cross sections were compared with two LHCb measurements of the pp cross section at forward rapidity at $\sqrt{s} = 7\,\mathrm{TeV}$ and $\sqrt{s} = 8\,\mathrm{TeV}$ [149, 150]. For the comparisons, the PYTHIA value of the total cross section was multiplied by the fraction of fiducial Z's to obtain the expected forward cross section in the LHCb acceptance. This was done because the values given by the LHCb measurements pertain to fiducial cross sections.

At $\sqrt{s} = 7\,\mathrm{TeV}$, the total cross section is 676 pb and the fraction of fiducial Z's in the LHCb acceptance is 7.8%, leading to a fiducial cross section of 52 pb. This is lower than the measured value of $76.0 \pm 0.3 \pm 0.5 \pm 1.0 \pm 1.3$ pb, where the uncertainties are respectively statistical, systematic, due to the beam energy and due to the luminosity. At $\sqrt{s} = 8\,\mathrm{TeV}$, the total cross section is 795 pb with a fiducial fraction of 8.6%, leading to a fiducial cross section of 69 pb. Again, the PYTHIA value is lower than the measured value of $95.0 \pm 0.3\ (\mathrm{stat}) \pm 0.7\ (\mathrm{syst}) \pm 1.1\ (\mathrm{beam\ energy}) \pm 1.1\ (\mathrm{luminosity})$. The discrepancy can be explained by the fact that PYTHIA calculates the cross sections at leading order. Contributions from next-to-leading order (NLO) and next-to-next-to leading order (NNLO) calculations can be significant. In particular, going from LO to NLO can increase the total cross section by as much as 22%, although the exact value depends on the PDF set used to compute the cross section [151]. NNLO corrections show smaller differences of the order of 2-3% compared to NLO computations [151]. However, the higher-order corrections are beyond the scope of the estimate of the projections presented in this chapter.

Relative changes in cross sections in PYTHIA

In the corrections for energy, the ratio of cross sections at different energies were used. In in the previous check, it was found that the absolute cross sections do not reflect the values found in data. It was therefore investigated whether the relative changes in the cross section in PYTHIA could be correct despite this. For this, the same two LHCb measurements from the above cross-check were used. The cross section at $\sqrt{s} = 8\,\mathrm{TeV}$ was computed from the measured cross section at $\sqrt{s} = 7\,\mathrm{TeV}$ and the energy correction C_{energy}. In addition to the energy correction, an acceptance correction was applied because at higher energy, the rapidity distribution widens which leads to more (fiducial) Z bosons in the LHCb acceptance. Equation 5.1 was used, with an acceptance correction of $C_{\mathrm{acc}} = 1.11 \pm 0.2$ and energy correction of $C_{\mathrm{energy}} = 1.18$. The corresponding expected cross section at $\sqrt{s} =$

$8\,\mathrm{TeV}$ is 99.2 ± 2.3 pb, which is reasonably compatible with the reported value of $95.0 \pm 0.3\ (\mathrm{stat}) \pm 0.7\ (\mathrm{syst}) \pm 1.1\ (\mathrm{beam\ energy}) \pm 1.1\ (\mathrm{luminosity})$. This means that the ratio of cross sections at different energies in PYTHIA is a good proxy for the ratio in data.

5.3.2 Rapidity distributions in PYTHIA

In this subsection, two verifications of the rapidity distributions are shown. First the ALICE cross section in p–Pb at $\sqrt{s_{\mathrm{NN}}} = 8.16\,\mathrm{TeV}$ is computed from the LHCb pp cross section at $\sqrt{s} = 8\,\mathrm{TeV}$. Secondly, the forward/backward ratio is calculated in p–Pb collisions at $\sqrt{s_{\mathrm{NN}}} = 8.16\,\mathrm{TeV}$ in ALICE.

ALICE p–Pb cross section at $\sqrt{s_{\mathrm{NN}}} = 8.16\,\mathrm{TeV}$ from LHCb pp cross section at $\sqrt{s} = 8\,\mathrm{TeV}$

To compute the expected cross section in the ALICE measurement, Eq. 5.1 was used. For p–Pb collisions, the product of A_1 and A_2 is 208. The LHCb cross section at $\sqrt{s} = 8\,\mathrm{TeV}$ is 95 pb [150], with an acceptance correction of $C_{\mathrm{acc}} = 0.51 \pm 0.01$ and an energy correction of $C_{\mathrm{energy}} = 0.98$. For the energy correction, it can be seen that the decrease of the cross section due to shadowing is stronger than the increase due to the higher energy, leading to a value smaller than unity. The computed value of $\sigma_{pPb,8.16TeV}^{\mathrm{ALICE(PYTHIA)}} = 9.9 \pm 0.3$ nb is consistent with the measured value of $10.3\ \pm\ 1.4\ (\mathrm{stat})\ \pm 0.9\ (\mathrm{syst})$ nb.

Forward/backward ratio in p–Pb collisions at $\sqrt{s_{\mathrm{NN}}} = 8.16\,\mathrm{TeV}$

Another way to test the rapidity distribution generated by PYTHIA is to compare the ratios of the forward and backward cross section in p–Pb collisions. In PYTHIA pp collisions in p–Pb configuration at $\sqrt{s_{\mathrm{NN}}} = 8.16\,\mathrm{TeV}$, the number of fiducial Z bosons at forward rapidity is 2241, while it is 825 at backward rapidity. This leads to a forward/backward ratio of 2.7 ± 0.1. The cross sections measured in ALICE are $\sigma_{\mathrm{pPb,forward}} = 10.3\ \pm\ 1.4\ (\mathrm{stat})\ \pm\ 0.9\ (\mathrm{syst})$ nb and $\sigma_{\mathrm{pPb,backward}} = 3.7 \pm 0.6\ (\mathrm{stat}) \pm 0.3\ (\mathrm{syst})$. Assuming the statistical uncertainty to be uncorrelated and the systematic uncertainty to be fully correlated, the forward/backward ratio in data is $2.8 \pm 0.6\ (\mathrm{stat}) \pm 0.1\ (\mathrm{syst})$. This is consistent with the value found with PYTHIA.

LO versus NLO distributions

In the PYTHIA simulations, LO computations were done to compute the Z-boson cross section. It already was mentioned that higher order computations are necessary to properly describe absolute cross sections. To investigate the influence of higher order corrections to the rapidity distribution, Z bosons were generated at NLO in POWHEG simulations. Figure 5.2 shows the rapidity distributions of generated fiducial Z bosons, with the fiducial region specified for the ALICE analysis. The right plot shows the ratio of the PYTHIA over POWHEG distributions, which only deviates from unity at the edge of the fiducial region where few Z bosons are generated. This means that the LO distributions from which the acceptance correction C_{acc} was computed are sufficient for the projections in p–O and O–O collisions.

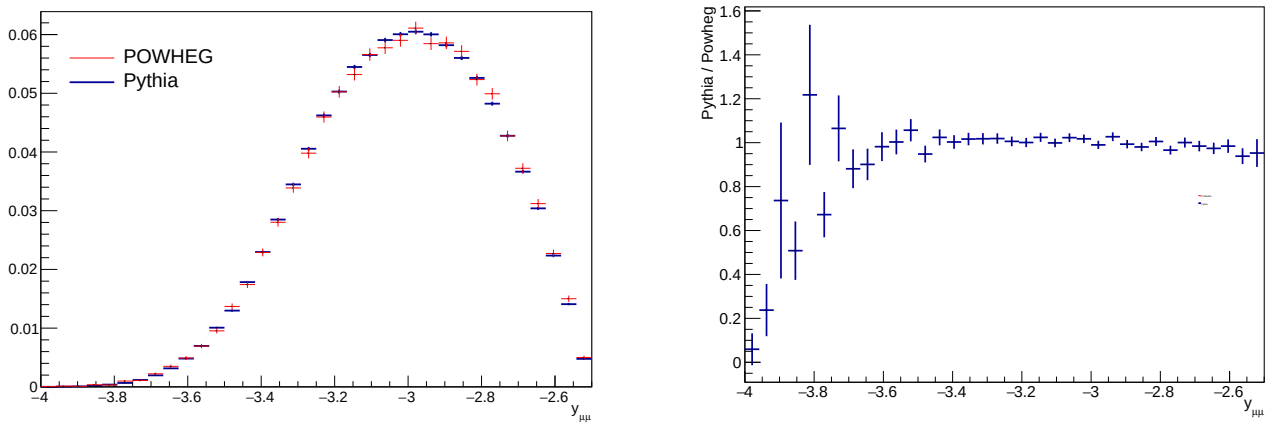

Figure 5.2: Rapidity distributions (left) and ratio (right) of generated fiducial Z bosons in Pb–Pb collisions at $\sqrt{s_{\mathrm{NN}}} = 5.02\,\mathrm{TeV}$ in PYTHIA LO and POWHEG NLO simulations. The fiducial region is defined by the selections in ALICE analyses.

5.3.3 Conclusions from cross checks

Two conclusions were drawn from the cross checks. The first is that the rapidity distributions in data are well described by PYTHIA simulations using computations at LO. Secondly, although the absolute cross sections differ from those measured, relative differences in the LO PYTHIA cross sections at different energies are similar to relative differences in measured cross sections. This validates the use of the PYTHIA simulations for the projections, as described in Eq. 5.1.

5.4 Results

In this section, the values of the estimated measured yields are presented. To compute them, Eq. 5.1 was used. The values of the detector reconstruction and selection efficiency $A\epsilon$ and product of atomic mass numbers $A_1 A_2$ depend on the collision configuration. Therefore, the projections for p–O collisions and O–O collisions are each detailed in separate subsections.

5.4.1 p–O projections

In p–O collisions, the product of A_1 and A_2 is 16. The detector reconstruction and selection efficiency is assumed to be the same as in the ALICE p–Pb analysis at $\sqrt{s_{\mathrm{NN}}} = 8.16\,\mathrm{TeV}$, in which the value was $A\epsilon = 0.74$. The projections have been computed using separately the LHCb pp measurement at $\sqrt{s} = 7\,\mathrm{TeV}$ and ALICE p–Pb measurement at $\sqrt{s_{\mathrm{NN}}} = 8.16\,\mathrm{TeV}$ mentioned in Sec. 5.2. To use the p–Pb measurement for the computation of the projections, the p–Pb cross sections was first be converted into a pp cross section by $\sigma_{\mathrm{pp}} = \sigma_{\mathrm{pA}}/\mathrm{A}$. The uncertainty on each cross section represents the total uncertainty, computed by assuming that all given uncertainties in the corresponding

measurement are uncorrelated. It was mentioned earlier that currently, only collisions in the p–going directions are foreseen. However, projections for O–going collisions are also shown, as the collision configurations are not yet finalized.

The various values of the pp cross section, C_{acc}, C_{energy} and the expected measured yield are shown in Tab. 5.1. It can be seen in the table that expected yields between the two different input measurements agree well with each other. However, the uncertainty on the projection from the p–Pb measurement has a much larger uncertainty than the projection from the pp measurement. This is caused by the larger relative uncertainty in the reference measurement itself (16% versus 2.6% uncertainty in the pp measurement).

input measurement	σ_{pp} [nb]	projection rapidity	projection energy	C_{acc}	C_{energy}	expected measured yield [dimuons per nb^{-1}]
pp at $\sqrt{s} = 7\,\mathrm{TeV}$	0.076 ± 0.002	forward	$\sqrt{s_{\mathrm{NN}}} = 9\,\mathrm{TeV}$	0.55 ± 0.01	1.33	0.66 ± 0.02
pp at $\sqrt{s} = 7\,\mathrm{TeV}$	0.076 ± 0.002	backward	$\sqrt{s_{\mathrm{NN}}} = 9\,\mathrm{TeV}$	0.32 ± 0.01	1.33	0.38 ± 0.01
p–Pb at $\sqrt{s_{\mathrm{NN}}} = 8.16\,\mathrm{TeV}$	0.050 ± 0.008	forward	$\sqrt{s_{\mathrm{NN}}} = 9\,\mathrm{TeV}$	0.97 ± 0.02	1.16	0.66 ± 0.11
p–Pb at $\sqrt{s_{\mathrm{NN}}} = 8.16\,\mathrm{TeV}$	0.018 ± 0.003	backward	$\sqrt{s_{\mathrm{NN}}} = 9\,\mathrm{TeV}$	1.51 ± 0.05	1.16	0.37 ± 0.07

Table 5.1: Projections for Z-boson production in p–O collisions.

5.4.2 O–O projections

In the calculation of the p–O projections, the values obtained using the ALICE measurement were found to be consistent with the one using the LHCb measurement, though with a higher uncertainty. Consequently, for the O–O projections only the LHCb pp measurement at $\sqrt{s} = 7\,\mathrm{TeV}$ was used. In contrast to the p–O projections, the product of A_1 and A_2 in O–O collisions is $16^2 = 256$. The detector reconstruction and selection efficiency depends on the occupation level, which will be higher in O–O collisions than in p–O collisions. Charged particle multiplicities in O–O collisions are expected to be similar to those found in Pb–Pb collisions at $\sqrt{s_{\mathrm{NN}}} = 5.02\,\mathrm{TeV}$ in the 70-90% centrality interval [152]. From the Z-boson measurement in Pb–Pb collisions described in this thesis, the efficiency in this centrality interval is $A\epsilon = 0.73$. As O–O collisions are symmetric, the projections were computed for only one rapidity window.

The projections were computed for the current baseline for the center-of-mass energy of $\sqrt{s_{\mathrm{NN}}} = 6.37\,\mathrm{TeV}$ and also for $\sqrt{s_{\mathrm{NN}}} = 5.02\,\mathrm{TeV}$ which is still under consideration. Table 5.2 shows the values of the projections for the O–O collisions.

input measurement	σ_{pp} [nb]	projection rapidity	projection energy	C_{acc}	C_{energy}	expected measured yield per nb^{-1}
pp at $\sqrt{s} = 7\,\mathrm{TeV}$	0.076 ± 0.002	forward	$\sqrt{s_{\mathrm{NN}}} = 6.37\,\mathrm{TeV}$	0.33 ± 0.01	0.85	4.00 ± 0.15
pp at $\sqrt{s} = 7\,\mathrm{TeV}$	0.076 ± 0.002	forward	$\sqrt{s_{\mathrm{NN}}} = 5.02\,\mathrm{TeV}$	0.22 ± 0.01	0.64	2.00 ± 0.10

Table 5.2: Projections for Z-boson production in O–O collisions.

5.4.3 Experimental uncertainties

The kinematic selections on the dimuons ensure that background in the measurement is roughly 1% in p–Pb collisions, and smaller than 1% in Pb–Pb at $\sqrt{s_{\mathrm{NN}}} = 5.02\,\mathrm{TeV}$ (as explained in subsection 3.6.1). Because of this, the signal extraction is done by counting the number of entries in the $60 < m_{\mu\mu} < 120$ GeV/c^2 mass interval. Consequently, the uncertainty on the signal extraction is the square root of the number of entries. This uncertainty dominates the statistical uncertainty of the measurement.

The systematic uncertainties in the p–Pb and Pb–Pb measurements are dominated by the uncertainty in the calculation of the detector efficiency. This uncertainty arises from discrepancies in the detector response in the MC simulations used to calculate the efficiency. At the current time, it is unclear whether the detector response can be more accurately simulated during LHC Run 3. Therefore, as a conservative estimate, the same order of magnitude of systematic uncertainty is expected. This ranges from 6.2 to 8.2%.

5.4.4 Comparison with p–Pb and Pb–Pb collisions

In section 4.2, the nuclear effects probed in Pb–Pb collisions were discussed. The effects probed depend on the momentum fraction x of the partons in the collisions. To see if p–O and O–O collisions are sensitive to the same physics, a comparison of the bjorken-x values is shown in Tab. 5.3. For completeness, p–Pb collisions at $\sqrt{s_{\mathrm{NN}}} = 5.02\,\mathrm{TeV}$ and $\sqrt{s_{\mathrm{NN}}} = 8.16\,\mathrm{TeV}$ are also included, as measurements in ALICE have been done in those configurations. Equation 4.1 was used to obtain the values of bjorken-x. For p–O and p–Pb collisions, the boost of the center-of-mass frame was taken into account by shifting the rapidity measured in the laboratory frame by $\Delta y = 0.347$ and $\Delta y = 0.465$ respectively.

At backward rapidity, all configurations probe bjorken-x values of the order of $[10^{-4},\ 10^{-3}]$, which indicates sensitivity to nuclear shadowing. At forward rapidity, the bjorken-x probed in p–O and O–O collisions is smaller than those in p–Pb and Pb–Pb collisions. As a result, the measurements will be less sensitive to both the EMC and antishadowing effect. Because these are competing effects, the decrease in sensitivity to both could compensate. In the end, the nuclear effects probed by the p–O and O–O collisions will be similar to those in p–Pb and Pb–Pb collisions.

5.5 Conclusions

The projections per nb^{-1} for p–O and O–O collisions are summarized in Table 5.4. Given the expected luminosities of 5 nb^{-1} for p–O collisions and 1 nb^{-1} for O–O collisions, the yields would be respectively 3 and 4 Z bosons. With these yields, a measurement of Z-boson production during the oxygen runs will not be feasible.

To obtain a similar number of candidates as were used in the p–Pb and Pb–Pb measurement (64 and 208

collision system	COM energy [TeV]	CMS rapidity	x1	x2
Pb–Pb (or O–O)	5.02	$2.5 < y < 4$	$[0.22, 0.99]$	$[3.33 \cdot 10^{-4}, 1.49 \cdot 10^{-3}]$
p–Pb (p–going)	5.02	$2.03 < y < 3.53$	-	$[5.30 \cdot 10^{-4}, 2.37 \cdot 10^{-3}]$
p–Pb (Pb–going)	5.02	$-4.47 < y < -2.97$	$[0.35, 1.58]$	-
p–Pb (p–going)	8.16	$2.03 < y < 3.53$	-	$[3.26 \cdot 10^{-4}, 1.46 \cdot 10^{-3}]$
p–Pb (Pb–going)	8.16	$-4.47 < y < -2.97$	$[0.22, 0.97]$	-
O–O	6.37	$2.5 < y < 4$	$[0.17, 0.78]$	$[2.62 \cdot 10^{-4}, 1.18 \cdot 10^{-3}]$
p–O (p–going)	9	$2.15 < y < 3.65$	-	$[2.62 \cdot 10^{-4}, 1.18 \cdot 10^{-3}]$
p–O (O–going)	9	$-4.35 < y < -2.85$	$[0.17, 0.78]$	-

Table 5.3: Comparison of bjorken-x values probed in various collision systems at several energies.

Collision system	expected measured yield per nb^{-1}
p–O, p–going at $\sqrt{s_{\mathrm{NN}}} = 9\,\mathrm{TeV}$	0.66 ± 0.02
p–O, O–going at $\sqrt{s_{\mathrm{NN}}} = 9\,\mathrm{TeV}$	0.38 ± 0.01
O–O at $\sqrt{s_{\mathrm{NN}}} = 5.02\,\mathrm{TeV}$	2.00 ± 0.10
O–O at $\sqrt{s_{\mathrm{NN}}} = 6.37\,\mathrm{TeV}$	4.00 ± 0.15

Table 5.4: Projections for Z-boson production in p–O and O–O collisions per nb^{-1} of luminosity.

respectively), higher luminosities would be needed. For p–O collisions at $\sqrt{s_{\mathrm{NN}}} = 9\,\mathrm{TeV}$, the integrated luminosity would have to be 98 nb^{-1}, while for O–O collisions at $\sqrt{s_{\mathrm{NN}}} = 6.37\,\mathrm{TeV}$, 53 nb^{-1} would be required. Such a measurement would be valuable to constrain the A-dependence of nuclear PDFs, which is currently not yet well understood.

Chapter 6

J/ψ pair production: analysis method and results

In this chapter the measurement of the di-J/ψ (or J/ψ pair) cross section is presented. All J/ψ are studied in their dimuon decay channel, and the cross section is calculated as

$$\sigma_{J/\psi J/\psi} = \frac{N_{J/\psi J/\psi}}{A\epsilon(J/\psi J/\psi) \times \mathcal{L} \times \mathcal{B}^2_{J/\psi \to \mu^+\mu^-}}, \tag{6.1}$$

where $N_{J/\psi J/\psi}$ is the number of di-J/ψ, $A\epsilon(J/\psi J/\psi)$ the di-J/ψ acceptance and efficiency, $\mathcal{L}$ the integrated luminosity of the data sample and $\mathcal{B}_{J/\psi \to \mu^+\mu^-}$ the branching ratio of single J/ψ to a muon pair which is $5.961 \pm 0.033\%$ [2].

In the following sections, the event and track selection for this analysis will be detailed, followed by a separate section for each of the terms in Eq. 6.1. Finally, the obtained cross section is presented.

6.1 Event selection

The di-J/ψ analysis is done on the Run-2 dataset of pp collisions at $\sqrt{s} = 13\,\mathrm{TeV}$ at the LHC. The data were collected from 2016 to 2018. Data taken in 2015 were not considered for the analysis, even though they also comprise pp collisions at $\sqrt{s} = 13\,\mathrm{TeV}$ and were part of the Run-2 data taking. The reason for excluding the 2015 data is that the data taking conditions (such as trigger conditions of the spectrometer) were different than for the 2016-2018 data, which complicates their integration. The 2015 data represent about 10% of the entire Run-2 dataset, so that their omission does not strongly reduce the size of the data sample [153].

The analysis was done on CMUL7 events, which were detailed in subsection 3.1.1. A physics selection was applied on the CMUL7 events to remove background collisions. The procedure to remove these background events

in Pb–Pb collisions was also explained in subsection 3.1.1. Additional criteria are applied to pp events. Because the instantaneous luminosity is higher in pp collisions than in Pb–Pb collisions, it is possible for two distinct pp collisions to occur within a single event. Such an event is then considered a pileup event. There are two categories of pileup events. The first is same-bunch pileup when there are two or more collisions occurring in the same bunch crossing. The second category is out-of-bunch pileup, when there are two or more collisions in a bunch crossing separate from the one that triggered the acquisition. The rate of out-of-bunch pileup depends on the readout time of a detector. For example, the SPD has a large readout time of 300 ns, which corresponds to 12 bunch crossings. Using information from the V0, which has a readout time of 25 ns, out-of-bunch pileup within the SPD readout time can be rejected. Additionally, the presence of multiple reconstructed vertices in the SPD can be used to tag pileup from same-bunch-crossing collisions and out-of-bunch pileup within the SPD readout time. An event is tagged as pileup and removed if there are multiple vertices separated more than 0.8 cm along the beam axis. A more refined pileup removal involves specifying the number of contributors N_{cont} to each vertex, depending on the event multiplicity. The latter is approximated by the number of SPD tracklets (i.e. line segments reconstructed using only SPD hits) $N_{\mathrm{tracklets}}$. For this multiplicity-dependent pileup removal, events are rejected if there are multiple vertices more than 0.8 cm separated along the beam axis and $N_{\mathrm{cont}} \geq 3$ for events with $N_{\mathrm{tracklets}} < 20$, $N_{\mathrm{cont}} \geq 4$ for events with $20 < N_{\mathrm{tracklets}} < 50$ and $N_{\mathrm{cont}} \geq 5$ for events with $N_{\mathrm{tracklets}} > 50$. The pileup rejection criteria are based on the number of SPD tracklets from which the vertices are reconstructed. For collisions with interaction vertices that are strongly displaced along the z-axis, a large number of the outgoing particles may lie outside of the SPD acceptance. This decreases the efficiency of the pileup removal using SPD tracklets. As such, the rejection criteria are tuned to collisions whose z-coordinate is displaced less than 10 cm from the nominal interaction point, which coincides with the center of the SPD. The same selection is therefore also applied in the data, requiring events with $|V_z| < 10$ cm.

The number of events at various stages of the selection criteria are shown in Table. 6.1.

Event selection	number of millions of events
triggered	667.0
+ physics selection	603.7
+ mult. dep. pileup rejection	602.5
+ V_z selection	587.4

Table 6.1: Number of million CMUL7 events at successive stages of event selection criteria.

6.1.1 Track selection

The selection criteria on the muon tracks are almost identical to those for the Z-boson analysis, described in subsection 3.1.2. The only difference is that for the J/ψ, no requirement is set for the p_{T} of the muons, whereas in the Z-boson analysis a transverse momentum $p_{\mathrm{T}} > 20$ GeV/c was required. The condensed list of track selection criteria is

- $-4 < \eta_\mu < -2.5$.
- $170^\circ < \theta_{\rm abs} < 178^\circ$, where $\theta_{\rm abs}$ is the polar angle at the exit point of the front absorber.
- $p_\mu \times DCA < 6\sigma$, where p_μ is the muon momentum and DCA (Distance of Closest Approach) is its closest distance to the primary vertex.
- Only muon tracks that can be matched to track segments in the tracking stations were considered.

6.2 Signal extraction

The (di-)J/ψ are reconstructed in their muonic decay channels in the spectrometer. A 2-dimensional invariant mass spectrum is computed from all combinations of double dimuon pairs (each dimuon consisting of an unlike-sign muon pair) per event. The 2D mass spectrum obtained over the full data sample is shown in Figure 6.1. No ordering of the indices 1 and 2 was done for the spectrum. In total, 2575 quadrimuon pairs were found in the invariant mass range $[2,5]$ GeV/c^2 $\times[2,5]$ GeV/c^2.

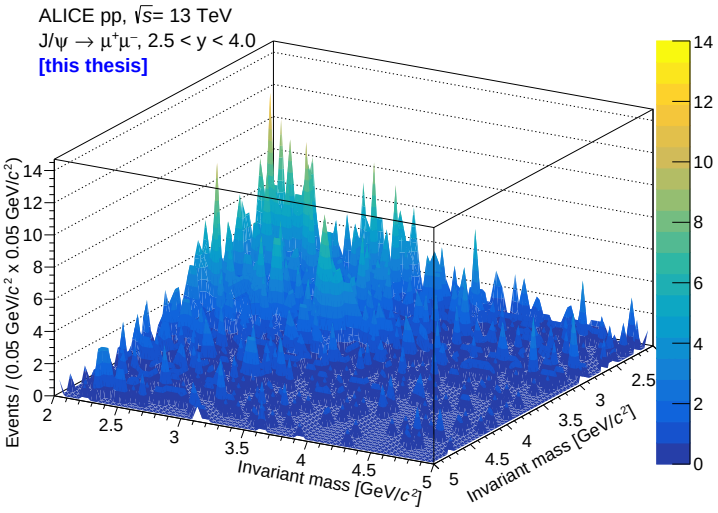

Figure 6.1: 2-dimensional distribution of quadrimuon pairs.

The di-J/ψ signal is obtained from a 2D fit to the 2D invariant mass spectrum. However, a 1D fit is done first, to obtain the parameters of the single J/ψ fit functions which enter in the 2D fit function.

6.2.1 Fit configurations

In the following subsections, the 1D and 2D fits are described. For the fits, various configurations were used. The fit configurations differ in the background functions, parameters for signal functions, and the mass interval over which the fit was performed. A description of the configurations is now given.

The signal function of the J/ψ (and $\psi(2S)$) is always taken to be an extended Crystal Ball (CB2) function. The CB2 function consists of a gaussian core together with two exponential tails. In the fits, the tail parameters are always kept fixed. There are two separate sets of values to which they can be fixed. One set was obtained from fits to data while letting all tail parameters free. Another was obtained by the same procedure, but using MC simulations instead of data.

To fit the combinatorial background, three different functions were used. These are an exponential of a 2nd-order polynomial, a double exponential, and a ratio of a first-order polynomial over a second-order polynomial.

Lastly, two mass ranges were considered for the fits: $[2.0, 4.5]$ GeV/c^2 and $[2.2, 4.9]$ GeV/c^2 ranges.

Analytic expressions of the functions mentioned above, as well as a table containing the tail parameters of the CB2 function are given in Appendix A. All combinations of the above variations were used as fit configurations. The 3 different background functions, 2 sets of tail parameters and 2 fit intervals therefore lead to 12 different values for the signal extraction. In the following subsections, example plots of the fits will be shown. The same fit configuration will be used for all example plots. The configuration pertains to the fit using an exponential of 2nd order polynomial as background function, using the tail parameters obtained from fits to data for the signal functions, fitted over the mass range of $[2, 4.5]$ GeV/c^2.

6.2.2 1-dimensional fits

For the 1D fits, the entire single dimuon invariant mass spectrum (i.e. not only the dimuons obtained in the di-J/ψ signal extraction) was computed. The large number of dimuons in the data sample will allow to establish the fit parameters of the single J/ψ with high accuracy. The 1D fits consist of three separate steps.

In the first step, only a background function is fitted, simultaneously over the invariant mass intervals $[m_{\min}, 2.8]$ GeV/c^2 and $[3.4, m_{\max}]$ GeV/c^2, where $m_{\min}$ and $m_{\max}$ are respectively the minimum and maximum mass of the fit range considered. The intervals were chosen to avoid the J/ψ and $\psi(2S)$ signal regions. The first step then yields initial values of the background parameters.

In the second step, the J/ψ signal function is added. A fit of the combined background and J/ψ functions is then done around the J/ψ invariant mass peak of $[3.026, 3.167]$ GeV/c^2. In this fit, the parameters of the background function are kept fixed, and the tails of the CB2 function are also fixed.

In the third step, the $\psi(2S)$ signal function is added. The signal function of the $\psi(2S)$ is also a CB2 function with the same tails as the J/ψ signal function. Furthermore, the gaussian mean of the $\psi(2S)$ is set to the gaussian mean of the J/ψ signal function, shifted by the difference of their PDG mass. The gaussian width of the $\psi(2S)$ is set to 1.05 times the width of the J/ψ signal function. Ultimately, only the normalisation of the $\psi(2S)$ signal function is kept as a free parameter. For the third fit, all background parameters (including normalisation) are set free. The gaussian mean and width of the J/ψ signal function as well as the normalisation of the J/ψ and $\psi(2S)$ signals are also set free.

The third and final fit is done over the full mass interval considered. An example of the completed fit results after the third step is shown in Fig. 6.2.

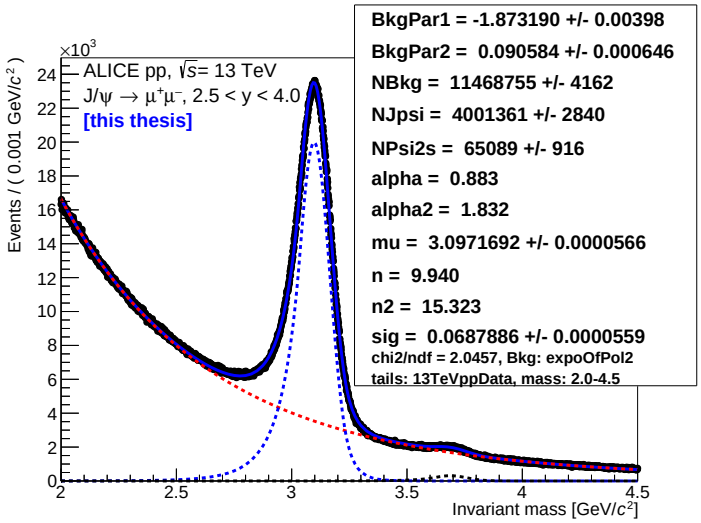

Figure 6.2: Results obtained in the 1-dimensional fit procedure. The J/ψ, $\psi(2S)$ and background contributions are also shown separately.

6.2.3 2-dimensional fits

After the 1-dimensional fits have been obtained, a 2-dimensional fit function is defined. This is done by introducing a second invariant mass variable m_2, and essentially create a copy of the 1D signal function, but as a function of m_2. The 2-dimensional fit function F is then defined as

$$\begin{aligned} F(m_1, m_2) = N_{(\mathrm{J}/\psi)_1,(\mathrm{J}/\psi)_2}\mathbf{J}/\psi_{\mathbf{1}}(\mathbf{m_1})\mathbf{J}/\psi_{\mathbf{2}}(\mathbf{m_2}) + N_{B_1,(J/\psi)_2}\mathbf{B_1}(\mathbf{m_1})\mathbf{J}/\psi_{\mathbf{2}}(\mathbf{m_2}) \\ + N_{(J/\psi)_1,B_2}\mathbf{J}/\psi_{\mathbf{1}}(\mathbf{m_1})\mathbf{B_2}(\mathbf{m_2}) + N_{B_1,B_2}\mathbf{B_1}(\mathbf{m_1})\mathbf{B_2}(\mathbf{m_2}), \end{aligned} \tag{6.2}$$

where $N_{(\mathrm{J}/\psi)_1,(\mathrm{J}/\psi)_2}$ represents the number of di-J/ψ, $N_{B_1,(J/\psi)_2}$ and $N_{(J/\psi)_1,B_2}$ represent the mixed background (meaning a J/ψ from one variable and a background dimuon from the other) and N_{B_1,B_2} represents the pure background (meaning background dimuons from both variables). The bolded $\mathbf{J}/\psi$ and $\mathbf{B}$ indicate the J/ψ signal function and the background function respectively, as a function of the first invariant mass variable m_1 or the second invariant mass variable m_2. The $\psi(2S)$ signal function is not included in the 2-dimensional fit, as its contributions are expected to be negligible.

In the 2D fit, the background function is kept the same, although the parameters are left free because the combinatorial background is not expected to be the same for di-J/ψ as for single J/ψ. For the J/ψ signal, the function is kept the same and the parameters are fixed to those obtained from the 1D fit. This is done because the J/ψ signal is mainly driven by the detector response. The data shown in Fig. 6.1 are then fitted to the 2D function in Eq. 6.2.

The projections of the 2D fit along the m_1 and m_2 axes is shown in Figure 6.3.

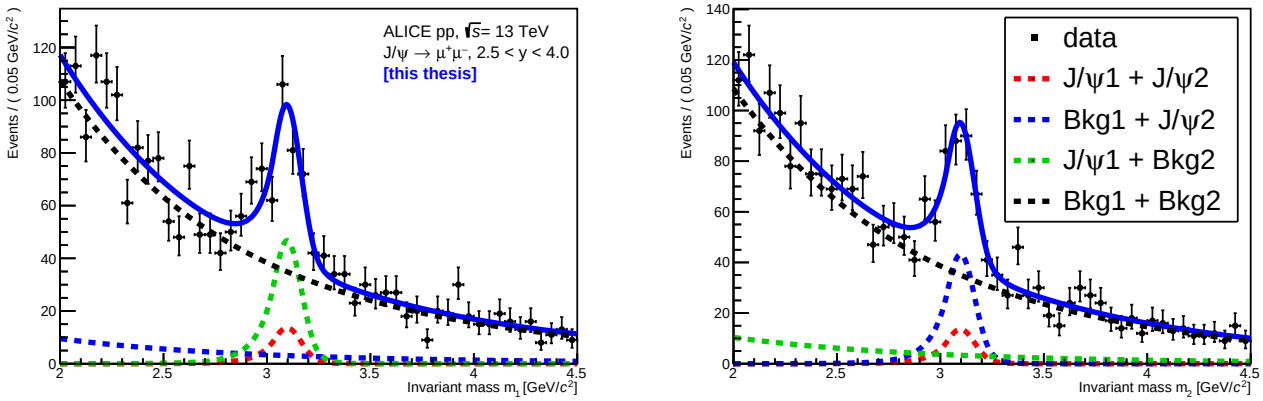

Figure 6.3: 1-dimensional projections of the 2-dimensional fit to the data. The left plot shows the projection as a function of the m_1 variable, while the right plot shows the projection versus m_2.

From the 2D fit, the number of di-J/ψ is extracted. As mentioned before, 12 different fit configurations were used, which leads to 12 different signal extractions shown in Figure 6.4. The average of all configurations is taken to be the final value of the signal extraction. The statistical uncertainty is the average of the uncertainty of each configuration, and the systematic uncertainty is the standard deviation of the central values. The number of di-J/ψ pairs found is finally $59.3 \pm 13.5\ (\mathrm{stat}) \pm 4.4\ (\mathrm{syst})$.

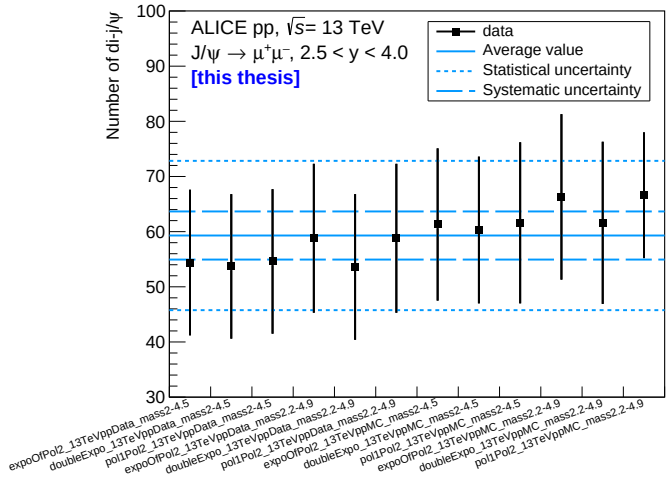

Figure 6.4: Number of di-J/ψ extracted from fits for various fit configurations. The final value, along with the statistical and systematic uncertainties are shown as well.

6.3 Acceptance and efficiency

The $A\epsilon$ of the di-J/ψ is factorised as the product of the $A\epsilon$ two single J/ψ according to

$$A\epsilon(J/\psi J/\psi) = A\epsilon(J/\psi)A\epsilon(J/\psi). \tag{6.3}$$

Due to time constraints, it was not possible to compute the values of the single J/ψ $A\epsilon$ from simulations in this thesis. The value was therefore taken from another analysis done on single J/ψ over the same data set. However, this can only be done if the p_{T} and rapidity distributions of the J/ψ in the di-J/ψ are similar to those of single J/ψ. The normalised p_{T} and rapidity distributions of single dimuons as well as of the dimuons comprising the di-dimuons signal (i.e. for each di-dimuon, the two dimuon comprising it were evaluated separately) are shown in Figure 6.5. A selection on the invariant mass of $2.9 < M_{J/\psi} < 3.3$ GeV/c^2 was applied, in order to enhance the J/ψ signal / background ratio so that the J/ψ kinematics are dominant in the p_{T} and y distributions. For the di-dimuons, the low number of entries enhances the effect of statistical fluctuations. In the p_{T} distributions, the means differ by 0.26 GeV/c (8%), while the means of the rapidity distributions differ by 0.03 (1%). However, the differences are an order of magnitude smaller than the uncertainties, so that distributions can be considered equal.

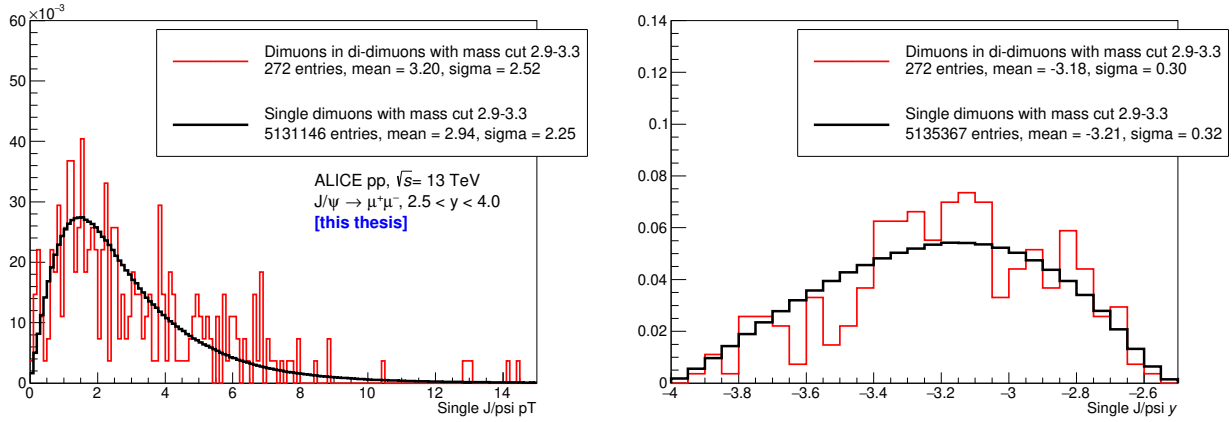

Figure 6.5: Comparison of p_{T} (left) and rapidity (right) distribution between all single dimuons and the dimuons in the di-dimuon spectrum. A selection on the invariant mass of $2.9 < M_{J/\psi} < 3.3$ GeV/c^2 was applied on all dimuons shown in order to enhance the J/ψ signal / background as much as possible.

As a first approximation, it should therefore suffice to use the values obtained in the single J/ψ analysis, which are $A\epsilon(J/\psi) = 0.2593 \pm 0.0001(\mathrm{stat}) \pm 0.010(\mathrm{syst})$ [153]. The corresponding value of the di-J/ψ $A\epsilon$ is then $0.067 \pm 0.005(\mathrm{syst})$, where the statistical uncertainty has been neglected and the relative systematic uncertainty was computed as twice the relative systematic uncertainty on the single J/ψ $A\epsilon$.

6.4 Luminosity

The luminosity can be computed given the number of MB events together with the corresponding MB cross section. The CINT7 class was chosen as MB event and the corresponding reference cross section is σ_{V0}. The latter was determined in a van der Meer scan, and was evaluated as $\sigma_{\mathrm{V0}} = 57.8 \pm 1.2$ mb, where the uncertainty is systematic (the statistical uncertainty is negligible) [154]. The luminosity is then calculated according to

$$\mathcal{L} = \frac{N_{\mathrm{MB}}}{\sigma_{\mathrm{V0}}} = \frac{N_{\mathrm{CMUL7}} F_{\mathrm{norm}}}{\sigma_{\mathrm{V0}}}, \tag{6.4}$$

where in the second fraction the number of MB events is obtained from the number of CMUL7 events multiplied by the normalisation factor introduced in 3.4. For the di-J/ψ analysis, only the offline direct method and offline indirect method were used to estimate the normalisation factor. The normalisation factor was computed with equations 3.9 and 3.10, on CINT7 events that pass all the event selection criteria described in Section 6.1. The values of the normalisation factors per run are shown in Figure 6.6. Fluctuations in the value of the direct method can be seen to be significantly larger than in the indirect method. The run-by-run values are then aver-

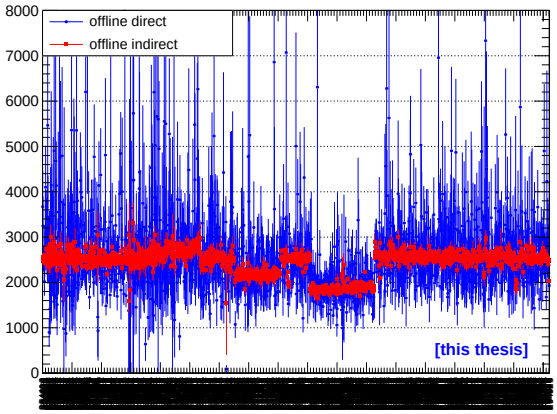

Figure 6.6: Normalisation factor as a function of run for the Run-2 dataset of pp collisions at $\sqrt{s} = 13\,\mathrm{TeV}$.

aged to a single value, using the number of analysed CMUL7 events per run as weight. The weighted average of the indirect method is taken as the value of the normalisation factor. The difference with the value obtained from the direct method is taken as the systematic uncertainty on the normalisation factor, equal to 2.9%. This leads to a normalisation factor of $2399.0 \pm 1.4\ (\mathrm{stat}) \pm 69.1\ (\mathrm{syst})$. Using Eq. 6.4, the integrated luminosity is then $\mathcal{L} = 24.38 \pm 0.01\ (\mathrm{stat}) \pm 0.87\ (\mathrm{syst})\mathrm{pb}^{-1}$, where the systematic uncertainty on the V0 cross section was taken into account as well.

6.5 Contamination from $b\bar{b}$ pairs.

In the measurement presented in this thesis, no separation is made between prompt J/ψ and non-prompt J/ψ as this is not currently feasible with the spectrometer. Nonetheless, it is interesting to consider the sensitivity to non-prompt contributions from decays of $b\bar{b}$ pairs that hadronise into two B hadrons, which both decay into a J/ψ. In this section, the influence of this process in the di-J/ψ measurement is studied.

In order to determine the sensitivity of the measurement to the contamination of $b\bar{b}$ pairs, simulations were done using PYTHIA 6. For the simulations, three different input processes were used, each denoted by an arbitrary internal name in ALICE:

- kPyBeauty: Configuration which simulates 1 $b\bar{b}$ pair per event, based on LO calculations.
- kPyBeautyppMNR: This configuration is tuned to NLO computations [155], and instead of only $b\bar{b}$ pairs, an entire pp event is simulated.
- kPyBeautyppMNRwmi: the same as kPyBeautyppMNR but this configuration includes mechanisms for multi-parton interactions

In the simulations, all B hadrons were forced to decay into J/ψ. For each of the three configurations, 50000 events, each containing at least one $b\bar{b}$ pair were simulated. A number of events containing two $b\bar{b}$ pairs ($\mathcal{O}(100)$ per configuration) were observed. By counting the number of events in which two or more J/ψ enter the ALICE spectrometer rapidity of $2.5 < y < 4.0$, the probability of such events $P(\text{two or more J}/\psi \text{ in } 2.5 < y < 4.0)$ can be computed. The contamination cross section can then be calculated as

$$\sigma^{\text{ALICE}}_{b\bar{b}\to J/\psi+J/\psi} = \sigma^{\text{tot}}_{b\bar{b}} \times P(\text{two or more J}/\psi \text{ in } 2.5 < y < 4.0) \times \mathcal{B}^2_{B\to J/\psi} \tag{6.5}$$

where $\sigma^{\text{tot}}_{b\bar{b}}$ is the total $b\bar{b}$ cross section, and $\mathcal{B}_{B\to J/\psi}$ the branching ratio of B hadrons to J/ψ. The total cross section was determined in an LHCb measurement to be $495 \pm 2(\text{stat}) \pm 52(\text{stat})\mu b$ [156], and the PDG branching ratio is $1.094 \pm 0.032\%$ [2]. $P(\text{two or more J}/\psi \text{ in } 2.5 < y < 4.0)$ was computed for each simulation configuration. The value and systematic uncertainty of the probability were then computed as the average and standard deviation of the three configurations, leading to $P(\text{two or more J}/\psi \text{ in } 2.5 < y < 4.0) = 3.2 \pm 0.3(\text{syst})\%$. With these numbers (neglecting the statistical uncertainty on $\sigma_{b\bar{b}}$), the cross section from J/ψ pairs originating from $b\bar{b}$ pairs in the ALICE acceptance is 1.9 ± 0.3 (syst) nb.

It is also possible that from a $b\bar{b}$ pair, only one J/ψ enters the spectrometer acceptance, along with a J/ψ formed from a $c\bar{c}$ pair. Contributions of this kind are assumed to be negligible in the analysis as they require a $c\bar{c}$ pair in addition to a $b\bar{b}$ pair in the same event, both within the spectrometer acceptance.

6.6 Summary of systematic uncertainties

In the previous sections, various contributions to the systematic uncertainty of the cross sections were given. Table 6.2 presents a summary of all contributions.

source	contribution
signal extraction	7.4%
acceptance and efficiency $A\epsilon$	7.6%
luminosity	3.6%
branching ratio	1.1%
total	11.2%

Table 6.2: Overview of contributions to the systematic uncertainty of the di-J/ψ cross section.

6.7 Results

With the values obtained in the previous sections, the cross section computed with Eq. 6.1 yields a cross section of $10.2 \pm 2.3\ (\mathrm{stat}) \pm 1.1\ (\mathrm{syst})$ nb. The obtained cross section is inclusive, as no separation was made between prompt and non-prompt contributions. This complicates the comparison with an LHCb measurement, also done in pp collisions at $\sqrt{s} = 13\,\mathrm{TeV}$, in which the non-prompt contributions were removed [99]. In the LHCb analysis, the prompt di-J/ψ production cross section was measured to be $15.2 \pm 1.0\ (\mathrm{stat}) \pm 0.9\ \mathrm{syst}$ nb [99]. It should be noted that the LHCb measurement was done for rapidity $2 < y < 4.5$, while the ALICE measurement was done for $2.5 < y < 4$.

To compare the results, the differential cross sections $\frac{\mathrm{d}\sigma}{\mathrm{d}y}$ were computed for both measurements. Additionally, the contamination from $b\bar{b}$ pairs estimated in Section 6.5 was subtracted from the ALICE cross section. The rapidity differential cross sections are then $5.5 \pm 1.5\ (\mathrm{stat}) \pm 0.8\ (\mathrm{syst})$ nb and $6.1 \pm 0.4\ (\mathrm{stat}) \pm 0.4\ (\mathrm{syst})$ nb for the ALICE and LHCb measurement respectively. Although the uncertainties on the ALICE value are larger, the measurements agree well with each other.

6.8 Outlook

The measurement of di-J/ψ production demonstrates the feasibility of such measurements in ALICE. However, it is clear that a larger integrated luminosity is necessary in order to derive meaningful conclusions on DPS contributions. In December of 2018, the LHC Run-2 came to an end, and the accelerator was stopped. This period where no collisions take place is called the Long Shutdown 2 (LS2), and it was devoted to the preparation of the LHC Run-3. During LS2, each of the experiments planned upgrades to their detectors and the LHC accelerator itself was upgraded as well. In LHC Run-3, the target integrated luminosity of ALICE for pp collisions at $\sqrt{s} = 13\,\mathrm{TeV}$ is

$200\ \mathrm{pb}^{-1}$ [157]. This represents an increase of a factor 8 with respect to the current dataset. With the larger integrated luminosity, it could become possible to perform the measurement differentially as a function of Δp_{T} or Δy between the two J/ψ. The production cross section versus Δy is important in order to separate SPS from DPS contributions. Furthermore, with the ability to reconstruct J/ψ (through the electron decay channel) in the central barrel, ALICE has the unique capability at the LHC to study simultaneous mid and forward J/ψ pair production. This allows to probe large Δy, where DPS contributions dominate.

In preparation of LHC Run-3, the ALICE detector has been upgraded. A new detector called the Muon Forward Tracker (MFT), has been installed, which was designed to improve the vertexing capabilities of the Muon Spectrometer [158]. With the MFT it will be possible to separate prompt and non-prompt contributions, as the latter occur with displaced vertices. As such, the prompt J/ψ pair production will be able to be measured directly, instead of through corrections to the inclusive cross section.

Chapter 7

Conclusions

The Quark-Gluon Plasma is a rich studying ground for properties of QCD under extreme conditions. In order to recognize features of the QGP, it is necessary to have a firm grip on QCD phenomena that do not involve a hot and dense medium. For example, parton distribution functions are known to be different in nuclei than in free protons and neutrons, leading to nuclear parton distribution functions (nPDFs). The nPDFs form the building blocks of theoretical calculations involving hard processes, which are processes that occur with large momentum transfer. By convoluting the parton distributions with the partonic cross sections, our understanding of QCD can be tested to a high degree. While partonic cross sections for hard processes can be computed using perturbative QCD, the nPDFs are non-perturbative objects and therefore cannot be determined from first principles. Instead, they are obtained through global fits to data. Because Z bosons and their decay muons do not carry color charge, they do not interact with the QGP formed in central Pb–Pb collisions and are therefore not sensitive to strong final state effects. Their production can consequently be used to constrain nPDFs, which describe modifications to the initial state.

In this thesis, the production of Z bosons in Pb–Pb collisions at a center-of-mass energy of $\sqrt{s_{\mathrm{NN}}} = 5.02\,\mathrm{TeV}$ was measured. The Z bosons were reconstructed in their dimuon decay channels, with transverse momentum ${p_{\mathrm{T}}}^{\mu} > 20$ GeV/c, pseudorapidity $2.5 < \eta^{\mu} < 4.0$, dimuon rapidity $2.5 < y_{\mu\mu} < 4.0$ and dimuon invariant mass $60 < m_{\mu\mu} < 120$ GeV/c^2. The invariant yield, normalised by the nuclear overlap function $\langle T_{\mathrm{AA}} \rangle$ was computed, as well as the nuclear modification factor R_{AA}, which quantifies deviations in production between AA and pp collisions. The normalised invariant yield was determined integrated over rapidity and event centrality, and also as a function of each. The data were compared with theoretical models, both those including nPDFs and those with free-nucleon PDFs. The data show a clear and strong preference for nPDF calculations, which describe them well. In contrast, a $3.4\ \sigma$ deviation from the free-nucleon predictions was found in the integrated invariant yield. The observed deviation is larger than the $2.3\ \sigma$ deviation found in a previous ALICE publication on Z bosons, on a subset of the current data sample. The yield as a function of rapidity shows an increasing preference for nPDF models as the rapidity grows. This is attributed to the shadowing effect, which is more pronounced at forward rapidity where lower values of bjorken-x

are probed. The results obtained in ALICE are therefore complementary to those obtained in ATLAS and CMS, where large bjorken-x are probed at midrapidity. Additionally, the data serve as a test of features of nPDFs such as their universality. Lastly, the yield as a function of centrality can be used to test assumptions in the Glauber Monte Carlo framework. The latter is used to determine event properties such as centrality, the number of binary collisons $\langle N_{\mathrm{coll}} \rangle$, and the number of nucleons that undergo at least one scattering $\langle N_{\mathrm{part}} \rangle$. Z bosons can only be created in the initial hard scatterings, so that their production should scale with $\langle N_{\mathrm{coll}} \rangle$. The normalised invariant yield should therefore not depend on the centrality of the event. Within uncertainties, it was indeed found to be constant.

Starting from LHC Run-3 in 2022, the readout of the ALICE detector will be improved to be able to handle a 50 kHz interaction rate in Pb–Pb collisions (it was 7.5 kHz in Run-2). The integrated luminosity in Run-3 and Run-4 combined will be roughly 10 times larger than the current Pb–Pb dataset. The higher integrated luminosity will allow for measurements with much better precision than currently accessible, which in turn will lead to stronger constraining power in the nPDF fits. In addition to collisions involving Pb–nuclei, heavy-ion data taking involving oxygen nuclei are also programmed for Run-3. The interest in such runs in the context of nPDFs comes from the fact that at high energy, most data in nPDF fits involve Pb–nuclei, as they come from the LHC. Due to a lack of data from lighter ions at high energy, the dependence on the atomic mass A of nPDFs is not well understood. Measurements of Z bosons in lighter ion collisions could therefore be valuable to constrain it. To estimate the experimental feasibility of such measurements, projections were made for Z-boson production in p–O collisions at $\sqrt{s_{\mathrm{NN}}} = 9\,\mathrm{TeV}$ and O–O collisions at $\sqrt{s_{\mathrm{NN}}} = 6.37\,\mathrm{TeV}$. With the expected luminosity, measurements in both systems were found to be unfeasible. However, an increase in the allotted time for the oxygen runs could make measurements attainable.

In recent times, signs of collective behavior typically associated with the QGP have been observed in high-multiplicity pp and pA collisions. The origin of this behavior is not yet well understood. One possible explanation is the formation of small QGP droplets. Another potential origin for the observed collectivity are multi-parton interactions (MPI). Such MPI could be indirectly observed in the production of J/ψ pairs, which contain contributions from single parton scatterings as well as multiple parton scatterings. In particular, double parton contributions (DPS) are expected to be non-negligible at LHC energies. J/ψ pair production is also useful to understand single J/ψ production, where current measurements and calculations of differential cross sections and polarisation prevent conclusive statements regarding dominant production modes. Associated quarkonium production such as J/ψ pair production are considered promising tools to disentangle the various single J/ψ production models.

In this thesis, a measurement of the di-J/ψ cross section in pp collisions at $\sqrt{s_{\mathrm{NN}}} = 13\,\mathrm{TeV}$ was presented. The analysis was done on a data sample with an integrated luminosity of $\mathcal{L} = 24.38 \pm 0.01\ (\mathrm{stat}) \pm 0.87\ (\mathrm{syst})\mathrm{pb}^{-1}$. The J/$\psi$ were reconstructed in their dimuon decay channels, with dimuon rapidity $2.5 < y_{\mu\mu} < 4.0$. At the moment, the Muon Spectrometer does not allow for a separation between prompt and non-prompt contributions, so that the inclusive cross section was measured to be $10.2 \pm 2.3\ (\mathrm{stat}) \pm 1.1\ (\mathrm{syst})\ \mathrm{nb}$. By estimating non-prompt contributions

using simulations, the prompt differential J/ψ pair production cross section $\frac{\mathrm{d}\sigma}{\mathrm{d}y} = 5.5 \pm 1.5\ (\mathrm{stat}) \pm 0.8\ (\mathrm{syst})$ was obtained. This result is in good agreement with the value of $\frac{\mathrm{d}\sigma}{\mathrm{d}y} = 6.1 \pm 0.4\ (\mathrm{stat}) \pm 0.4\ (\mathrm{syst})$ found in LHCb. This is the first time that the inclusive di-J/ψ cross section has been measured in ALICE.

Thanks to the addition of the Muon Forward tracker in Run-3, it will be possible to directly measure the prompt di-J/ψ production. Moreover, the integrated luminosity of pp collisions is expected to increase by a factor of 8, which will allow for a measurement with much better experimental precision. With the increased luminosity, the cross section as a function of the rapidity difference between the two J/ψ can then be measured. This will help to distinguish SPS from DPS contributions, as the latter are expected to dominate at large Δy.

Appendix A

Fit functions and parameters

A.1 Signal function

The J/ψ and $\psi(2S)$ functions were fitted with a Double Crystal Ball (also known as an extended Crystal Ball) function. The function consists of a gaussian core with mean $\bar{x}$ and standard deviation σ, with exponential tails on the left and right of the core. Each tail is characterised by a power n_i, and an α_i that describes how far away from the gaussian core the tail begins. The function is defined as

$$f = N \begin{cases} A\left(B - \frac{x-\bar{x}}{\sigma}\right)^{-n_1} & \text{for } \frac{x-\bar{x}}{\sigma} \leq -\alpha_1 \\ \exp\left(\frac{-(x-\bar{x})^2}{2\sigma^2}\right) & \text{for } -\alpha_1 < \frac{x-\bar{x}}{\sigma} < \alpha_2 \\ C\left(D + \frac{x-\bar{x}}{\sigma}\right)^{-n_2} & \text{for } \frac{x-\bar{x}}{\sigma} \geq \alpha_2 \end{cases} \tag{A.1}$$

where N is a normalisation factor and

$$\begin{aligned} A &= \left(\frac{n_1}{\alpha_1}\right)^{n_1} \exp\left(-\frac{\alpha_1^2}{2}\right), \quad B = \frac{n_1}{\alpha_1} - \alpha_1 \\ C &= \left(\frac{n_2}{\alpha_2}\right)^{n_2} \exp\left(-\frac{\alpha_2^2}{2}\right), \quad D = \frac{n_2}{\alpha_2} - \alpha_2. \end{aligned}$$

The parameters are defined such that $\alpha_1, n_1, \alpha_2, n_2 > 0$.

A.1.1 Tail parameters

In order to improve fit stability, the tail parameters of the CB2 functions were always fixed. The values of the tail parameters were taken from another analysis [153]. Two sets were available: one extracted from the integrated Run-2 invariant mass spectrum, and another one extracted from MC simulations. The tail parameters of the two

sets are presented in Table A.1.

	13 TeV pp data	13 TeV MC
α_1	0.883	0.993
n_1	9.940	2.9075
α_2	1.832	2.182
n_2	15.323	3.122

Table A.1: Two sets of tail parameters for the CB2 function. Values taken from [153].

A.2 Background functions

Various functions were used to describe the combinatorial background. These are the **exponential of 2nd order polynomial** given by

$$N \exp\left(Ax + Bx^2\right), \tag{A.2}$$

a **ratio of first over second order polynomial** given by

$$N \frac{1 + Ax}{Bx + Cx^2}, \tag{A.3}$$

and **double exponential** given by

$$N \left(\exp\left(Ax\right) + B \exp\left(Cx\right)\right). \tag{A.4}$$

For all three functions, N represents the normalisation, while A, B, and C are the function parameters.

Bibliography

[1] https://en.wikipedia.org/wiki/File:Standard_Model_of_Elementary_Particles.svg.

[2] **Particle Data Group** Collaboration, P. A. Zyla *et al.*, "Review of Particle Physics," *PTEP* **2020** no. 8, (2020) 083C01.

[3] P. Foka and M. A. Janik, "An overview of experimental results from ultra-relativistic heavy-ion collisions at the CERN LHC: Bulk properties and dynamical evolution," *Rev. Phys.* **1** (2016) 154–171, arXiv:1702.07233 [hep-ex].

[4] M. L. Miller, K. Reygers, S. J. Sanders, and P. Steinberg, "Glauber modeling in high energy nuclear collisions," *Ann. Rev. Nucl. Part. Sci.* **57** (2007) 205–243, arXiv:nucl-ex/0701025.

[5] W. Busza, K. Rajagopal, and W. van der Schee, "Heavy Ion Collisions: The Big Picture, and the Big Questions," *Ann. Rev. Nucl. Part. Sci.* **68** (2018) 339–376, arXiv:1802.04801 [hep-ph].

[6] M. Strickland, "Anisotropic Hydrodynamics: Three lectures," *Acta Phys. Polon. B* **45** no. 12, (2014) 2355–2394, arXiv:1410.5786 [nucl-th].

[7] **ALICE** Collaboration, K. Aamodt *et al.*, "Two-pion Bose-Einstein correlations in central Pb-Pb collisions at $\sqrt{s_{NN}} = 2.76$ TeV," *Phys. Lett. B* **696** (2011) 328–337, arXiv:1012.4035 [nucl-ex].

[8] R. Pasechnik and M. Šumbera, "Phenomenological Review on Quark–Gluon Plasma: Concepts vs. Observations," *Universe* **3** no. 1, (2017) 7, arXiv:1611.01533 [hep-ph].

[9] **CMS** Collaboration, V. Khachatryan *et al.*, "Observation of Long-Range Near-Side Angular Correlations in Proton-Proton Collisions at the LHC," *JHEP* **09** (2010) 091, arXiv:1009.4122 [hep-ex].

[10] **ATLAS, ALICE, CMS, LHCb** Collaboration, A. Ohlson, "Ridges in p–A (and pp) collisions," in *3rd Large Hadron Collider Physics Conference*. Kurchatov Institute, Gatchina, 2016. arXiv:1901.00747 [nucl-ex].

[11] **ALICE** Collaboration, J. Adam *et al.*, "Enhanced production of multi-strange hadrons in high-multiplicity proton-proton collisions," *Nature Phys.* **13** (2017) 535–539, arXiv:1606.07424 [nucl-ex].

[12] **CMS** Collaboration, V. Khachatryan *et al.*, "Observation of Long-Range Near-Side Angular Correlations in Proton-Proton Collisions at the LHC," *JHEP* **09** (2010) 091, arXiv:1009.4122 [hep-ex].

[13] A. Ortiz, A. Paz, J. D. Romo, S. Tripathy, E. A. Zepeda, and I. Bautista, "Multiparton interactions in pp collisions from machine learning-based regression," *Phys. Rev. D* **102** no. 7, (2020) 076014, arXiv:2004.03800 [hep-ph].

[14] J. L. Nagle and W. A. Zajc, "Small System Collectivity in Relativistic Hadronic and Nuclear Collisions," *Ann. Rev. Nucl. Part. Sci.* **68** (2018) 211–235, arXiv:1801.03477 [nucl-ex].

[15] K. Kovařík, P. M. Nadolsky, and D. E. Soper, "Hadronic structure in high-energy collisions," *Rev. Mod. Phys.* **92** no. 4, (2020) 045003, arXiv:1905.06957 [hep-ph].

[16] J. C. Collins, D. E. Soper, and G. F. Sterman, "Factorization of Hard Processes in QCD," *Adv. Ser. Direct. High Energy Phys.* **5** (1989) 1–91, arXiv:hep-ph/0409313.

[17] Y. L. Dokshitzer, "Calculation of the Structure Functions for Deep Inelastic Scattering and e+ e- Annihilation by Perturbation Theory in Quantum Chromodynamics.," *Sov. Phys. JETP* **46** (1977) 641–653.

[18] V. N. Gribov and L. N. Lipatov, "Deep inelastic e p scattering in perturbation theory," *Sov. J. Nucl. Phys.* **15** (1972) 438–450.

[19] L. N. Lipatov, "The parton model and perturbation theory," *Yad. Fiz.* **20** (1974) 181–198.

[20] G. Altarelli and G. Parisi, "Asymptotic Freedom in Parton Language," *Nucl. Phys. B* **126** (1977) 298–318.

[21] T.-J. Hou *et al.*, "New CTEQ global analysis of quantum chromodynamics with high-precision data from the LHC," *Phys. Rev. D* **103** no. 1, (2021) 014013, arXiv:1912.10053 [hep-ph].

[22] E. Iancu and R. Venugopalan, *The Color glass condensate and high-energy scattering in QCD*. 3, 2003. arXiv:hep-ph/0303204.

[23] J. Jalilian-Marian, A. Kovner, A. Leonidov, and H. Weigert, "The BFKL equation from the Wilson renormalization group," *Nucl. Phys. B* **504** (1997) 415–431, arXiv:hep-ph/9701284.

[24] F. Gelis, E. Iancu, J. Jalilian-Marian, and R. Venugopalan, "The Color Glass Condensate," *Ann. Rev. Nucl. Part. Sci.* **60** (2010) 463–489, arXiv:1002.0333 [hep-ph].

[25] V. A. Novikov, L. B. Okun, A. N. Rozanov, and M. I. Vysotsky, "Theory of Z boson decays," *Rept. Prog. Phys.* **62** (1999) 1275–1332, arXiv:hep-ph/9906465.

[26] S. A. Bludman, "The First gauge theory of weak interactions and the prediction of weak neutral currents," in *3rd International Symposium on the History of Particle Physics: The Rise of the Standard Model*. 6, 1992. arXiv:hep-ph/9212232.

[27] J. Swain, "Electroweak couplings, lepton universality, and the origin of mass: An experimental perspective," *PoS* **silafae-III** (2000) 036.

[28] **ALEPH, DELPHI, L3, OPAL, LEP Electroweak** Collaboration, S. Schael *et al.*, "Electroweak Measurements in Electron-Positron Collisions at W-Boson-Pair Energies at LEP," *Phys. Rept.* **532** (2013) 119–244, arXiv:1302.3415 [hep-ex].

[29] J. Anderson, M. Boonekamp, H. Burkhardt, M. Dittmar, V. Halyo, and T. C. Petersen, "Proton proton luminosity, standard candles and PDFs at the LHC," in *HERA and the LHC: 4th Workshop on the Implications of HERA for LHC Physics*. 3, 2009.

[30] **LHCb** Collaboration, R. Aaij *et al.*, "Measurement of the forward Z boson production cross-section in pp collisions at $\sqrt{s} = 13$ TeV," *JHEP* **09** (2016) 136, arXiv:1607.06495 [hep-ex].

[31] **ATLAS** Collaboration, G. Aad *et al.*, "Measurement of $W^{\pm}$ and Z-boson production cross sections in pp collisions at $\sqrt{s} = 13$ TeV with the ATLAS detector," *Phys. Lett. B* **759** (2016) 601–621, arXiv:1603.09222 [hep-ex].

[32] J.-C. Peng and J.-W. Qiu, "The Drell-Yan Process," *The Universe* **4** no. 3, (2016) 34–44.

[33] https://feynman.aivazis.com.

[34] R. Bonciani, F. Buccioni, N. Rana, I. Triscari, and A. Vicini, "NNLO QCD$\times$EW corrections to Z production in the $q\bar{q}$ channel," *Phys. Rev. D* **101** no. 3, (2020) 031301, arXiv:1911.06200 [hep-ph].

[35] S. Amoroso *et al.*, "Les Houches 2019: Physics at TeV Colliders: Standard Model Working Group Report," in *11th Les Houches Workshop on Physics at TeV Colliders: PhysTeV Les Houches*. 3, 2020. arXiv:2003.01700 [hep-ph].

[36] **CMS** Collaboration, A. M. Sirunyan *et al.*, "Measurement of the differential Drell-Yan cross section in proton-proton collisions at $\sqrt{s}$ = 13 TeV," *JHEP* **12** (2019) 059, arXiv:1812.10529 [hep-ex].

[37] A. Khare, "The November J / psi revolution: Twenty five years later," *Curr. Sci.* **77** (1999) 1210, arXiv:hep-ph/9910468.

[38] L. Maiani, "The GIM Mechanism: origin, predictions and recent uses," in *48th Rencontres de Moriond on Electroweak Interactions and Unified Theories*. 3, 2013. arXiv:1303.6154 [hep-ph].

[39] J. L. Rosner, "The Arrival of charm," *AIP Conf. Proc.* **459** no. 1, (1999) 9–27, arXiv:hep-ph/9811359.

[40] V. Mateu, P. G. Ortega, D. R. Entem, and F. Fernández, "Calibrating the Naïve Cornell Model with NRQCD," *Eur. Phys. J. C* **79** no. 4, (2019) 323, arXiv:1811.01982 [hep-ph].

[41] P. Faccioli, C. Lourenco, J. Seixas, and H. K. Wohri, "Towards the experimental clarification of quarkonium polarization," *Eur. Phys. J. C* **69** (2010) 657–673, arXiv:1006.2738 [hep-ph].

[42] J.-P. Lansberg, "New Observables in Inclusive Production of Quarkonia," *Phys. Rept.* **889** (2020) 1–106, arXiv:1903.09185 [hep-ph].

[43] **D0** Collaboration, V. M. Abazov *et al.*, "Observation and Studies of Double J/ψ Production at the Tevatron," *Phys. Rev. D* **90** no. 11, (2014) 111101, arXiv:1406.2380 [hep-ex].

[44] "Measurement of the differential non-prompt J/ψ production fraction in $\sqrt{}$s = 13 TeV pp collisions at the ATLAS experiment,".

[45] **CDF** Collaboration, D. Acosta *et al.*, "Measurement of the J/ψ meson and $b-$hadron production cross sections in $p\bar{p}$ collisions at $\sqrt{s} = 1960$ GeV," *Phys. Rev. D* **71** (2005) 032001, arXiv:hep-ex/0412071.

[46] J. P. Lansberg, "J/ψ, ψ ' and Υ production at hadron colliders: A Review," *Int. J. Mod. Phys. A* **21** (2006) 3857–3916, arXiv:hep-ph/0602091.

[47] N. Brambilla *et al.*, "Heavy Quarkonium: Progress, Puzzles, and Opportunities," *Eur. Phys. J. C* **71** (2011) 1534, arXiv:1010.5827 [hep-ph].

[48] G. T. Bodwin, E. Braaten, and J. Lee, "Comparison of the color-evaporation model and the NRQCD factorization approach in charmonium production," *Phys. Rev. D* **72** (2005) 014004, arXiv:hep-ph/0504014.

[49] Y. Fan, Y.-Q. Ma, and K.-T. Chao, "Relativistic Correction to J/psi Production at Hadron Colliders," *Phys. Rev. D* **79** (2009) 114009, arXiv:0904.4025 [hep-ph].

[50] E. Chapon *et al.*, "Perspectives for quarkonium studies at the high-luminosity LHC," arXiv:2012.14161 [hep-ph].

[51] A. V. Berezhnoy, A. K. Likhoded, A. V. Luchinsky, and A. A. Novoselov, "Double J/psi-meson Production at LHC and 4c-tetraquark state," *Phys. Rev. D* **84** (2011) 094023, arXiv:1101.5881 [hep-ph].

[52] J.-P. Lansberg and H.-S. Shao, "J/ψ -pair production at large momenta: Indications for double parton scatterings and large α_s^5 contributions," *Phys. Lett. B* **751** (2015) 479–486, arXiv:1410.8822 [hep-ph].

[53] J.-P. Lansberg, C. Pisano, F. Scarpa, and M. Schlegel, "Pinning down the linearly-polarised gluons inside unpolarised protons using quarkonium-pair production at the LHC," *Phys. Lett. B* **784** (2018) 217–222, arXiv:1710.01684 [hep-ph]. [Erratum: Phys.Lett.B 791, 420–421 (2019)].

[54] A. Szczurek and R. Maciula, "Production of one and two $c\bar{c}$ pairs at LHC," *AIP Conf. Proc.* **1523** no. 1, (2013) 255–259, arXiv:1212.5427 [hep-ph].

[55] J.-P. Lansberg, H.-S. Shao, N. Yamanaka, Y.-J. Zhang, and C. Noûs, "Complete NLO QCD study of single- and double-quarkonium hadroproduction in the colour-evaporation model at the Tevatron and the LHC," *Phys. Lett. B* **807** (2020) 135559, arXiv:2004.14345 [hep-ph].

[56] J. P. Lansberg, "On the mechanisms of heavy-quarkonium hadroproduction," *Eur. Phys. J. C* **61** (2009) 693–703, arXiv:0811.4005 [hep-ph].

[57] J. R. Gaunt, C.-H. Kom, A. Kulesza, and W. J. Stirling, "Same-sign W pair production as a probe of double parton scattering at the LHC," *Eur. Phys. J. C* **69** (2010) 53–65, arXiv:1003.3953 [hep-ph].

[58] **D0** Collaboration, V. M. Abazov *et al.*, "Observation and Studies of Double J/ψ Production at the Tevatron," *Phys. Rev. D* **90** no. 11, (2014) 111101, arXiv:1406.2380 [hep-ex].

[59] **CMS** Collaboration, S. Chatrchyan *et al.*, "Study of Double Parton Scattering Using W + 2-Jet Events in Proton-Proton Collisions at $\sqrt{s}$ = 7 TeV," *JHEP* **03** (2014) 032, arXiv:1312.5729 [hep-ex].

[60] M. Diehl and J. R. Gaunt, "Double parton scattering theory overview," *Adv. Ser. Direct. High Energy Phys.* **29** (2018) 7–28, arXiv:1710.04408 [hep-ph].

[61] M. Rinaldi, S. Scopetta, and V. Vento, "Double parton correlations in constituent quark models," *Phys. Rev. D* **87** (2013) 114021, arXiv:1302.6462 [hep-ph].

[62] D. F. Geesaman, K. Saito, and A. W. Thomas, "The nuclear EMC effect," *Ann. Rev. Nucl. Part. Sci.* **45** (1995) 337–390.

[63] K. J. Eskola, P. Paakkinen, H. Paukkunen, and C. A. Salgado, "EPPS16: Nuclear parton distributions with LHC data," *Eur. Phys. J. C* **77** no. 3, (2017) 163, arXiv:1612.05741 [hep-ph].

[64] K. Kovarik *et al.*, "nCTEQ15 - Global analysis of nuclear parton distributions with uncertainties in the CTEQ framework," *Phys. Rev. D* **93** no. 8, (2016) 085037, arXiv:1509.00792 [hep-ph].

[65] K. J. Eskola, H. Paukkunen, and C. A. Salgado, "EPS09: A New Generation of NLO and LO Nuclear Parton Distribution Functions," *JHEP* **04** (2009) 065, arXiv:0902.4154 [hep-ph].

[66] S. J. Brodsky, I. Schmidt, and J.-J. Yang, "Nuclear antishadowing in neutrino deep inelastic scattering," *Phys. Rev. D* **70** (2004) 116003, arXiv:hep-ph/0409279.

[67] A. W. Thomas, "Reflections on the Origin of the EMC Effect," *Int. J. Mod. Phys. E* **27** no. 12, (2019) 1840001, arXiv:1809.06622 [hep-ph].

[68] N. Armesto, "Nuclear shadowing," *J. Phys. G* **32** (2006) R367–R394, arXiv:hep-ph/0604108.

[69] A. Kusina, J.-P. Lansberg, I. Schienbein, and H.-S. Shao, "Reweighted nuclear PDFs using Heavy-Flavor Production Data at the LHC: nCTEQ15$_{rwHF}$ & EPPS16$_{rwHF}$," arXiv:2012.11462 [hep-ph].

[70] I. Helenius, K. J. Eskola, H. Honkanen, and C. A. Salgado, "Impact-Parameter Dependent Nuclear Parton Distribution Functions: EPS09s and EKS98s and Their Applications in Nuclear Hard Processes," *JHEP* **07** (2012) 073, arXiv:1205.5359 [hep-ph].

[71] S. Dulat, T.-J. Hou, J. Gao, M. Guzzi, J. Huston, P. Nadolsky, J. Pumplin, C. Schmidt, D. Stump, and C. P. Yuan, "New parton distribution functions from a global analysis of quantum chromodynamics," *Phys. Rev. D* **93** no. 3, (2016) 033006, arXiv:1506.07443 [hep-ph].

[72] A. Kusina *et al.*, "Impact of LHC vector boson production in heavy ion collisions on strange PDFs," *Eur. Phys. J. C* **80** no. 10, (2020) 968, arXiv:2007.09100 [hep-ph].

[73] H. Khanpour and S. Atashbar Tehrani, "Global Analysis of Nuclear Parton Distribution Functions and Their Uncertainties at Next-to-Next-to-Leading Order," *Phys. Rev. D* **93** no. 1, (2016) 014026, arXiv:1601.00939 [hep-ph].

[74] H. Khanpour, M. Soleymaninia, S. Atashbar Tehrani, H. Spiesberger, and V. Guzey, "Nuclear parton distribution functions with uncertainties in the general mass variable flavor number scheme," arXiv:2010.00555 [hep-ph].

[75] **NNPDF** Collaboration, R. Abdul Khalek, J. J. Ethier, and J. Rojo, "Nuclear parton distributions from lepton-nucleus scattering and the impact of an electron-ion collider," *Eur. Phys. J. C* **79** no. 6, (2019) 471, arXiv:1904.00018 [hep-ph].

[76] M. Walt, I. Helenius, and W. Vogelsang, "Open-source QCD analysis of nuclear parton distribution functions at NLO and NNLO," *Phys. Rev. D* **100** no. 9, (2019) 096015, arXiv:1908.03355 [hep-ph].

[77] P. Paakkinen, "Nuclear parton distribution functions," arXiv:1802.05927 [hep-ph].

[78] R. Abdul Khalek, J. J. Ethier, J. Rojo, and G. van Weelden, "nNNPDF2.0: quark flavor separation in nuclei from LHC data," *JHEP* **09** (2020) 183, arXiv:2006.14629 [hep-ph].

[79] H. Paukkunen, "Nuclear PDFs Today," *PoS* **HardProbes2018** (2018) 014, arXiv:1811.01976 [hep-ph].

[80] P. Paakkinen, "Constraining npdfs with lhc data – now and in the future." Accessed on 27th of april, 2021. http://llr.in2p3.fr/~fleuret/wikiil/upload/RencontresIonsLourds/Orsay_HI_meeting_nPDFs_Paakkinen.pdf.

[81] J. P. Blaizot, F. Gelis, and R. Venugopalan, "High-energy pA collisions in the color glass condensate approach. 1. Gluon production and the Cronin effect," *Nucl. Phys. A* **743** (2004) 13–56, arXiv:hep-ph/0402256.

[82] **ALICE** Collaboration, B. Abelev *et al.*, "Transverse momentum distribution and nuclear modification factor of charged particles in p-Pb collisions at $\sqrt{s_{NN}} = 5.02$ TeV," *Phys. Rev. Lett.* **110** no. 8, (2013) 082302, arXiv:1210.4520 [nucl-ex].

[83] C. Lourenco, R. Vogt, and H. K. Woehri, "Energy dependence of J/psi absorption in proton-nucleus collisions," *JHEP* **02** (2009) 014, arXiv:0901.3054 [hep-ph].

[84] J. Zhao, K. Zhou, S. Chen, and P. Zhuang, "Heavy flavors under extreme conditions in high energy nuclear collisions," *Prog. Part. Nucl. Phys.* **114** (2020) 103801, arXiv:2005.08277 [nucl-th].

[85] F. Arleo, C.-J. Naïm, and S. Platchkov, "Initial-state energy loss in cold QCD matter and the Drell-Yan process," *JHEP* **01** (2019) 129, arXiv:1810.05120 [hep-ph].

[86] Z. Conesa del Valle, "Vector bosons in heavy-ion collisions at the LHC," *Eur. Phys. J. C* **61** (2009) 729–733, arXiv:0903.1432 [hep-ex].

[87] **ATLAS** Collaboration, M. Aaboud *et al.*, "Observation of centrality-dependent acoplanarity for muon pairs produced via two-photon scattering in Pb+Pb collisions at $\sqrt{s_{\rm NN}} = 5.02$ TeV with the ATLAS detector," *Phys. Rev. Lett.* **121** no. 21, (2018) 212301, arXiv:1806.08708 [nucl-ex].

[88] S. Klein, A. H. Mueller, B.-W. Xiao, and F. Yuan, "Lepton Pair Production Through Two Photon Process in Heavy Ion Collisions," *Phys. Rev. D* **102** no. 9, (2020) 094013, arXiv:2003.02947 [hep-ph].

[89] M. Kłusek-Gawenda, W. Schäfer, and A. Szczurek, "Centrality dependence of dilepton production via $\gamma\gamma$ processes from Wigner distributions of photons in nuclei," *Phys. Lett. B* **814** (2021) 136114, arXiv:2012.11973 [hep-ph].

[90] **ALICE** Collaboration, J. Adam *et al.*, "J/ψ suppression at forward rapidity in Pb-Pb collisions at $\sqrt{\mathbf{s_{\rm NN}}} = \mathbf{5.02}$ TeV," *Phys. Lett. B* **766** (2017) 212–224, arXiv:1606.08197 [nucl-ex].

[91] **ATLAS** Collaboration, M. Aaboud *et al.*, "Measurements of W and Z boson production in pp collisions at $\sqrt{s} = 5.02$ TeV with the ATLAS detector," *Eur. Phys. J. C* **79** no. 2, (2019) 128, arXiv:1810.08424 [hep-ex]. [Erratum: Eur.Phys.J.C 79, 374 (2019)].

[92] **ALICE** Collaboration, J. Adam *et al.*, "W and Z boson production in p-Pb collisions at $\sqrt{s_{\rm NN}}$ = 5.02 TeV," *JHEP* **02** (2017) 077, arXiv:1611.03002 [nucl-ex].

[93] **ALICE** Collaboration, S. Acharya *et al.*, "Z-boson production in p-Pb collisions at $\sqrt{s_{\rm NN}} = 8.16$ TeV and Pb-Pb collisions at $\sqrt{s_{\rm NN}} = 5.02$ TeV," *JHEP* **09** (2020) 076, arXiv:2005.11126 [nucl-ex].

[94] **ALICE** Collaboration, G. Taillepied, "Electroweak-boson production in p-Pb and Pb-Pb collisions at the LHC with ALICE," *PoS* **HardProbes2020** (2020) 112, arXiv:2008.07809 [nucl-ex].

[95] **ALICE** Collaboration, S. Acharya *et al.*, "Measurement of Z^0-boson production at large rapidities in Pb-Pb collisions at $\sqrt{s_{\rm NN}} = 5.02$ TeV," *Phys. Lett. B* **780** (2018) 372–383, arXiv:1711.10753 [nucl-ex].

[96] **LHCb** Collaboration, R. Aaij *et al.*, "Observation of Z production in proton-lead collisions at LHCb," *JHEP* **09** (2014) 030, arXiv:1406.2885 [hep-ex].

[97] **CMS** Collaboration, A. M. Sirunyan *et al.*, "Observation of nuclear modifications in $W^{\pm}$ boson production in pPb collisions at $\sqrt{s_{\rm NN}} = 8.16$ TeV," *Phys. Lett. B* **800** (2020) 135048, arXiv:1905.01486 [hep-ex].

[98] **LHCb** Collaboration, R. Aaij *et al.*, "Observation of structure in the J/ψ -pair mass spectrum," *Sci. Bull.* **65** no. 23, (2020) 1983–1993, arXiv:2006.16957 [hep-ex].

[99] **LHCb** Collaboration, R. Aaij *et al.*, "Measurement of the J/ψ pair production cross-section in pp collisions at $\sqrt{s} = 13$ TeV," *JHEP* **06** (2017) 047, arXiv:1612.07451 [hep-ex]. [Erratum: JHEP 10, 068 (2017)].

[100] **ATLAS** Collaboration, M. Aaboud *et al.*, "Measurement of the prompt J/ ψ pair production cross-section in pp collisions at $\sqrt{s} = 8$ TeV with the ATLAS detector," *Eur. Phys. J. C* **77** no. 2, (2017) 76, arXiv:1612.02950 [hep-ex].

[101] **LHCb** Collaboration, R. Aaij *et al.*, "Observation of J/ψ pair production in pp collisions at $\sqrt{s} = 7TeV$," *Phys. Lett. B* **707** (2012) 52–59, arXiv:1109.0963 [hep-ex].

[102] **LHCb** Collaboration, R. Aaij *et al.*, "Observation of double charm production involving open charm in pp collisions at $\sqrt{s}$ = 7 TeV," *JHEP* **06** (2012) 141, arXiv:1205.0975 [hep-ex]. [Addendum: JHEP 03, 108 (2014)].

[103] **LHCb** Collaboration, R. Aaij *et al.*, "Measurement of the J/ψ pair production cross-section in pp collisions at $\sqrt{s} = 13$ TeV," *JHEP* **06** (2017) 047, arXiv:1612.07451 [hep-ex]. [Erratum: JHEP 10, 068 (2017)].

[104] **ATLAS** Collaboration, G. Aad *et al.*, "Observation of a new particle in the search for the Standard Model Higgs boson with the ATLAS detector at the LHC," *Phys. Lett. B* **716** (2012) 1–29, arXiv:1207.7214 [hep-ex].

[105] **CMS** Collaboration, S. Chatrchyan *et al.*, "Observation of a New Boson at a Mass of 125 GeV with the CMS Experiment at the LHC," *Phys. Lett. B* **716** (2012) 30–61, arXiv:1207.7235 [hep-ex].

[106] L. Evans and P. Bryant, "LHC Machine," *JINST* **3** (2008) S08001.

[107] C. Salgado *et al.*, "Proton-Nucleus Collisions at the LHC: Scientific Opportunities and Requirements," *J. Phys. G* **39** (2012) 015010, arXiv:1105.3919 [hep-ph].

[108] M. Schaumann *et al.*, "First Xenon-Xenon Collisions in the LHC," in *9th International Particle Accelerator Conference*, p. MOPMF039. 2018.

[109] M. Tarhini, *Measurement of Z-boson and J/ψ Production in p-Pb and Pb-Pb Collisions at $\sqrt{s_{\rm NN}}$ = 5.02 TeV with ALICE at the LHC*. Theses, Université Paris-Saclay, June, 2017. https://tel.archives-ouvertes.fr/tel-01691725.

[110] https://home.cern/resources/faqs/facts-and-figures-about-lhc, Accessed on May 15th, 2020.

[111] https://home.cern/science/engineering/pulling-together-superconducting-electromagnets, Accessed on May 15th, 2020.

[112] https://www.lhc-closer.es/taking_a_closer_look_at_lhc/0.buckets_and_bunches, Accessed on Aug 11th, 2020.

[113] M. Ferro-Luzzi, W. Herr, and T. Pieloni, "LHC bunch filling schemes for commissioning and initial luminosity optimization," Tech. Rep. LHC-Project-Note-415. CERN-LHC-Project-Note-415, CERN, Geneva, Jun, 2008. http://cds.cern.ch/record/1114612.

[114] J. Jowett *et al.*, "The 2018 heavy-ion run of the LHC," in *10th International Particle Accelerator Conference*, p. WEYYPLM2. 2019.

[115] https://lpc.web.cern.ch/fillingschemes.htm, Accessed on Aug 11th, 2020.

[116] **ALICE** Collaboration, K. Aamodt *et al.*, "The ALICE experiment at the CERN LHC," *JINST* **3** (2008) S08002.

[117] **ALICE** Collaboration, B. B. Abelev *et al.*, "Performance of the ALICE Experiment at the CERN LHC," *Int. J. Mod. Phys.* **A29** (2014) 1430044, arXiv:1402.4476 [nucl-ex].

[118] *The forward muon spectrometer of ALICE: addendum to the technical proposal for a Large Ion Collider experiment at the CERN LHC*. LHC Tech. Proposal. CERN, Geneva, 1996. http://cds.cern.ch/record/314011.

[119] **ALICE** Collaboration, *ALICE dimuon forward spectrometer: Technical Design Report*. Technical Design Report ALICE. CERN, Geneva, 1999. http://cds.cern.ch/record/401974.

[120] **ALICE** Collaboration, *ALICE dimuon forward spectrometer: addendum to the Technical Design Report*. Technical Design Report ALICE. CERN, Geneva, 2000. http://cds.cern.ch/record/494265.

[121] **ALICE** Collaboration, J. Adam *et al.*, "Centrality dependence of the charged-particle multiplicity density at midrapidity in Pb-Pb collisions at $\sqrt{s_{\rm NN}}$ = 5.02 TeV," *Phys. Rev. Lett.* **116** no. 22, (2016) 222302, arXiv:1512.06104 [nucl-ex].

[122] L. Betev *et al.*, "Definition of the ALICE Coordinate System and basic rules for Sub-Detector Components numbering." ALICE-INT-2003-038. http://edms.cern.ch/document/406391.

[123] C. Finck and A. M. S. collaboration, "The muon spectrometer of the ALICE," *Journal of Physics: Conference Series* **50** (Nov, 2006) 397–401. https://doi.org/10.1088%2F1742-6596%2F50%2F1%2F056.

[124] https://twiki.cern.ch/twiki/bin/viewauth/ALICE/MuonTracking.

[125] M. Brice, "Installation of the ALICE dipole magnet. Mise en place définitive du dipôle du spectromètre à muons pour l'experience ALICE.," May, 2005. http://cds.cern.ch/record/835416.

[126] M. Gagliardi, *The ALICE muon spectrometer: trigger detectors and quarkonia detection in p-p collisions*. PhD thesis, 2007. https://cds.cern.ch/record/1322409. Presented on Jul 2007.

[127] **Particle Data Group** Collaboration, M. Tanabashi *et al.*, "Review of Particle Physics," *Phys. Rev. D* **98** no. 3, (2018) 030001.

[128] R. Brun, F. Bruyant, M. Maire, A. C. McPherson, and P. Zanarini, *GEANT 3: user's guide Geant 3.10, Geant 3.11; rev. version*. CERN, Geneva, 1987. https://cds.cern.ch/record/1119728.

[129] T. Sjostrand, S. Mrenna, and P. Z. Skands, "A Brief Introduction to PYTHIA 8.1" *Comput. Phys. Commun.* **178** (2008) 852–867, arXiv:0710.3820 [hep-ph].

[130] S. Alioli, P. Nason, C. Oleari, and E. Re, "NLO vector-boson production matched with shower in POWHEG," *JHEP* **07** (2008) 060, arXiv:0805.4802 [hep-ph].

[131] T. Sjostrand, S. Mrenna, and P. Z. Skands, "PYTHIA 6.4 Physics and Manual," *JHEP* **05** (2006) 026, arXiv:hep-ph/0603175.

[132] **CMS** Collaboration, S. Chatrchyan *et al.*, "Study of Z production in PbPb and pp collisions at $\sqrt{s_{\mathrm{NN}}} = 2.76$ TeV in the dimuon and dielectron decay channels," *JHEP* **03** (2015) 022, arXiv:1410.4825 [nucl-ex].

[133] **ALICE Collaboration** Collaboration, "Centrality determination in heavy ion collisions,". https://cds.cern.ch/record/2636623.

[134] H. Paukkunen, private communication.

[135] M. Cacciari, S. Frixione, and P. Nason, "The p(T) spectrum in heavy flavor photoproduction," *JHEP* **03** (2001) 006, arXiv:hep-ph/0102134.

[136] **ALICE** Collaboration, B. Abelev *et al.*, "Centrality determination of Pb-Pb collisions at $\sqrt{s_{NN}}$ = 2.76 TeV with ALICE," *Phys. Rev. C* **88** no. 4, (2013) 044909, arXiv:1301.4361 [nucl-ex].

[137] O. Bugnon, private communication.

[138] P. Pillot, private communication.

[139] R. Boughezal, J. M. Campbell, R. K. Ellis, C. Focke, W. Giele, X. Liu, F. Petriello, and C. Williams, "Color singlet production at NNLO in MCFM," *Eur. Phys. J. C* **77** no. 1, (2017) 7, arXiv:1605.08011 [hep-ph].

[140] R. Gavin, Y. Li, F. Petriello, and S. Quackenbush, "FEWZ 2.0: A code for hadronic Z production at next-to-next-to-leading order," *Comput. Phys. Commun.* **182** (2011) 2388–2403, arXiv:1011.3540 [hep-ph].

[141] A. M. Cooper-Sarkar, "Low-x physics and W and Z production at the LHC," in *4th Les Houches Workshop on Physics at TeV Colliders*. 12, 2005. arXiv:hep-ph/0512228.

[142] **ATLAS** Collaboration, G. Aad *et al.*, "Measurement of $W^{\pm}$ boson production in Pb+Pb collisions at $\sqrt{s_{\mathrm{NN}}} = 5.02$ TeV with the ATLAS detector," *Eur. Phys. J. C* **79** no. 11, (2019) 935, arXiv:1907.10414 [nucl-ex].

[143] **ATLAS** Collaboration, G. Aad *et al.*, "Z boson production in Pb+Pb collisions at $\sqrt{s_{\mathrm{NN}}}$= 5.02 TeV measured by the ATLAS experiment," *Phys. Lett. B* **802** (2020) 135262, arXiv:1910.13396 [nucl-ex].

[144] **CMS** Collaboration, A. M. Sirunyan *et al.*, "High precision measurements of Z boson production in PbPb collisions at $\sqrt{s_{\mathrm{NN}}} = 5.02$ TeV," arXiv:2103.14089 [hep-ex].

[145] **CMS** Collaboration, A. M. Sirunyan *et al.*, "Measurements of differential Z boson production cross sections in proton-proton collisions at $\sqrt{s}$ = 13 TeV," *JHEP* **12** (2019) 061, arXiv:1909.04133 [hep-ex].

[146] dr N. Valle, private communication.

[147] **ALICE** Collaboration, S. Acharya *et al.*, "Analysis of the apparent nuclear modification in peripheral Pb–Pb collisions at 5.02 TeV," *Phys. Lett. B* **793** (2019) 420–432, arXiv:1805.05212 [nucl-ex].

[148] K. J. Eskola, I. Helenius, M. Kuha, and H. Paukkunen, "Shadowing in inelastic nucleon-nucleon cross section?," *Phys. Rev. Lett.* **125** no. 21, (2020) 212301, arXiv:2003.11856 [hep-ph].

[149] **LHCb** Collaboration, R. Aaij *et al.*, "Measurement of the forward Z boson production cross-section in pp collisions at $\sqrt{s} = 7$ TeV," *JHEP* **08** (2015) 039, arXiv:1505.07024 [hep-ex].

[150] **LHCb** Collaboration, R. Aaij *et al.*, "Measurement of forward W and Z boson production in pp collisions at $\sqrt{s} = 8$ TeV," *JHEP* **01** (2016) 155, arXiv:1511.08039 [hep-ex].

[151] S. Catani, L. Cieri, G. Ferrera, D. de Florian, and M. Grazzini, "Vector boson production at hadron colliders: a fully exclusive QCD calculation at NNLO," *Phys. Rev. Lett.* **103** (2009) 082001, arXiv:0903.2120 [hep-ph].

[152] A. Huss, A. Kurkela, A. Mazeliauskas, R. Paatelainen, W. van der Schee, and U. A. Wiedemann, "Discovering partonic rescattering in light nucleus collisions," arXiv:2007.13754 [hep-ph].

[153] M. Guittière, *Etude du ψ(2S) en fonction de la multiplicité de particules chargées dans les collisions proton-proton à $\sqrt{s}$ = 13 TeV au LHC avec le détecteur ALICE : Caractérisation et tests sous faisceau du Muon Forward Tracker d'ALICE*. Theses, Ecole nationale supérieure Mines-Télécom Atlantique, Oct., 2020. https://tel.archives-ouvertes.fr/tel-03064980.

[154] **ALICE Collaboration** Collaboration, "ALICE luminosity determination for pp collisions at $\sqrt{s} = 13$ TeV,". https://cds.cern.ch/record/2160174.

[155] M. L. Mangano, P. Nason, and G. Ridolfi, "Heavy quark correlations in hadron collisions at next-to-leading order," *Nucl. Phys. B* **373** (1992) 295–345.

[156] **LHCb** Collaboration, R. Aaij *et al.*, "Measurement of forward J/ψ production cross-sections in pp collisions at $\sqrt{s} = 13$ TeV," *JHEP* **10** (2015) 172, arXiv:1509.00771 [hep-ex]. [Erratum: JHEP 05, 063 (2017)].

[157] **ALICE Collaboration** Collaboration, "Future high-energy pp programme with ALICE,". https://cds.cern.ch/record/2724925.

[158] "Technical Design Report for the Muon Forward Tracker," tech. rep., Jan, 2015. https://cds.cern.ch/record/1981898.

université PARIS-SACLAY

ÉCOLE DOCTORALE
Particules, hadrons, énergie et noyau : instrumentation, imagerie, cosmos et simulation (PHENIICS)

Titre: Production des bosons Z et du double charme avec ALICE auprès du LHC

Mots clés: LHC, Collisions d'Ions Lourds, Plasma de Quarks et des Gluons, ALICE, Charme

Résumé: Dans la nature, les propriétés de confinement du chromodynamique quantique (QCD) interdisent l'observation de quarks et de gluons libres. Cependant, dans des conditions extrêmes, un état de matière appelé le plasma de quarks et gluons (QGP) dans lequel les quarks et gluons sont déconfinés peut exister. Ce QGP peut être créé et étudié grâce à des collisions entre des noyaux lourds ultra-relativistes. Au Large Hadron Collider (LHC), des collisions entre des noyaux de plomb (Pb) prennent place et sont étudiées dans plusieurs expériences. Cette thèse présente les mesures de la production de bosons Z et de J/ψ reconstruits dans le spectromètre à muons du détecteur ALICE.
Certaines observables dans les collisions PbPb sont impactées par des effets non liés au QGP, effets qu'il est important de décorréler de ceux liés au QGP. Les distributions des partons dans les noyaux (nPDF) qui jouent un rôle important dans de nombreux processus en sont un très bon exemple. Les nPDF constituent un ingrédient crucial pour les calculs des sections efficaces dans des collisions d'ions lourds et elles ne peuvent pas être obtenues par des calculs QCD. Les nPDF sont obtenues par des ajustements aux données de certaines mesures incluant, parmi d'autres, celle des bosons électrofaibles. Ces dernières peuvent donc être utilisées pour contraindre ou vérifier la justesse des nPDFs. Dans cette thèse, la production des bosons Z dans des collisions PbPb à une énergie de 5.02 TeV par paire de nucléons dans le centre de masse avec le détecteur ALICE est détaillée. Les résultats montrent une forte préférence pour les modèles qui incluent des modifications nucléaires dans les PDF. Cela indique que les distributions des partons dans les noyaux ne sont pas des superpositions simples des protons et neutrons.
Dans un avenir proche, des collisions proton-oxygène et oxygène-oxygène prendront place au LHC. Les estimations de la production du boson Z dans ces collisions, obtenues par l'extrapolation des sections efficaces actuelles des expériences ALICE et LHCb sont calculées. Avec la luminosité intégrée attendue pour ces deux systèmes de collision, le mesure apparaît comme impossible.
Dans une collision proton-proton, les particules lourdes comme le J/ψ sont produites dans une collision parton-parton dure et unique (SPS). Il est également possible de créer une paire de J/ψ via ce même processus. La densité des partons augmentant rapidement à hautes énergies, il devient possible que deux diffusions prennent place lors une seule collision pp. Cette double diffusion dure de parton (DPS) constitue un autre mécanisme de génération d'une paire de J/ψ. La production de paires de J/ψ peut par conséquent être utilisée pour étudier les contributions relatives des processus SPS et DPS. Dans cette thèse, une mesure de la section efficace des paires de J/ψ dans des collisions proton-protons à une énergie de 13 TeV par paire de nucléon dans le centre de masse est rapportée pour la première fois dans ALICE. Elle montre, malgré des incertitudes expérimentales importantes, un bon accord avec la section efficace obtenue par la collaboration LHCb. Les futures prises des données au LHC fourniront une statistique plus importante qui permettra de faire une mesure de meilleure précision dans laquelle les contributions SPS et DPS pourraient être séparées.

université PARIS-SACLAY

ÉCOLE DOCTORALE
Particules, hadrons, énergie et noyau : instrumentation, imagerie, cosmos et simulation (PHENIICS)

Title: Z boson and double charm production with ALICE at the LHC

Keywords: LHC, Heavy-Ion collisions, Quark-Gluon Plasma, ALICE, Charm

Abstract: In Nature, free quarks and gluons cannot be observed due to the confinement properties of quantum chromodynamics (QCD). However, in extreme conditions, a state of matter called the Quark-Gluon Plasma (QGP) is formed in which quarks and gluons are deconfined. The QGP can be created and studied by colliding ultrarelativistic heavy nuclei. At the Large Hadron Collider (LHC), collisions between lead (Pb) nuclei take place and are studied at the various experiments. In this thesis we present measurements on Z bosons and J/ψ, reconstructed in the muon spectrometer of the ALICE detector.
Observations from PbPb collisions are subject to effects unrelated to the QGP, and it is important to disentangle these from QGP effects. In particular, parton distributions are different in heavy nuclei than in unbound protons and neutrons. In order to describe the production of probes with large transverse momentum, special objects called nuclear parton distribution functions (nPDFs) are necessary. They are a crucial ingredient of calculations of cross sections in heavy ion collisions, but cannot be obtained from first principles calculations in QCD. Instead, they are instead obtained from fits to data which include, among others, measurements of electroweak bosons. The latter can therefore be used to constrain or verify the accuracy of the nPDFs. In this thesis, the production of Z bosons in PbPb collisions at a center-of-mass energy per nucleon pair of 5.02 TeV with the ALICE detector is reported. The results strongly show a preference for models that take nuclear modifications to PDFs into account. This indicates that parton distributions in nuclei are not a simple superposition of protons and neutrons.
In the near future, proton-oxygen and oxygen-oxygen collisions will take place at the LHC. We detail projections of Z boson production in these collisions, obtained by extrapolating existing cross sections from the ALICE and LHCb experiments. With the expected integrated luminosities for the two collision systems, measurements are found to be unfeasible.
In proton-proton collisions, heavy particles such as the J/ψ are produced from a single partonic scattering (SPS). It is possible to create a pair of J/ψ from such a process, as opposed to a single J/ψ. However, J/ψ pairs can also be created through another mechanism. Because the densities of partons increase rapidly at high energies, it becomes possible for two parton scatterings to occur during a single pp collision. This is referred to as double parton scattering (DPS). J/ψ pairs can therefore be used as a tool to study relative contributions of SPS and DPS. In this thesis, a measurement of the production cross section of J/ψ pairs in proton-proton collisions at sqrt(s) = 13 TeV is presented. The measurement serves as a first of its kind in ALICE. It shows good agreement the cross section obtained by LHCb collaboration, although experimental uncertainties are large. Future LHC data taking periods will provide a larger data sample, which will allow for a measurement with better experimental precision. This could enable a measurement in which SPS and DPS contributions can be separated.